DEPARTMENT OF PHYSICS
UNIVERSITY OF JYVÄSKYLÄ
RESEARCH REPORT No. 3/2014

EXPERIMENTAL CHARACTERIZATION OF ELECTRONIC, STRUCTURAL AND OPTICAL PROPERTIES OF INDIVIDUAL CARBON NANOTUBES

BY
OLLI HERRANEN

Academic Dissertation
for the Degree of
Doctor of Philosophy

To be presented, by permission of the
Faculty of Mathematics and Natural Sciences
of the University of Jyväskylä,
for public examination in Auditorium FYS-1 of the
University of Jyväskylä on May 16, 2014
at 12 o'clock noon

Jyväskylä, Finland
May 2014

Preface

The work reviewed in this thesis has been carried out during the years 2009-2014 at the Nanoscience Center, Department of Physics at the University of Jyväskylä, Finland.

First I would like to thank my supervisor Professor Markus Ahlskog for his guidance and support during my Ph.D. project. I first started as a summer student in the group during the summer of 2005. The past nine years have taught a lot. I have had opportunities to meet wonderful people that have always been patient and helpful. Special thanks to Dr. Andreas Johansson who has been guiding me a lot especially in the first years of my Ph.D. studies and it has been always easy to ask help and share scientific problems in the lab with him. I also want to thank all the present and the past members of the Moltech group especially Mr. Mikael Pajunen for teaching me the secrets of e-beam lithography and Dr. Deep Talukdar for guiding me to the world of noise. I'm also grateful to other former and present staff in NSC especially Dr. Jenni Karvonen, Dr. Kimmo Kinnunen, Mr. Antti Nuottajärvi and Mr. Tarmo Suppula for helping and guiding me in various different problems and practical issues in the lab. Collaboration with Prof. Mika Pettersson's group has been very fruitful and it has always been easy to ask questions from Mika related to optical spectroscopy. Also collaboration groups of Prof. Esko Kauppinen and Prof. Martti Kauranen are greatly acknowledged.

Special thanks go also to the nice working environment and atmosphere in the NSC and in the Department of Physics and especially to the following persons for their friendship, support, and many fascinating discussions during the years from freshman to Ph.D. student: Mr. Janne-Petteri Niemelä, Mr. Jaakko Leppäniemi, Dr. Mikko Leskinen, Mr. Mikko Palosaari, Dr. Veikko Linko and Dr. Ville Kotimäki.

Finally, I wish to thank my family. My brother Matti has been always patient enough for my questions and problems related to physics. Thanks to my parents Ritva and Pertti who have always been supporting and caring me during the life. Last, I want to thank my beloved wife, Sanna for her love and support and my children Elli, Aake and Ilta for brighten my days throught the project and given me something totally else to think.

This thesis has been supported by Jenny and Antti Wihuri foundation and Finnish Cultural Foundation which are greatfully acknowledged.

Abstract

Herranen, Olli
Experimental characterization of electronic, structural and optical properties of individual carbon nanotubes
Jyväskylä: University of Jyväskylä, 2014, 114 p.
(Research report/Department of Physics, University of Jyväskylä,
ISBN 978-951-39-5650-9 (paper copy)
ISBN 978-951-39-5651-6 (pdf)
ISSN 0075-465X
diss.

In this thesis properties of individual carbon nanotubes (CNTs) are studied performing measurements in electronic transport, including noise, optical spectroscopy and electron diffraction. Furthermore, novel sample geometry of suspended CNT devices is developed and a CNT synthesis setup relying on chemical vapor deposition (CVD) has been established.

Combined Raman and transport measurements on individual singlewalled nanotubes (SWNTs) are performed. These methods serve as powerful tools to determine the properties of a single device. In addition, it is possible to evaluate the reliability of these two mutually independent methods.

Suspended nanotube structures with a fully transparent path are very useful in various measurements including optical spectroscopy with reduced background noise and various transport effect neglecting the substrate effects to the CNT channel. The main benefit of the fully transparent path is that it is possible to determine the exact chiral indices of the studied tube by using the electron diffraction technique with transmission electron microscope (TEM). Such structures require new microfabrication techniques and a reliable method to prepare suspended CNTs samples is developed. In this work though, fully working electrical contacts could not be included in the measured samples due to various fabrication problems. The past and the state-of-the-art of the relevant fabrication issues are discussed in this thesis.

The suspended CNTs were studied by in-house and other collaborators using nonlinear optical techniques. The first four-wave-mixing (FWM) signal from individual semiconducting SWNT was shown. Furthermore, FWM imaging is presented which serves as a fast and sensitive imaging technique. The first observation of second harmonic generation (SHG) from an individual CNT is

also presented which could be exploited for fast determination of handedness of a CNT in the future.

The last study presents the results of noise measurement on intermediate sized multiwalled carbon nanotubes (MWNTs). Such tubes can possess ballistic conduction but don't form noticeable Schottky barriers at the CNT-metal contact, as opposite compared to SWNTs. We have shown that the noise properties of such a system is described better using ballistic noise models compared to more conventional models developed for diffusive transport. Furthermore, the noise magnitude was found to be one to two orders of magnitude smaller than in similar SWNT devices.

Keywords Carbon nanotube, electrical transport, $1/f$ noise, chemical vapor deposition, electron diffraction, optical spectroscopy

Author Olli Herranen
Nanoscience Center
Department of Physics
University of Jyväskylä
Jyväskylä
Finland

Supervisor Professor Markus Ahlskog
Nanoscience Center
Department of Physics
University of Jyväskylä
Jyväskylä
Finland

Reviewers Dr. Tech. Juha Riikonen
Department of Micro and Nanosciences
Aalto University School of Electrical Engineering
Espoo
Finland

Dr. Krisztián Kordás
Department of Electrical Engineering
University of Oulu
Oulu
Finland

Opponent Docent Krister Svensson
Department of Physics
Karlstad University
Karlstad
Sweden

List of publications

This thesis is based on the work contained in the following publications:

A.I. J. Rintala, O. Herranen, A.Johansson, M. Ahlskog and M. Pettersson, *Raman Spectroscopy and Low-Temperature Transport Measurements of Individual Single-Walled Carbon Nanotubes with Varying Thickness*, Journal of Physical Chemistry C **113**, 15398 (2009).

A.II. O.Herranen, J. Rintala, A. Johansson, P. Queipo, A. G. Nasibulin, E. I. Kauppinen, M. Pettersson and M. Ahlskog, *Electronic transport measurements and Raman spectroscopy on carbon nanotube devices*, Physica Status Solidi B **246**, 2853 (2009).

A.III. P. Myllyperkiö, O. Herranen, J. Rintala, H. Jiang, P. R. Mudimela, Z. Zhu, A. G. Nasibulin, A. Johansson, E. I. Kauppinen, M. Ahlskog and M. Pettersson, *Femtosecond Four-Wave-Mixing Spectroscopy of Suspended Individual Semiconducting Single-Walled Carbon Nanotubes*, ACS Nano **4**, 6780 (2010).

A.IV. M. J. Huttunen, O. Herranen, A. Johansson, H. Jiang, P. R. Mudimela, P. Myllyperkiö, G. Bautista, A. G. Nasibulin, E. I. Kauppinen, M. Ahlskog, M. Kauranen and M. Pettersson, *Measurement of optical second-harmonic generation from an individual single-walled carbon nanotube*, New Journal of Physics **15**, 083043 (2013).

A.V. J. Aumanen, A. Johansson, O. Herranen, P. Myllyperkiö and M. Pettersson, *Local Photo-Oxidation of Individual Single Walled Carbon Nanotubes Probed by Femtosecond Four Wave Mixing Imaging*, manuscript submitted.

A.VI. O. Herranen, D. Talukdar and M. Ahlskog, *Ultra-Low Noise Multi-walled Carbon Nanotube Transistors*, Carbon, in press (2014) http://dx.doi.org/10.1016/j.carbon.2014.04.050

Author's contribution

In **A.I** and **A.II** the author has fabricated the samples, carried out all the transport measurements and participated in Raman measurements and data

analysis. In **A.I** the author participated in the writing and in **A.II** was the main writer of the publication.
In **A.III**–**A.V** the author has developed the sample geometry, fabricated the slit structures, participated in the electron diffraction measurements and writing of the publications. In **A.V** the author did the CNT synthesis.
In **A.VI** the author has fabricated the samples, carried out the measurements and is the main writer of the manuscript.

Other work to which author has contributed:

M. Ahlskog, O. Herranen, A. Johansson, J. Leppäniemi and D. Mtusko, *Electronic transport in intermediate sized carbon nanotubes*, Physical Review B **79**, 155408 (2009)

D. Talukdar, P. Yotprayoonsak, O. Herranen, M. Ahlskog, *Linear current fluctuations in the power-law region of metallic carbon nanotubes*, Physical Review B **88**, 125407 (2013)

List of Abbreviations

2DEG	Two dimensional electron gas
A	Anisole
AC	Alternating current
AFM	Atomic force microscopy
ALD	Atomic layer deposition
CARS	Coherent anti-Stokes Raman scattering
CNT	Carbon nanotube
CVD	Chemical vapor deposition
DAQ	Data aquisition
DC	Direct current
DEP	Dieletrophoresis
DM	Dichroic mirror
ED	Electron diffraction
EL	Ethyl lactate
EPC	Electron-phonon coupling
FET	Field-effect transistor
FIB	Focused ion beam
FWM	Four-wave-mixing
GBIP	General purpose interface bus
IPA	Isopropanol
KA	Kohn anomaly
LB	Langmuir-Blodgett
LO	Longnitudal optical mode
LPCVD	Low-pressure chemical vapor deposition
MIBK	Methyl isobutyl ketone
MOSFET	Metal-oxide-semiconductor field-effect transistor
MW	Molecular weight
MWNT	Multiwalled carbon nanotube
NOPA	Non-collinear optical amplifier
PMMA	Polymethylmethacrylate
PMMA-MAA	Polymethylmethacrylate-co-methacrylic acid
PMT	Photomultiplier tube
PRR	Pulse repetition rate

QPC	Quantum point contact
RBM	Radial breathing mode
RIE	Reactive-ion etching
RR	Resonance Raman
RTN	Random telegraph noise
SEM	Scanning electron microscopy
SB	Schotkky barrier
SHG	Second harmonic generation
SOI	Silicon-on-insulator
STM	Scanning tunneling microscopy
SWNT	Singlewalled carbon nanotube
TEM	Transmission electron microscopy
TFT	Thin film transistor
TO	Transverse optical mode
UHV	Ultra-high vacuum
WLS	White-light source

Contents

Chapter 1

Introduction

Carbon nanomaterials are most interesting in materials science. Their unique mechanical and electrical properties make them suitable for a variety of different applications. Especially graphitic materials such as fullerenes, nanotubes and graphene have been the topic of an increasing number of studies in the past decades. They are promising candidates in the future to replace many existing material and are already in use in many different fields. The present and potential applications include composite materials, thin film applications such as displays, electronics components such as transistors, energy storage such as batteries and supercapacitors, energy harvesting such as solar cells, biosensors and other biotechnology applications etc. [1]

Carbon nanotubes got international publicity in 1991 when Iijima published the famous paper called *Helical microtubules of graphitic carbon* [2]. However, the first images of such material were probably taken by Radushkevich et al. in 1952 [3] but their report was written in Russian and didn't get publicity in the international community. In 1976 Oberlin et al. reported images of hollow graphitic cylinders [4]. The production of first the nanotubes goes even further in history and already ancient Syrian blacksmiths have been producing them in the Middle Ages, when forging Damascus steel. Of course, the syrians were not aware of that but it was verified later when examining ancient sword blades [5].

A new era of carbon-related research began in 1985 when a new allotrope of carbon, fullerenes, was found by Kroto et al. [6]. They vaporized graphite by laser irradiation which led to the formation of the C_{60} molecule resembling a football. It was named as buckminsterfullerene or buckyballs. The main authors of the original paper won the Nobel Price of chemistry in 1996 for their work on buckyballs. The building block of graphitic materials of all other dimensionalities got publicity in 2004 when graphene was introduced [7]. It can be wrapped up into 0D fullerenes, rolled into 1D nanotubes or stacked into 3D graphite.

Description of this work

Still, lots of basic research needs to be done to understand the properties of such materials even better and to bring forward them into the market on a larger scale. In this thesis individual carbon nanotube devices are studied with different measurement techniques including electrical measurements, optical spectroscopy and electron microscopy. Chapter 2 describes combined transport and Raman studies on individual single-walled carbon nanotube devices. Also the development in sample fabrication is reviewed briefly. Chapter 3 concentrates on the fabrication of suspended nanotube structures which would allow combining optical spectroscopy and electrical transport measurements from index identified nanotubes assigned using electron diffraction. In the beginning of the chapter, a short literature review is given on the topic of suspended nanotube samples. Chapter 4 then describes the electron microscopy and nonlinear optical spectroscopy that was performed to the suspended devices. Understanding the noise is crucial for many applications. Noise properties of CNTs are discussed in chapter 5 and results from noise measurements of multiwalled nanotubes are presented. Finally, the summary is presented in chapter 6.

1.1 The structure of carbon nanotubes

The structure of carbon nanotubes is closely related to graphene. Graphene exhibits planar sp^2 hybridization. Carbon has four valence orbitals: $2s$, $2p_x$, $2p_y$ and $2p_z$ orbitals. Among these orbitals the (s, p_x, p_y) orbitals combine and form bonding σ and antibonding σ^* orbitals. The σ bonds are strong covalent bonds with a large energy gap between the states. Therefore they don't play any role in the electronic properties of graphene and are often neglected. They, however, determine the mechanical properties of graphene sheets. The remaining p_z orbital, pointing out from the graphene sheet cannot couple with the σ states. Instead it can form delocalized orbitals which have bonding π and antibonding π^* orbitals close to the Fermi energy E_F. These π orbitals cross at K-points showing linear dispersion. Therefore graphene is called a semimetal. [8]

Graphene is a sheet of carbon atoms that are densely packed in a honeycomb crystal lattice [9]. It is not a Bravais lattice (array of points that are generated by a set of translations) but it can be formed from hexagonal Bravais lattice with two atom basis. The unit cell and the Brillouin zone of the graphene honeycomb lattice can be seen on fig. 1.1 (a) and (b). The Brillouin zone consists of three high symmetry points, Γ, K and M as the center, the corner, and the center of the edge, respectively. The energy dispersion relations are calculated between these symmetry points. Furthermore, there are two inequivalent K-points in the graphene Brillouin zone labeled as $K : \left(0, \frac{4\pi}{3a}\right)$ and $K' : \left(0, -\frac{4\pi}{3a}\right)$.

The carbon nanotubes are just graphene rolled into a cylindrical form seamlessly. The nanotube chiral vector i.e. circumferential vector $\vec{C_h}$ can be formed by using graphene unit vectors. The chiral vector is always an integer multiple

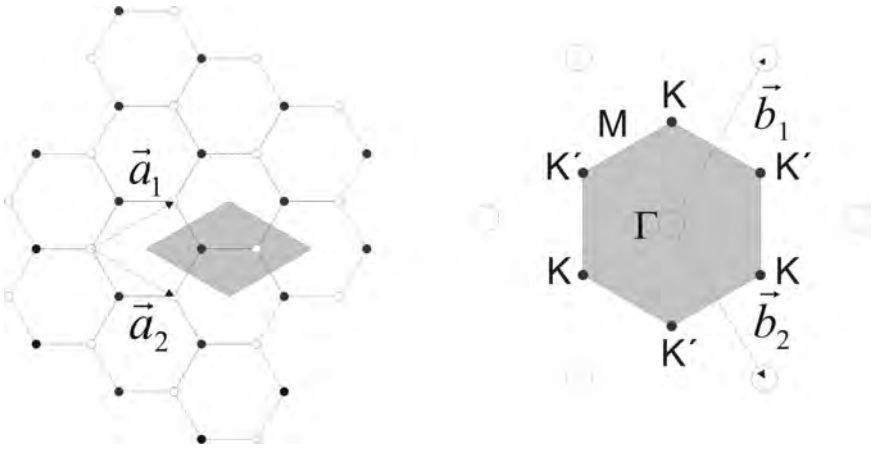

Figure 1.1: **a)** Graphene honeycomb lattice with two-atom basis (white and black dots represent the two inequivalent carbon atoms), lattice vectors $\vec{a_1}$, $\vec{a_2}$ and the unit cell (gray area). **b)** Reciprocal space, reciprocal lattice vectors $\vec{b_1}$, $\vec{b_2}$ and first Brillouin zone (gray area) of the graphene. Adapted with permission from reference [9].

of the lattice vectors i.e. $\vec{C_h} = n\vec{a_1} + m\vec{a_2}$ and it thus describes the structure of nanotube (see fig. 1.2). This means that the whole geometry of the SWNT is determined by a pair of integers (n, m) [8]. The unit cell of a CNT is a rectangle generated by the chiral vector $\vec{C_h}$ and the translational vector $\vec{T}$ containing $2N$ carbon atoms, where N is the number of hexagons in the unit cell. The Brillouin zone of a nanotube is one dimensional and the zone edges are usually labeled as X, $\vec{X} = \pm(\pi/T)\vec{\kappa}_{||}$, where $\vec{\kappa}_{||}$ is the basis vector along $\vec{T}$-direction i.e. axial direction of the tube. Therefore, the nanotube band structure is represented along the $\Gamma - X$ -direction. Nanotubes of the type $(n, 0)$ $(\theta = 0\ ^\circ)$ are called zigzag tubes, tubes of type (n, n) $(\theta = 30\ ^\circ)$ are called armchair tubes and tubes of type $((n, m \neq n \neq 0))$ are called chiral tubes. All the essential structural parameters of the SWNT are described in table 1.1.

The energy dispersion relation of the SWNT is obtained from graphene using the zone folding approximation. The periodic boundary conditions due to rolling up of the sheet leads to quantization of allowed wave vectors in the circumferential direction since the circumferential length becomes comparable to the Fermi wavelength λ_f. The periodic boundary conditions are described as

$$\vec{k} \cdot \vec{C_h} = 2\pi q, \tag{1.1}$$

where q is integer. The wave vector $\vec{k}$ is continuous along the tube axis $(k_{||})$ but restricted in the circumferential $k_\perp$ direction and thus a set of parallel lines to the axial direction of the tube is generated as seen in figure 1.3 (a). Therefore the energy bands are set of 1D dispersions formed from cross sections of the

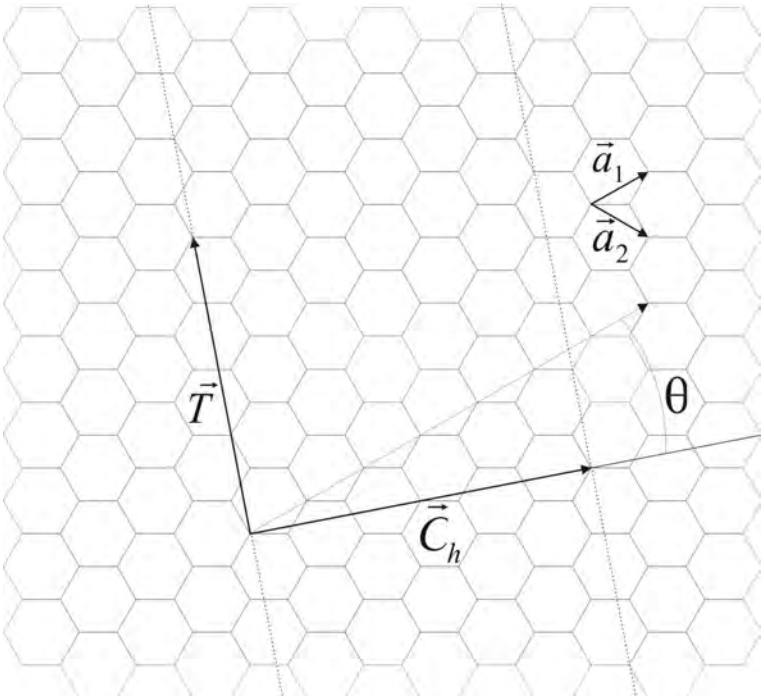

Figure 1.2: Graphene honeycomb lattice with lattice vectors $\vec{a_1}$ and $\vec{a_2}$. The chiral vector $\vec{C_h}$ represents a possible wrapping of the graphene sheet into a tubular form. The direction perpendicular to $\vec{C_h}$ is the tube axis and spans the translational vector $\vec{T}$. Translational vector is the unit vector of CNT. Adapted with permission from reference [8].

Table 1.1: Structural parameters for a (n,m) nanotube. Adapted with permission from reference [8].

Symbol	**Name**	**Formula**	**Values**
a	lattice constant	$a = \sqrt{3}a_{cc} \approx 2.46$ Å	$a_{cc} \approx 1.42$ Å
$\vec{a_1}$, $\vec{a_2}$	basis vectors	$\left(\frac{\sqrt{3}}{2}; \frac{1}{2}\right) a$, $\left(\frac{\sqrt{3}}{2}; -\frac{1}{2}\right) a$	
$\vec{b_1}$, $\vec{b_2}$	reciprocal-lattice vectors	$\left(\frac{1}{\sqrt{3}}; 1\right) \frac{2\pi}{a}$, $\left(\frac{1}{\sqrt{3}}; -1\right) \frac{2\pi}{a}$	
$\vec{C_h}$	chiral vector	$\vec{C_h} = n\vec{a_1} + m\vec{a_2} \equiv (n, m)$	$(0 \leq \lvert m \rvert \leq n)$
d_t	tube diameter	$d_t = \frac{\lvert\vec{C_h}\rvert}{\pi} = \frac{a}{\pi}\sqrt{n^2 + nm + m^2}$	
θ	chiral angle	$\sin\theta = \frac{\sqrt{3}m}{2\sqrt{n^2+nm+m^2}}$	$0 \leq \lvert\theta\rvert \leq \frac{\pi}{6}$
		$\cos\theta = \frac{2n+m}{2\sqrt{n^2+nm+m^2}}$	$\tan\theta = \frac{\sqrt{3}m}{2n+m}$
$\vec{T}$	translational vector	$\vec{T} = t_1\vec{a_1} + t_2\vec{a_2} \equiv (t_1, t_2)$	$\gcd(t_1, t_2)$
		$t_1 = \frac{2m+n}{N_R}$, $t_2 = -\frac{2n+m}{N_R}$	$N_R = \gcd(2m + n, 2n + m)$
N_C	number of C atoms per unit cell	$N_C = \frac{4(n^2+nm+m^2)}{N_R}$	

graphene dispersion relations [9]. If at least one k-line crosses the K point of the graphene Brillouin zone, the tube is metallic. If none of the lines cross the point, an energy gap between the valence and conduction bands is created and the tube is thus semiconducting. In general, the (n, m) nanotube is metallic if $n - m = 3l$ (l is integer) and otherwise semiconducting. Thus armchair (n, n) tubes are always metallic. However, $(n, 0)$ zigzag tubes satisfying the metallic condition are actually small band gap semiconducting tubes (gap comparable to thermal energy in room temperature) due to the curvature effects. The band gap of the semiconducting nanotube is roughly inversely proportional to tube's diameter as

$$E_g = \frac{2a_{cc}\lambda_0}{d_t}, \tag{1.2}$$

where a_{cc} is the $C-C$ bond length and $\lambda_0 = 2.9$ eV the transfer integral between first-neighbor π orbitals. [8]

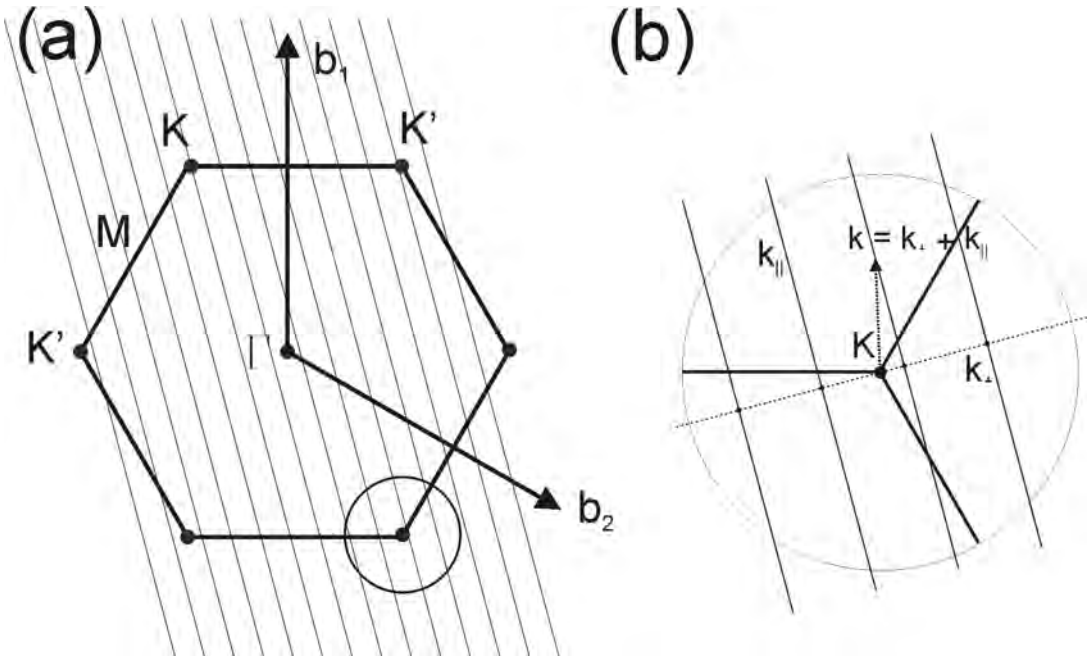

Figure 1.3: (a) Graphene Brillouin zone and allowed k-states in SWCNT (parallel lines). (b) Expanded depiction of allowed states near K point. Dashed line is the direction of the chiral vector $\vec{C_h}$. Adapted with permission from reference [10].

As described earlier, the unit cell of CNT contains $2N$ atoms and thus the band structure consists of N bonding π orbitals and N antibonding π^* orbitals. Furthermore, the density of states (DOS) $D(E) = \Delta N/\Delta E$ represents the number of available states for a given energy interval. The shape of the DOS depends dramatically on dimensionality. In one dimensional system the DOS is inversely

proportional to the square root of the energy [11]. The DOS diverges close to band extreme and these peaks are called Van Hove singularities (VHSs). The dispersion relation and the DOS is shown for metallic and semiconducting tubes in figure 1.4.

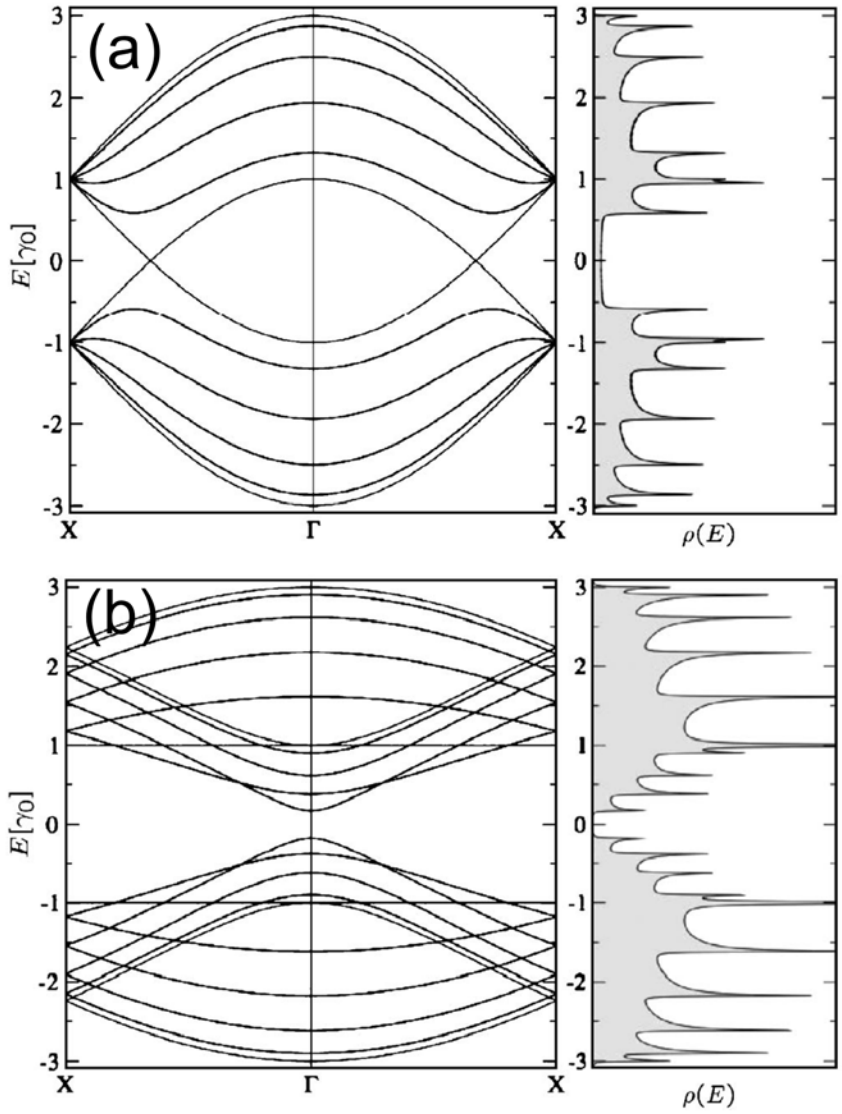

Figure 1.4: Band structure and density of states (a) for a $(5, 5)$ armchair metallic nanotube and (b) for $(10, 0)$ zigzag semiconducting nanotube. The Fermi energy is located at zero energy. Adapted with permission from reference [8].

Chapter 2

Combined transport and Raman measurements

Singlewalled carbon nanotubes were studied with Raman spectroscopy and low temperature transport measurements. The idea was to obtain information of the basic properties from an individual carbon nanotube with these mutually independent methods. First, basic theory of electrical transport and Raman spectroscopy is discussed. Then, the actual measurement results are presented and discussed in the following sections.

2.1 Transport properties of carbon nanotubes

The conductance of quasi-1D system is given by the Landauer formula [12]:

$$G(E) = \frac{2e^2}{h} M(E) T, \tag{2.1}$$

where $M(E)$ is the number of subbands contributing to the charge transfer and T is the average transmission probability of each subband. Three kinds of characteristic lengths are present in the mesoscopic systems: the mean free path l_m, the Fermi wavelength λ_F and the phase relaxation length l_ϕ [13]. The mean free path describes the average length that electrons travel before scattering. The Fermi wavelength is the de Broglie wavelength of electrons at Fermi energy and the phase-relaxation length is the average length where the electron retains it coherence as a wave. Elastic scattering of electrons doesn't contribute for l_ϕ, but only for l_m as inelastic scattering contributes to both of them. Only electrons that are near the Fermi energy contribute in transport so the lengths l_m and l_ϕ are scaled by the Fermi velocity as follows [13]

$$l_m = v_F \tau_m \qquad \& \qquad l_\phi = v_F \tau_\phi, \tag{2.2}$$

where τ_m is the momentum relaxation time and τ_ϕ the phase relaxation time. The times correspond to the overall changes of phase and momentum in the

system, not a single scattering event. It means that for example the changes in momentum reach $\hbar k_F$ and phase π, respectively.

Transport through the system can be classified into three different regimes: ballistic, diffusive and classical. The relationship between the characteristic lengths determines then the transport regime. The conductance is ballistic when the 1D channel length between contacts is smaller than the mean free path and the phase relaxation length of the channel [13]. It means that there are no scattering centers in the channel and thus transmission probability T reaches one if assuming ideal contacts. So the only resistance in the ballistic case comes from the contacts and if the contacts are ideal (Ohmic) i.e. reflectionless, the resistance reaches the quantized value. However, in general some scattering in the channel is always present. Therefore the resistance of the device is $R_c + R_t$, where R_c is the contact resistance and R_t is the resistance of the channel.

Carbon nanotubes are reported to be 1D ballistic conductors [14], [15], [16]. Metallic nanotubes have two conduction channels because two subbands cross at the Fermi energy [17]. The theoretical maximum conductance for such device can be obtained from the equation (2.1) by setting $T = 1$ and $M = 2$:

$$G_q = \frac{4e^2}{h} = 2G_0 \approx 1.549 \cdot 10^{-4}\ S \ \textit{i.e.}\ R_q = (2G_0)^{-1} = 6.45\ \text{k}\Omega,$$

where G_0 is the quantum conductance. Semiconducting nanotubes exhibit also ballistic conduction and then both the valence and the conduction band act as conduction channels. In reality there will always be backscattering from the contact interface which leads to $T < 1$ and thus the metal electrode-nanotube contact has a big influence on the transport properties of the tube [8]. Metallic nanotubes can get really close to the conductance maximum with ideal Ohmic contacts [14], [15]. In the case of metal-semiconducting nanotube contact a Schottky barrier is formed in the interface [16], [18] and the characteristics of the SWNT-FET is described by modulating the Schotkky barrier thickness at the contacts. The critical issues in barrier formation are the work function of the metal and size of the band gap (which furthermore is inversely proportional to the diameter). Thus CNTs larger than ~ 2 nm don't form Schottky barriers with Palladium (Pd) as the contact metal [16].

The role of the contact has indeed a great influence to the behavior of the CNT device but besides the geometry of the contact and the work function of the metal also the wetting properties of the metal have big influence [16], [17]. The ideal case would be to have metal whose wetting properties are good and work function is at the same level as the valence or conduction band of the tube. Then the barrier would not affect the charge injection so much and the ON-state current would not be affected by the barrier.

Additional resistance from the nanotube channel itself occurs due to different scattering processes. One major scattering mechanism is electron-phonon scattering. Acoustic phonon scattering dominates at small bias voltages, whereas at large bias voltages it is scattering by optical and zone-boundary phonons [19].

Scattering from optical phonons is especially large in metallic tubes working at room temperature. Therefore, the effects of the environment have been demonstrated to affect to the transport of the tube significantly and the transport and phonon scattering is completely different in suspended tubes compared to the tubes on the substrate[20]. The current saturates once the electron emits a phonon which happens as soon as the energy of the electron has reached the optical phonon energy. The excess energy created by the phonon can be remarkable which furthermore heats the tube. Even negative differential conductance can be seen in the suspended tubes. Tubes that are on the substrate have more interaction with the substrate which leads to greater heat dissipation and relaxation of the optical phonons emitted through electron scattering. The phonon scattering in the semiconducting tubes is due to acoustic phonons since the tube ON-state resistance has been reported to grow linearly with temperature [21]. Many other sources of disorder such as localized lattice defects [22], electrostatic potential fluctuations and mechanical deformations [23], [24] affect also the scattering processes. The effects of disorder for clean nanotubes become dominant at low temperatures and these effects can be determined by extracting the mean free path of nanotube. The mean free paths of both metallic and semiconducting nanotubes have been reported to be several microns at low temperature [25].

2.1.1 Coulomb blockade

Quantum effects become relevant at low temperature when thermal energy is reduced enough. Especially in reduced dimensionality these effects are more visible because of the larger energy scales. [19].

Coulomb blockade effects can arise when two conditions are fulfilled. Firstly, the tunneling (or contact) resistance between the tube and the electrode must be larger than the so called quantum of resistance $R_q = h/2e^2$. Secondly, the total capacitance of a metallic island must be small enough so that the energy required to add an electron to the island becomes larger than the thermal energy [8]. The conditions are therefore

$$E_c = \frac{e^2}{2C} > k_B T = E_T, \quad R_c >> R_q = 12.9 \text{ k}\Omega. \tag{2.3}$$

When the contact resistance is very small so that the contacts are nearly perfect and the channel itself is ballistic, Fabry-Pérot interference of electron waves multiply reflected between two CNT-metal interfaces can occur. It means that the tube act as a coherent electron waveguide and a resonant cavity is formed between the electrode-nanotube interfaces [26].

2.2 Introduction to Raman scattering

Electromagnetic radiation incident upon matter will interact with it. Most of the photons will go unscattered through the atom but a small part will scatter from

it. Elastic scattering is called Rayleigh scattering and inelastic scattering either Raman or Brillouin scattering. Raman scattering is a process where photons scatter from optical phonons as in Brilloun scattering from acoustic phonons. [27]

In this section we are concentrating on scattering processes from nano-objects e.g. molecules and nanotubes. Scattering processes can be treated with a semi-classical approach. The photons are treated as classical electromagnetic waves while the scatterer as a quantum mechanical system. First-order Raman scattering is a three step process. The absorption of an incoming photon creates an electron-hole pair, which then scatters inelastically under the emission of a phonon, and finally recombines and emits the scattered photon. If a molecule absorbs energy, the scattering is called Stokes scattering and if it loses energy, anti-Stokes scattering. Compared to Rayleigh scattering (where the molecule returns to its incident state), Raman scattering is very weak. The scattered photon can have frequencies

$$\nu_1 = \nu_0 \pm \nu_{ph}, \tag{2.4}$$

where ν_0 is the frequency of the incident photon and ν_{ph} is the frequency of the phonon. In Raman spectroscopy, one measures the vibrational frequencies as a shift from the incident beam frequency. [28]

The scattering processes can be explained by the use of simple classical physics [28]. Let's consider an electromagnetic wave $E(t) = E_0 \cos 2\pi\nu_0 t$, where E_0 is the amplitude of the wave and ν_0 the frequency of the wave. In general, the interaction between an electromagnetic field and a molecule can be described with polarization density, or simply polarization, created by radiation hitting the molecule. The field induces a force to the electrons of the molecule which will then displace them related to the nucleus of the atom. Thus, an electric dipole is generated and described by a dipole moment vector. In macroscopic scale the polarization is defined as a sum of the individual dipole moment vectors. The induced electric dipole moment μ has the form of

$$\mu = \alpha E = \alpha E_0 \cos 2\pi\nu_0 t, \tag{2.5}$$

where α is called the polarizability. If the molecule is vibrating with a frequency ν_m, the nuclear displacement q is

$$q(t) = q_0 \cos 2\pi\nu_m t, \tag{2.6}$$

where q_0 is the vibrational amplitude. In small amplitudes polarizability α depends linearly on q and thus it can be written as a Taylor series:

$$\alpha = \alpha_0 + \left(\frac{\partial\alpha}{\partial q}\right)_{q=0} q + ... \tag{2.7}$$

Combining equations (2.5), (2.6), (2.7) one gets

$$\begin{aligned}\mu &= \alpha E_0 \cos 2\pi\nu_0 t \\ &= \alpha_0 E_0 \cos 2\pi\nu_0 t + \left(\frac{\partial\alpha}{\partial q}\right)_{q=0} q E_0 \cos 2\pi\nu_0 t \\ &= \alpha_0 E_0 \cos 2\pi\nu_0 t + \left(\frac{\partial\alpha}{\partial q}\right)_{q=0} q_0 E_0 \cos 2\pi\nu_m t \cos 2\pi\nu_0 t.\end{aligned} \tag{2.8}$$

Furthermore, using a trigonometric formula $2\cos x \cos y = \cos(x+y) + \cos(x-y)$ we get the equation (2.8) in the form

$$\mu = \alpha_0 E_0 \cos 2\pi\nu_0 t + \frac{1}{2}\left(\frac{\partial\alpha}{\partial q}\right)_{q=0} q_0 E_0 [\cos 2\pi(\nu_0+\nu_m) + \cos 2\pi(\nu_0-\nu_m)]. \tag{2.9}$$

The first term describes Rayleigh scattering, the second term anti-Stokes scattering and the third Stokes scattering. Thus, if the derivative $\partial\alpha/\partial q$ is zero, the vibration is not Raman active.

In general, molecules can be classified into different point groups i.e. same symmetry groups. The basic symmetry operations are identity E, rotation C_n, reflection σ_l, improper rotation S_n and inversion i. A molecule consisting of N atoms has $3N$ degrees of freedom i.e. the number of coordinates needed to specify the positions of all N atoms. The translational motion of the molecule in space can be described with three coordinates and additional three coordinates, such as Euler's angles, are needed to describe the orientation. Hence, in total $3N-6$ vibrational modes are available for each molecule. If the molecule is linear (only two orientation coordinates needed) available modes are $3N-5$. . The vibrational modes can be classified in different symmetry groups, some vibrations being only infrared (IR) active or Raman active. Thus general selection rules of certain vibrations being either IR or Raman active can be derived [28].

2.3 Raman spectrum of CNTs

The carbon nanotube has 6N phonon modes (since the unit cell of CNT consists $2N$ carbon atoms) but only few of them are either Raman or IR active depending on the symmetry properties of the particular tube since different tube chiralities belong to different symmetry groups. Only symmetry at the Γ-point ($\vec{k}=0$) vibrations are Raman active since only phonons associated to $\vec{k}$ close to zero are coupled to incident light. Even though the number of phonon modes can vary significantly depending on the chiral indices and thus tube diameter, the Raman and IR active modes are almost constant. In fact, there are either 15 or 16 Raman active modes in which only 6 or 7 are intense depending on the tube chirality. [9]

Raman spectra of individual CNTs are based on resonance Raman condition. Resonance Raman (RR) happens when the excitation energy of the laser is in

the resonance of one of the electronic excitations. In that case one could obtain huge enhancement in Raman cross-section (probability to Raman scattering) (in order to $\sim 10^6$). RR is hence very useful to study small objects such as carbon nanotubes. A Raman spectrum of SWNT is shown in figure 2.1. Three major peaks can usually be seen from the spectra: radial breathing mode (RBM), D-band and G-band. The fourth peak which has getting more attention in recent years is called the G'-band.

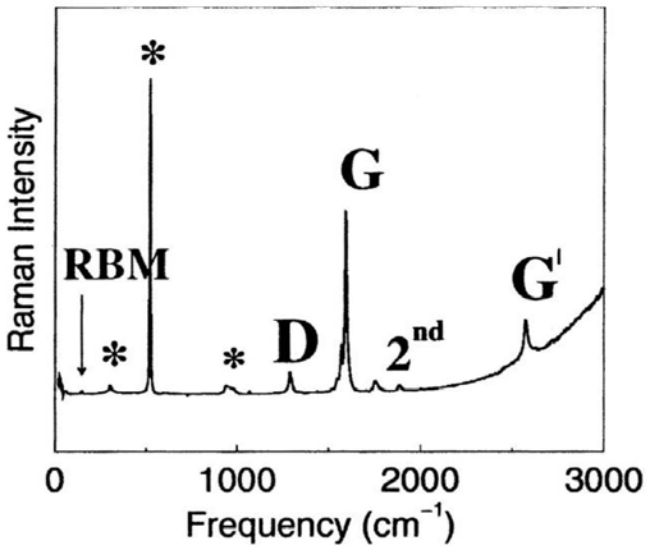

Figure 2.1: Raman spectrum of nanotube showing RBM, D-band, G-band and G'-band. Asterisks are from the Si/SiO_2 substrate. Adapted with permission from reference [29].

2.3.1 Radial breathing mode

The radial breathing mode (RBM) originates from the A_{1g} phonon mode where the carbon atoms move radially and the diameter of tube varies as seen in figure 2.2. It occurs usually in the frequency region of $100-400$ cm^{-1} and the frequency of the mode is inversely proportional to the tube's diameter:

$$\omega_{RBM} = \frac{\alpha}{d_t} + B, \tag{2.10}$$

where the values of constants α and B vary significantly in different studies and the measurements have given values such as $\alpha = 248$ cm^{-1}nm and $B = 0$ [30] and $\alpha = 217.8$ cm^{-1}, $B = 115.7$ cm^{-1} [31] for substrate supported tubes. Suspended tubes have been studied to minimize the effects with the substrate and electron diffraction has been used to directly determine the chiral indices of the tubes. Such studies have proposed values like $\alpha = 204$cm^{-1}, $B = 27$cm^{-1}

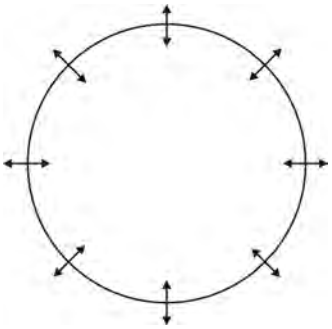

Figure 2.2: Radial breathing mode of carbon nanotube.

[32], $\alpha = 228\text{cm}^{-1}$, $B = 0$ [33]. The difference has been explained by the quality of the tubes. For example amorphous carbon at the tube surface might affect the relation [34]. Studies of other groups [34, 35] seem to confirm also that the constant $\alpha = 228\text{cm}^{-1}$ ($B = 0$) is correct to pristine tubes without environmental effects.

Chiral-index assignment

Since each tube has defined chiral indices and hence electronic properties related to the tube's diameter, they can be plotted in a so called Kataura plot (see figure 2.3), which plots the excitation energies of the tube as a function of tube's diameter. The plot is obtained e.g. by calculating the band structure of the tubes [36]. If determining the transition energies from resonance peak profiles [37] the transition energies of the tubes can be plotted as a function of measured RBM frequency which is called the experimental Kataura plot. (see figure 2.3). When the (E_{ii}, ω_{RBM}) pairs are determined, the index assignment can be done.

For example Maultzsch et al. [37] studied large amounts of tubes and established a table on optical transition energies and RBM frequencies. They compared characteristic patterns of the experimental and theoretical data but no quantitative agreement between theoretical and experimental data was needed. Furthermore, no calculated transition energies or RBM frequencies are needed. As seen from figure 2.3 the transition energies as a function of diameter follow roughly $1/d$ dependence. Different chiralities deviate from this dependence resulting in V-shaped branches to it. The tubes with largest chiral angle (armchair) are closest to the line and the small chiral angle tubes (zigzag) the outermost. Let the (n_1, n_2) tube be the outermost tube of the branch. Then the neighboring tubes in the branch are

$$(n_1', n_2') = (n_1 - 1, n_2 + 2), \tag{2.11}$$

($n_1' > n_2'$.) The assignment is done by using these branches and comparing the experimental and theoretical plots. The plots are matched with each other by

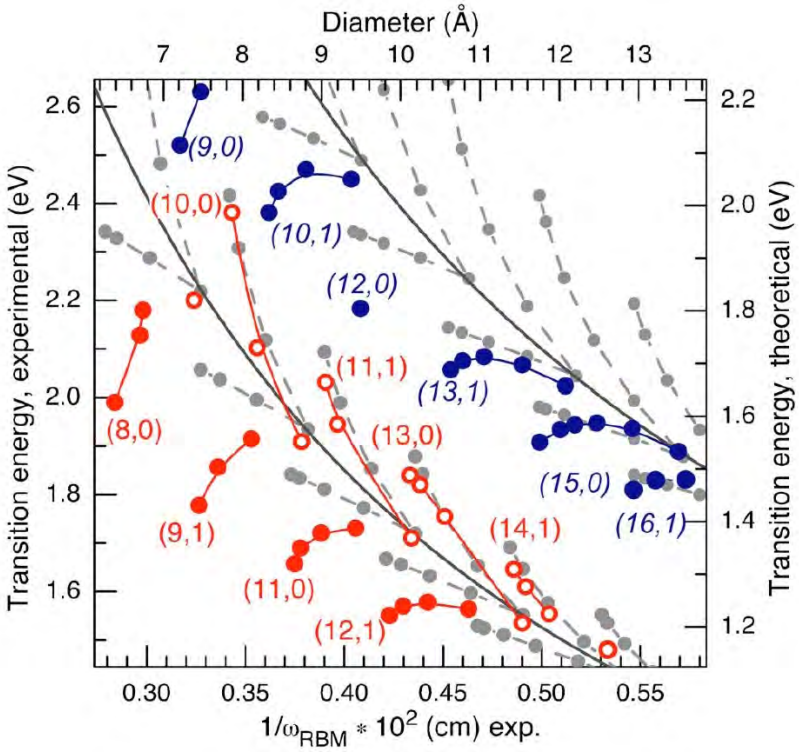

Figure 2.3: Kataura plot where second optical transitions of semiconducting nanotubes E_{22}^S (lower band) and first optical transitions of metallic nanotubes E_{11}^M (upper band) are shown. Large coloured dots are obtained from experimental data and small gray circles from theoretical calculations. The solid lines give the approximate 1/d dependence of the transition energies. The dashed lines indicate the V-shaped branches, where the chirality of the tube is related to its left neighbour (n, m) by $(n', m') = (n-1, m+2)$. The assignment in the experimental data is given for the first tube of each branch. The semiconducting tubes are divided into two families with $\nu = (n-m) \mathrm{mod}\ 3 = -1$ (full circles) and with $\nu = +1$ (open circles). Such plots can be made for higher optical transitions also. Adapted with permission from reference [37].

shifting and stretching one plot in respect to the other. This is analogous with tuning the coefficients α and B in equation (2.10). One key point is that the number of tubes within a branch is unambiguously determined by the construction of a nanotube from a graphene sheet which will exclude many possibilities. Further discussion on the accuracy of the method is given in reference [37].

The index assignment can be done also by comparing the excitation energy with the optical transition E_{ii} [31, 38]

$$E_{ii}(p,d) - \frac{\beta_p \cos(3\theta)}{d^2} = a\frac{p}{d}\left[1 + b\log\frac{c}{p/d}\right], \tag{2.12}$$

where θ is the chiral angle, $a = 1.049$ eV $\cdot$ nm, $b = 0.456$ and $c = 0.812$ nm^{-1} and $p = 1, 2, 3, 4, 5$ for $E_{11}^S, E_{22}^S, E_{11}^m, E_{33}^S, E_{44}^S$, respectively. It was also found that a correction term $\Delta E = \gamma/d$ with $\gamma = (0.305 \pm 0.004$ eV) is needed for higher transitions to reproduce the experimental data [31].

2.3.2 *D*-band

The D-band is observed in the $1300 - 1400 cm^{-1}$ range and it is common to all sp^2-hybridized disordered carbon materials. It comes from second-order Raman process where also the phonons which are inside the Brillouin zone become active, not only the phonons that are close to the Γ-point. The phonons that are close to K-points of the graphene Brillouin zone become active in nanotubes because of the defects (impurities or missing atoms), finite-size effects and molecules linked to the tube's sidewalls [39].

The behavior of the band is due to a double-resonance process. First an electron-hole pair is created when the incident photon is absorbed. The electron is then scattered by a phonon (or a defect) with wave vector $\vec{q}$ and scattered back by a defect (or a phonon) with wave vector $-\vec{q}$, recombining with the hole and emitting a scattered photon. [40]

2.3.3 *G*-band

The G-band mode occurs in the frequency range of $1500-1605 cm^{-1}$. It is derived from the double degenerate Raman-allowed optical E_{2g} mode of the graphene Γ-point. It is an intrinsic feature of nanotubes and it is related to vibrations that all sp^2-carbon materials have [29]. The double degenerate G-band peak of graphene is split into two peaks G^+ and G^-. The modes are polarized along the tube axis (LO) and along the tube circumference (TO) as shown in figure 2.4. The shape and position for the peaks depend strongly on the electronic properties of the tube. Actually the Raman G-band consist of more peaks than just the two main peaks (G^+ & G^-) especially in defective SWNTs due to double-resonance Raman process [41].

The most striking feature of the G-band is the well-defined difference in the line shapes of G^--peaks between metallic and semiconducting tubes as seen in

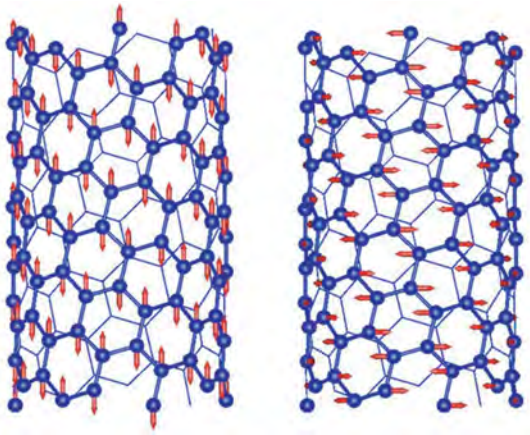

Figure 2.4: Tangential LO and TO phonon modes of SWNT. Adapted with permission from reference [42].

figure 2.5. Therefore, that feature is usually used to determine whether the tube is metallic or semiconducting. In the semiconducting tubes both peaks have a sharp Lorentzian line shape. But in the metallic tubes, the phonon line width of the LO phonon (G^--peak) is increased due to the electron-phonon coupling (EPC) caused by the Kohn anomalies (KA) [43]. Such anomalies are only present in the metallic tubes which have finite electronic density of states at the Fermi surface. The non-zero EPC is responsible for the broad, asymmetric Breit-Wigner-Fano (BWF) line shape which is given by [36]

$$I(\omega) = I_0 \frac{(1 + (\omega - \omega_{BWF})/q\Gamma)^2}{(1 + (\omega - \omega_{BWF})/\Gamma)^2}, \tag{2.13}$$

where I_0, ω_{BWF}, Γ and q are the maximum intensity, renormalized frequency, broadening parameter and the line shape parameter, respectively. Because the EPC affects only LO phonon of the metallic tube and increases the line width of the LO phonon, the TO phonon (G^+) remains showing a sharp Lorentzian line shape. Therefore the line shape of the lower frequency component between metallic and semiconducting tube is very different and it can be used to determine between the metallic and semiconducting character of the tube.

The splitting between the LO and TO modes in the semiconducting tubes can be explained in terms of curvature (see e.g. references [42, 43]. In the metallic tubes there has been a strong debate on the subject and different theories have been proposed [44–48]. In these theories the different behavior of the G^--band in semiconducting and metallic nanotubes is explained due to phonon-plasmon coupling in metallic nanotubes. All these theories are qualitative and fail to predict in a precise, quantitative way the observed features in Raman G-band. However, widely accepted results indicate that the splitting in metallic nanotubes is strongly induced by electron-phonon coupling and Kohn anomalies.

The Kohn anomaly softens only the LO mode which leads the lower frequency G^- peak to originate from the LO phonon. This is quite opposite compared to the semiconducting tube. The KA is furthermore responsible for the reduction of the LO phonon lifetime, which then increases the phonon line width [43].

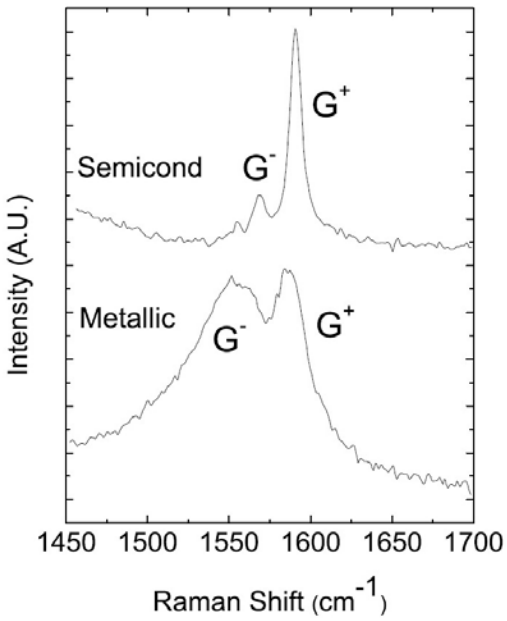

Figure 2.5: Raman G-band of semiconducting and metallic nanotubes. For semiconducting tubes there are two sharp Lorentzian peaks as for metallic the G^- peak is broad, asymmetric Breit-Wigner-Fano type of lineshape. Adapted with permission from reference [42].

2.4 Fabrication of CNT devices

This section begins with an overview of past of electrical transport measurements and the evolution of sample fabrication (subsection 2.4.1). Then subsection 2.4.2 describes the details of our fabrication processes for standard substrate supported SWNT-FET (singlewalled carbon nanotube field-effect transistor) devices.

The fabrication of CNT devices for electrical measurements consists of different processing steps. The most standard way includes the deposition of the nanotubes onto a substrate and then connecting them electrically to the measurement setup. There are many types of sample geometries depending on contacts, the environment of the channel or the gate configuration as illustrated in figure 2.6. Common CNT deposition methods include dispersing tubes into solu-

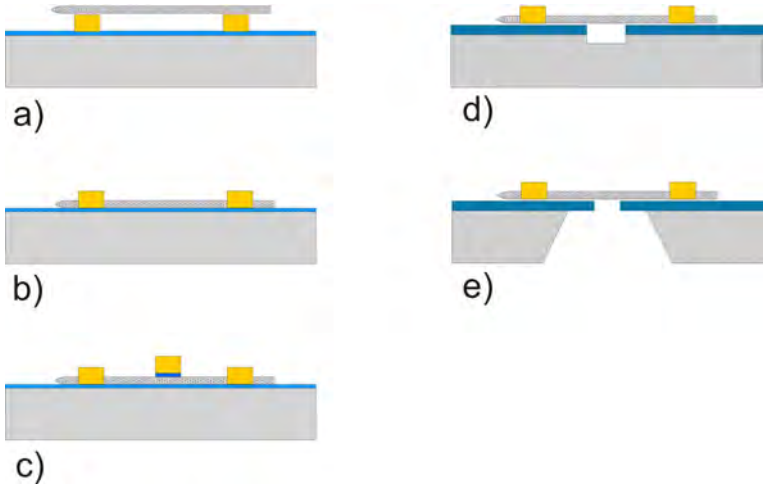

Figure 2.6: Typical concepts of CNT devices. **(a)** Bottom contacts with Si back gate i.e. the contact electrodes are fabricated before CNT deposition. **(b)** Top contacts with Si back gate i.e. contacts are made after CNT deposition. **(c)** Top-gated device with top contacts. Top gate is fabricated directly on top of a CNT channel with small dielectric in between. **(d)** Top contacted suspended device. The tube is hanging freely across a trench. **(e)** Suspended device across a through-wafer slit that allows TEM studies on the tube.

tion and spin them onto substrate or grow the tubes via CVD-method (chemical vapor deposition) directly onto substrate. More specialized methods include e.g. transferring the tubes or trapping the tubes between the electrodes using DEP (dielectrophoresis).

2.4.1 Advances in CNT device fabrication

Exploratory techniques

The beginning of experimental research on transport in single CNT's in the 1990's faced problems for which there were no precedents. Therefore there has been numerous exploratory techniques tried out that will be described in this section. This history is relevant for this work which also has been aiming for new untried measurement techniques.

STM lithography: The first electrical measurements of nanotube samples were made on bundles of multiwalled nanotubes by Langer et al. [49] published in 1994 and soon after first measurements on individual multiwalled samples were performed [50]. In these measurements the nanotube made with arc-discharge method were dispersed on top of a silicon oxide chip with prefabricated gold pads on it. After that a second layer of gold is evaporated followed by deposition of negative e-beam resist (ω-tricosenoic acid) by using Langmuir-Blodgett (LB) technique. Scanning tunneling microscope (STM) is used first to locate the tubes and then to expose the resist. After development of the resist the unprotected areas of gold are removed by argon milling [51]. The schematic of the sample processing is presented in figure 2.7.

Prefabricated pads: Almost at the same time Dai et. al. [53] and Ebbesen et al. [54] published their results on electrical transport measurements of individual MWNTs. Dai et. al. dispersed nanotubes on top of prefabricated gold pads and chose only those tubes in which the other end of the tube was on top of the gold pad and the other end directly onto the substrate. The other contact was done by bringing conducting AFM tip directly in contact with the tube. Ebbesen et al. used also prepatterned gold pads. The dispersed nanotubes were now connected to the pads by using focused ion beam deposition of tungsten (W). It was later assessed that the ion beam very seriously damaged the nanotubes. This method has not been used later despite the increased availability of ion beam instruments.

Dipping of tubes: In 1998 Frank et al. [55] studied MWNTs by dipping CNT fibers into the liquid metal mercury (Hg). The MWNTs were embedded into the fiber so that single rather long multiwalled tube was usually pointing out and by lowering it into mercury, so that only the single MWNT was inside the Hg, the transport measurements were possible to carry through.

Dielectrophoresis: Dielectrophoresis was first used to align carbon nanotubes [56] and soon also to place them between electrodes [57]. In this method an AC-electric field is generated between two electrodes which induce force affecting the

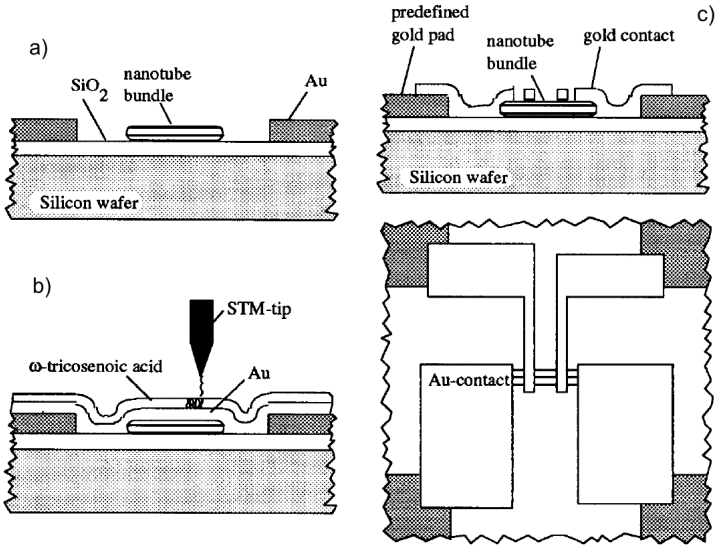

Figure 2.7: a) CNT bundles are deposited on a Si/SiO_2 chip with prefabricated gold pads on it. (b) 15 nm thick gold film is evaporated followed by deposition of Langmuir-Blodgett layers of negative e-beam resist (ω-tricosenoic acid). A STM is then used to locate the position of a nanotube or nanotube bundle between the predefined gold pad at tunneling voltages below 5 V and then bias voltage was increased in order to locally expose and to polymerize the LB resist layers from both ends of the nanotube towards the contact pads. (c) The LB-film acts as a negative resist and the unexposed parts of the resist layer can be removed by development in ethanol. Finally, the gold areas that were no longer protected by the LB-film could be removed by argon ion milling. The result of this process is an electrically connected nanotube or nanotube bundle. Adapted with permission from reference [52].

tubes. The first electrical measurements on DEP-trapped SWNT bundles were made by Krupke et. al. in 2003 [58] and later also FETs have been fabricated by trapping CNTs between electrodes [59].

Standard methods

The first transport measurements of singlewalled devices were published by Tans et al. in 1997 using a quite simple approach to fabricate bottom contacts (see fig. 2.6 (a)) [60]. They fabricated platinum (Pt) electrodes on top of a Si/SiO_2 substrate and deposited nanotubes produced by laser ablation method on top of the substrate. The suitable tubes, that were connecting two Pt electrodes, were then located using AFM. The measurement setup included also a third terminal aka gate which could be realized from the Si substrate which was separated from the tube with the help of a SiO_2 dielectric. Essentially these tubes were metallic in nature that showed semiconducting behavior at low temperatures.

After this more attention turned into singlewalled tubes since they represent better model system for 1 D conductor. In 1999 the same group demonstrated a room temperature transistor [61] using exactly the same fabrication method than before.

The most widely used method nowadays to fabricate CNT-FET devices, however, is to use e-beam lithography so that some marker and outer electrode structure is fabricated first on top of the substrate, then the nanotubes are deposited on the substrate, located with respect to the markers and finally connected to the outer electrodes with a second lithography step (top contact, see fig. 2.6 (b)). This method was first used by Bockrath et al. in 1997 [62] for ropes and after that for individual tubes as well [63].

When an increasing number of transport studies of SWNTs were available, it became clear that the contact between the semiconducting nanotube and the metal electrode plays a major role in transport characteristics [64–66] and operation of Schottky barrier transistor was introduced comprehensively [18]. Soon ballistic transport was realized also in semiconducting tubes by using proper contact metal (Pd) that matches the valence band of the average sized singlewalled nanotube [16] (p-type contacts). Many metals with different work functions have been tested ever since to make either p-type or n-type devices [16, 18, 67]. The work function, however, is not the only thing that is affecting at the interface because some additional tunnel barriers will form depending on the wetting properties of the metal [19].

Importance of gate structure

The effectiveness of gate plays a major role in CNT transistor transport characteristics. Many several gate configurations have been developed and next I will discuss most of them. The most universal configuration is the back gate configuration, where a thin dielectric layer (usually 300-500 nm thick SiO_2) is separating the tube from the Si chip. And then Si chip is used as a global gate. The gate capacitance of such device can be estimated as a wire on top of a plate which has capacitance per unit length of

$$C_g/L = 2\pi\epsilon_0\epsilon_r/\ln(4h/d), \tag{2.14}$$

where ϵ_r is the relative permittivity, or dielectric constant, h the thickness of the gate dielectric and d the diameter of the tube. There are then two obvious ways to improve the capacitance and hence the effectiveness of the transistor: choosing material with high dielectric constant or minimizing the distance between the tube and gate [19].

Local gate structures: Bachtold et al. [65] constructed a local gate just by evaporating Al lines on top of the substrate and using the proportioned native aluminum oxide Al_2O_3 (few nanometers thick) as a gate dielectric. The nanotubes were then deposited on top of the substrate and contacted.

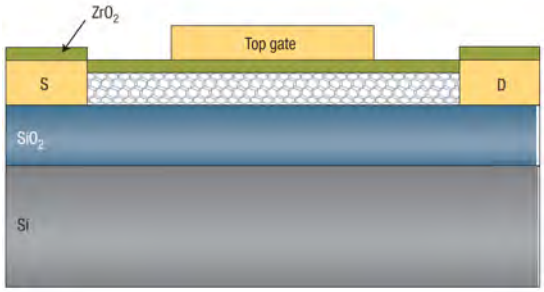

Figure 2.8: Sideview of a SWNT-FET with ALD-ZrO_2 as the gate dielectrics (source S, and drain, D electrodes). The nominal thickness of ZrO_2 used is 8 nm. The thickness of thermally grown SiO_2 on the Si substrate is 500 nm. Adapted with permission from reference [68].

Top-gating CNTs is a different approach to make the device more efficient. Here the tubes are more embedded by the gate compared to back gate structures which increases the performance of the gate. The fabrication starts by simply doing normal CNT-FET. A thin film of dielectric material is then deposited on top of the device and finally a local top gate is fabricated on top of that like in figure 2.8. Dielectric materials like SiO_2 [69] or high-κ materials such ZrO_2 [68] and HfO_2 [70] have been succesfully used.

Split gates have been used to study quantum dot behavior and $p-n$ junctions in CNTs. One possibility to fabricate such structure is to pattern split gates on top of the Si/SiO_2 surface and then growing another layer of SiO_2 to the gate dielectric like Lee et al. [71]. After that the device fabrication is trivial. Schematic of split gate structure is shown in figure 2.9. Such split gates are combined later on also in suspended devices like in reference [72].

Wrap-around gate structure: The most effective gate behavior should form if the gate is wrapped around the nanotube. This has been also realized in 2008 by Chen et al. [73]. They used atomic layer deposition (ALD) process to deposit dielectric (Al_2O_3) and gate electrode (tungsten nitride, WN) around suspended CNT. The tubes are then dispersed into a solution and deposited onto the substrate. Since the wrap-around gate is now everywhere the gate is etched away from the ends so that contacts can be done normally.

2.4.2 Fabrication steps of samples used in this work

Substrate supported CNT devices were fabricated with standard e-beam lithography steps on top of a Si/SiO_2 wafer forming top contacts to the tube as presented in figure 2.6 (b). Highly boron-doped single crystal silicon wafer was used as the starting material. The wafer was oxidized in a high temperature oven ($T = 1100°C$) in oxygen flow for 5 h in order to have thin, around 300 nm

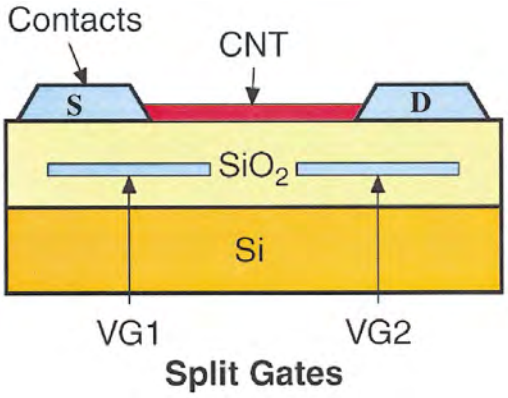

Figure 2.9: Schematic cross section of SWNT $p-n$ junction diode. The split gates VG1 and 2 are used to electrostatically dope a SWNT. For example, a $p-n$ junction with respect to the S contact can be formed by biasing $VG1 < 0$ and $VG2 > 0$. Adapted with permission from reference [71].

thick SiO_2 layer on top of the Si. After the oxidation the wafers were precut from the back side with silicon saw to 5 mm x 5 mm pieces so that each bigger piece contained a 5x5 matrix of these precut pieces.

Commercial Microchem positive e-beam resists were used as masks for e-beam patterning. Two layers of different resists were used to form the undercut. The first layer was either PMMA A3 (poly(methylmethacrylate)) dissolved in anisole having a molecular weight (MW) of 495 u or copolymer called polymethyl methacrylate-co-methacrylic acid dissolved in ethyl lactate (PMMA-MAA EL3). The second layer was PMMA A 2 % with a molecular weight of 950 u. The resists were spin coated on the substrate with 3000-4000 rpm for first layer and 4000-6000 rpm for second layer. After each spinning the sample was baked on a hot plate (160 $^{\circ}C$) between 2 and 3 minutes to evaporate solvent and solidify the resist.

The lithography procedure contained two different patterning steps. In the first step the 6x6 marker grid matrix and 28 electrodes around it were patterned for the location of the nanotubes as presented in figure 2.10. The tubes were deposited then on top of the surface and located with an AFM. Finally a second exposure was done to contact the nanotubes to the outer electrodes. The patterning was performed using Raith e-line electron beam writer and Elphy Quantum 4.0 lithography software always with 20 kV acceleration voltage and 500 µm writefield. In the first lithography step two different aperture sizes, and hence beam currents, were used: the outer (and bigger) components were done using a 120 µm aperture within a 2500 µm working area as the inner and smaller components were patterned with 30 µm aperture and 500 µm working area. The exposed pattern was then developed in 1:3 of MIBK (methylisobutylketone):IPA (isopropanol) for 40–50 s when using only PMMA. Copolymer, if used, was then

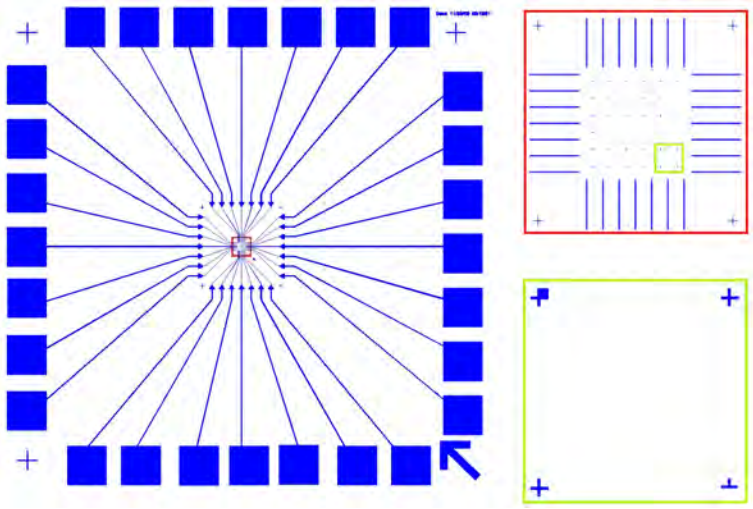

Figure 2.10: Structure design of the first patterning where marker crosses for the second patterning, bonding pads and electrodes to the marker grid are seen. Red inset: Marker grid for locating the nanotubes. Green inset: individual markers.

developed in 2:1 of methanol:methoxyethanol for ∼5 seconds.

An additional cleaning step in RIE was performed after development to get the residual resists away from the patterned areas. Oxford Instruments Plasmalab80Plus RIE (reactive ion etcher) was used for 30 s in 50 sccm oxygen flow and 40 mTorr pressure, 30 °C temperature and 60 W power. The evaporated metal was chosen to be palladium (Pd) because it makes good ohmic contacts to the CNT as described earlier. An additional sticking layer of Ti (∼5 nm) was used in the first exposure step to improve the adhesion before evaporating the ∼25 nm Pd layer. The evaporation was done either in Balzers BAE 250T HV (high vacuum) electron beam evaporator or by using a UHV (Cryo-torr 8, Telemark TT 10) evaporator with improved vacuum and hence film quality.

The nanotubes were deposited after the first exposure step. Both SWNT and MWNT material was used depending on the application. SWNTs were commercial Nanocyl 1100-series single-walled carbon nanotubes, which have average diameter of 2 nm. These tubes are produced via a catalytic carbon vapor deposition (CCVD) process [74]. The MWNT material was obtained from a collaborating group produced with arc-discharge method [75] or from Sigma-Aldrich produced with same kind of process. The CNT powder was dissolved in 1,2-dichloroethane and sonicated using either bath sonicator or more effective finger sonicator before deposition onto the substrate. The concentration of the tubes varied with the suspension so each deposition was made with several droplets of the tube suspension spun onto substrate. Really long SWNTs (∼tens of micrometers) were also used. These tubes were grown directly on the substrate with a substrate CVD method [76] at Helsinki University of Technol-

ogy (nowadays Aalto university) in professor Esko Kauppinen's NanoMaterials group. Later, also our own CVD setup was established on-site for tube synthesis as described later.

The 6x6 alignment mark matrix was mapped with an AFM (Veeco Dimension 3100 series) using tapping mode. The 10 μm x 10 μm images were captured so that 4 alignment marks were always seen and suitable tubes were chosen to be connected. The second exposure step was done with the same parameters as the first one. After development the Pd layer was directly evaporated to a form good contact with the tube.

2.5 Experimental methods

2.5.1 Conductivity measurements

The sample was first attached into 28 channel chip carrier by using varnish and measurements wires were attached to it by using a wire bonder. All low temperature measurements were carried out in a home-built dipstick in vacuum inside a shielded room. The dipstick has a silicon diode temperature sensor from Lakeshore and the lowest achievable temperature is the liquid helium boiling point (4.2 K). We used two terminal measurements where the same leads are used to feed the voltage and measure the current. Usually four-probe measurements in CNT devices coincide with 2-probe measurements because the metal contacts separate the nanotube into segments disturbing the electron flow in the tube [77].

The voltages were supplied from programmable DC voltage sources (Yokogawa 7651), one for source-drain voltage and one for gate voltage controlled by GPIB (general purpose interface bus)) card. The input and output signals were measured with a 18 bit data aquisition (DAQ) device (National Instruments PXI 6281 M) and controlled via LabView software. The measurements are done by applying the source-drain voltage through the tube and measured signal is fed through a low noise current preamplifier (DL instruments 1211) before readout. Maximum range for gate voltage was from -30 V to 30 V.

2.5.2 Raman spectroscopy

The Raman measurements were done with a homemade Raman spectrometer in a back-scattering geometry. The chip carrier was mounted to the socket which was placed onto XYZ-stage in a vertical position. The stage consists of a manual stage (Newport ULTRAling 462-XYZ-M) for coarse positioning and a XYZ-piezoscanner (Attocube ANPxyz101) for fine positioning. The spectral resolution for this setup was measured to be 3-4 cm^{-1} with 600 g/mm grating.

Two different laser sources were used: Alphalas Monolas-532-100-SM with 532 nm excitation wavelength and Melles Griot 25-LHP-991-230 with 632.8 nm excitation wavelength. The excitation light was focused to a sample with a

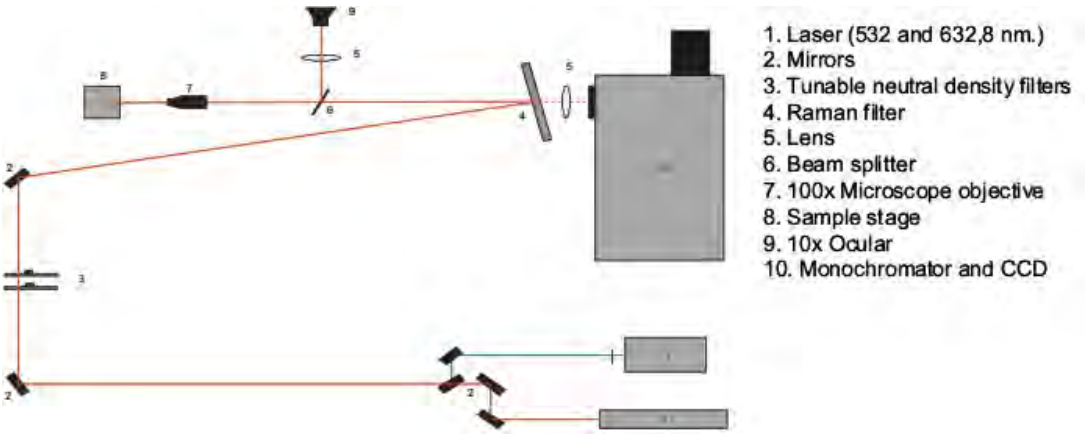

Figure 2.11: Raman measurement setup.

microscope objective (Olympos 100x, 0.70 N.A.) and the backscattered light was collected with the same objective. Also a beam splitter, an extra lens and a 10x microscope ocular was used to construct an optical microscope with 1000x magnification for positioning the laser spot in the desired area of the sample. The Rayleigh scattering was filtered away with a Semrock edge filter that allows to record the Raman spectrum down to 70 cm^{-1}. The scattered light was dispersed in a 0.5 m imaging spectrograph (Acton SpectraPro 2555i) using 600 g/mm grating and finally detected with an EMCCD camera (Andor Newton EM DU971N-BV) using a 60 μm slit width. A schematic drawing of the measurement setup is seen in figure 2.11. In typical measurement the signal was accumulated from 200 measurements with 2 s data collecting time to improve the signal-to-noise ratio.

2.6 Results

The samples were fabricated on top of the Si/SiO_2 substrate as described in section 2.4. The devices were then characterized first by probing transport measurements from room temperature down to 4.2 K and after that performing Raman measurements in ambient conditions. In total 4 devices were measured: two were characterized as metallic SWNTs, one as a semiconducting SWNT and one as a semiconducting bundle or doublewalled (DWNT) tube. The data collected from Raman and AFM measurements is presented in table 2.1. Furthermore, one tens of micrometer long CVD-grown tube was studied to see structural uniformity of the tube.

Table 2.1: Data collected from Raman measurements and AFM measurements on four different devices.

	(n,m)	ω_{RBM} (cm^{-1})	d_{RBM} (nm)^b	d_{RBM} (nm)^c	d_{AFM} (nm)	L_c (nm)	ω_D (cm^{-1})	ω_G (cm^{-1})
M1	(13,1) or (13.2)	218.3	1.08	1.07	0.8	360	1322.0	1554.1/ 1589.2
M2	(13,4)	193.9	1.22	1.22	1.0	750	1321.6	1537.9/ 1587.7
S1	[a]	103.5	2.48	2.67	2.7	880	1345.5	1559.8/ 1587.3
S2	[a]	133.1/ 97.0	1.85/ 2.68	1.92/ 2.91	1.8/ 2.6	850	1341.1	1578.9/ 1592.2 (532 nm) 1579.1/ 1597.7 (633 nm)

[a] several possibilities

2.6.1 Metallic devices

Raman spectrum of the devices was recorded using 632.8 nm (1.96 eV) excitation and no spectrum was obtained using 532.0 nm (2.33 eV) excitation. Both tubes show a clear spectrum with sharp RBM peak and G-band structure indicating them as metallic nanotubes (see figure 2.12 (a) and 2.12 (c)). The diameter of the tubes were calculated using equation (2.10) with coefficients $\alpha = 217.8$ cm^{-1} and $B = 15.7$ cm^{-1} obtained from reference [31] which are showed to work especially well for small-diameter tubes. When modifying the equation as a function of ω_{RBM} we can determine the diameters. Also different coefficients ($\alpha = 217.8$ cm^{-1} and $B = 15.7$ cm^{-1}) were used which were reported to work very well for suspended tubes [32]. The diameters were furthermore measured with the atomic force microscope (AFM) to cross check the values. The different coefficients give roughly same results for smaller tubes and the variation is more pronounced in thicker tubes as seen from table 2.1. Thus the diameter results for metallic tubes are in practice the same. The chiral index assignment was done by following the method discussed in section 2.3.1 i.e. comparing the measured RBM frequencies and the excitation energy E_{laser} to RBM frequencies and transition energies determined by Maultzsch et al. [37]. The SWNT was assumed to have E_{ii} within a resonant window $\Delta E = E_{laser} \pm 0.10$ eV. Such index assignment for M1 gave two possibilities: $(13, 1)$ or $(12, 3)$. $(12, 3)$ was concluded to be more likely, since our measured RBM frequency is closer to that (218.3 cm^{-1} compared to 217.4 cm^{-1}). The same treatment was done also for M2 $(13, 4)$ being the closest tube. It has to be mentioned, however, that such assignment is not very accurate. The D-band is strong in both tubes indicating

the presence of defects or contamination e.g. amorphous carbon at the tube's surface.

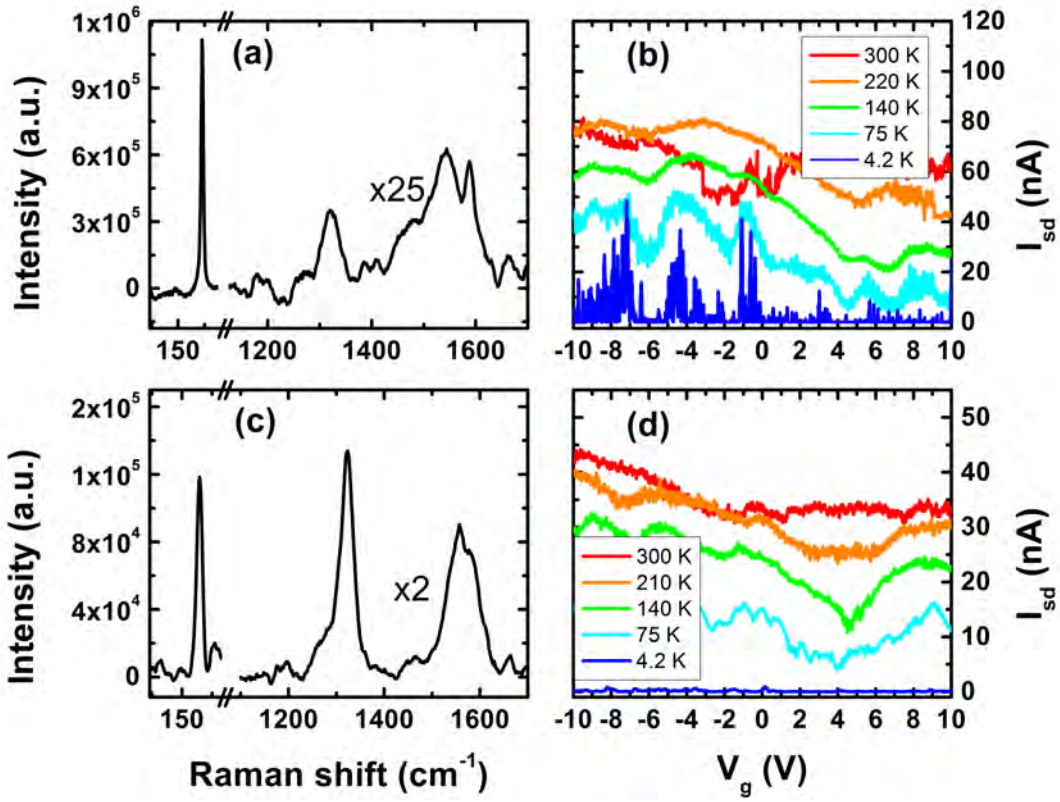

Figure 2.12: (a) Raman spectrum from sample M1. The right-hand section of the curve is smoothed and multiplied by a factor of 25 for clarity. (b) Corresponding gate curve at 10 mV source-drain bias. The color of each trace shows the sampling temperature. No clear gate modulation is present but a clear Coulomb blockade oscillations are visible at temperatures < 140 K. (c) Raman spectrum from sample M2 The right-hand section is multiplied by a factor of 2 for clarity. (d) Corresponding gate curve at 10 mV source-drain bias. Note that the gate curves are presented in linear scale. Adapted with permission from the paper **A.I.** from this thesis.

Transport measurements are shown in figure 2.12 (b) and (d). Both samples exhibit weak gate dependency throughout the whole gate range from -10 to 10 V. The resistance in room temperature for device M1 is 125 kΩ and for M2 298 kΩ both having linear $I - V$ curve. Sample M1 starts to show clear Coulomb blockade oscillations when cooling it down with a peak period centered at 242 mV as seen in figure 2.13. Furthermore, $I - V$ characteristics shows non-linear behavior at low temperatures which can also be explained with Coulomb blockade. It is well known that quantum dots form along the CNT channel

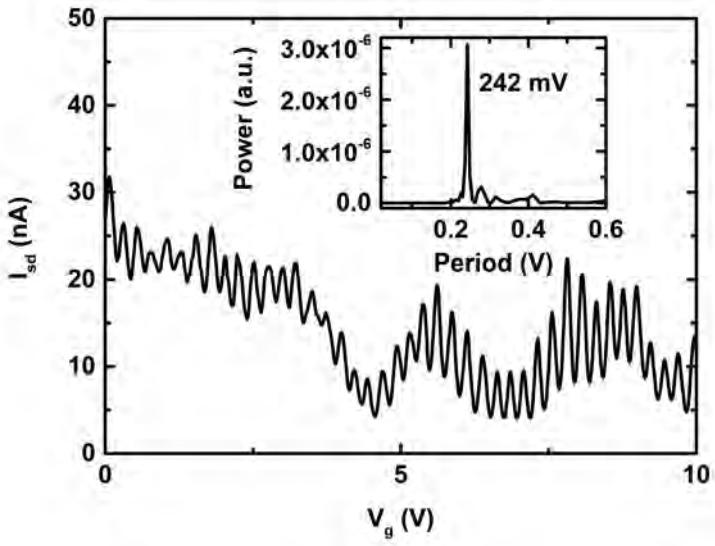

Figure 2.13: Coulomb blockade oscillations of M1 at 75 K. Inset: Fast Fourier transform (FFT) revealing the peak period centered at 242 mV.

due to e.g. defects or disorder caused by the underlying substrate [19]. Clear oscillations as a function of gate voltage would imply that one dot is dominating the characteristics. Non-linear $I-V$ is also present in sample M2 but no clear oscillations are visible in the gate curve. One plausible explanation of the plateau in M2 would be the presence of a small band gap in the tube. Based on Raman measurements, the tube was indexed as $(13,4)$ which is actually a small band gap tube with a band gap value of 31 meV [78]. Transport measurements give also a rough estimate of the size of possible band gap. This can be done by measuring the width of the plateau as accurately as possible in the lowest conducting gate voltage [79] as is shown in figure 2.14. The estimate of the band gap is $29-32$ meV which is in excellent agreement with the theoretical value. Tube M1 which is assigned as either $(13,1)$ or $(12,3)$ is also a small band gap tube with gap values of 50 meV or 43 meV, respectively. However, the strong Coulomb blockade oscillation drowns the possible signal originating from the band gap but these oscillations can be used to estimate the gate efficiency factor. The period of gate voltage peaks is [62] $\Delta V_g = (U+\Delta E)/e\alpha$, where $U = e^2/C$ is the charging energy to add one electron in the quantum dot, C the total capacitance of the device, e electron charge and α the gate efficiency factor [79]. The threshold voltage of conduction is roughly [62] $V_{max} = U+\Delta E = 31$ mV and thus we get an efficiency factor of $\alpha = 0.129$. If taking values for charging energy and level spacing used in references [62] and [79] ($U = 14$ eV$/L$ (nm) and $\Delta E = 0.5$ eV$/L$ (nm)) we get the efficiency factor of 0.166 which is consistent with the experimental result

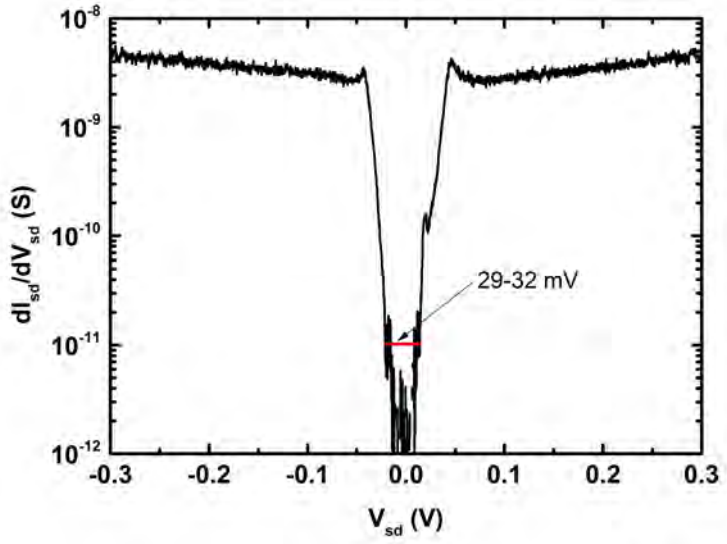

Figure 2.14: dI_{sd}/dV_{sd} vs. V_{sd} curve at 4.2 K and at zero gate voltage for band gap determination of tube M2. The estimate for the band gap is $29 - 32$ meV.

we have obtained.

2.6.2 Semiconducting devices

Raman spectrum of device S1 was recorded using 532 nm excitation and no signals were seen when using 632.8 nm (2.33 eV) excitation (see figure 2.15 (a)). The index assignment was attempted by comparing the excitation energy with the energies of E^S_{55} and E^S_{66} transitions (see section 2.3.1). As a results several potential candidates were obtained including $(21, 19)$, $(24, 16)$ and $(22, 17)$. The features of the G-band peaks clearly point towards semiconducting tube but anomalously the G^--peak is more intense than the G^+-peak the ratio of the peaks being 1.6. Normally the ratio of the peaks was reported by Jorio et al [80] to lie between 0.1 and 0.3. However, similar effect was also reported in the same study by Jorio et al. They suggested that the electronic transition energy E^S_{ii} satisfies a resonance condition for the incident photon. Furthermore, the lower energy electronic transition $E^S_{(i-1)(i-1)}$ satisfies the resonance condition for the scattered photon. If either of the G-band modes is very close to the scattered photon energy, that particular mode is strongly enhanced. So the E^S_{ii} and $E^S_{(i-1)(i-1)}$ transitions should lie within the phonon energy of the specific tube. They found that condition from ~ 1.6 nm thick tubes where E^S_{44} and E^S_{33} transitions fulfill the condition (see figure 2.16). Furthermore, they discussed that such condition should be present for the tubes having diameter close to 2.5 nm

with the excitation energy of 2.54 eV between E_{66}^S and E_{55}^S. Our findings can be explained with the same kind of resonance condition. If calculating the transition energies using equation (2.12) with diameter determined by using coefficient values for RBM-equation (2.10) like in reference [31] (leads to tube diameter of 2.48 nm), the transition energy E_{66}^S is too high to fit the observations. Instead calculated transitions fit well for diameters between 2.65 nm and 2.7 nm. Then the possible chiralities would be either $(21, 19)$, $(24, 16)$ or $(22, 17)$. AFM measurements give tube diameter of 2.7 nm which would fit the resonance window. Furthermore, if using coefficients obtained from reference [32] we get the tube diameter to be also 2.67 nm. Thus these findings favour the relation from reference [32] to work better in the thick tubes. The transport measurements seen

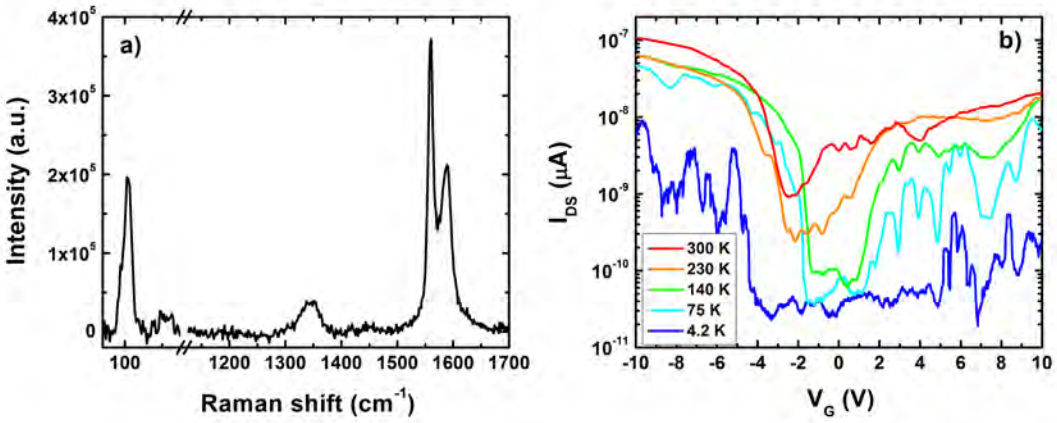

Figure 2.15: (a) Raman spectrum from sample S1. (b) Corresponding gate curve at 10 mV source-drain bias. The color of each trace shows the sampling temperature. Adapted with permission from the paper **A.I.** from this thesis.

in figure 2.15 (b) clearly confirms the semiconducting behavior of the tube.

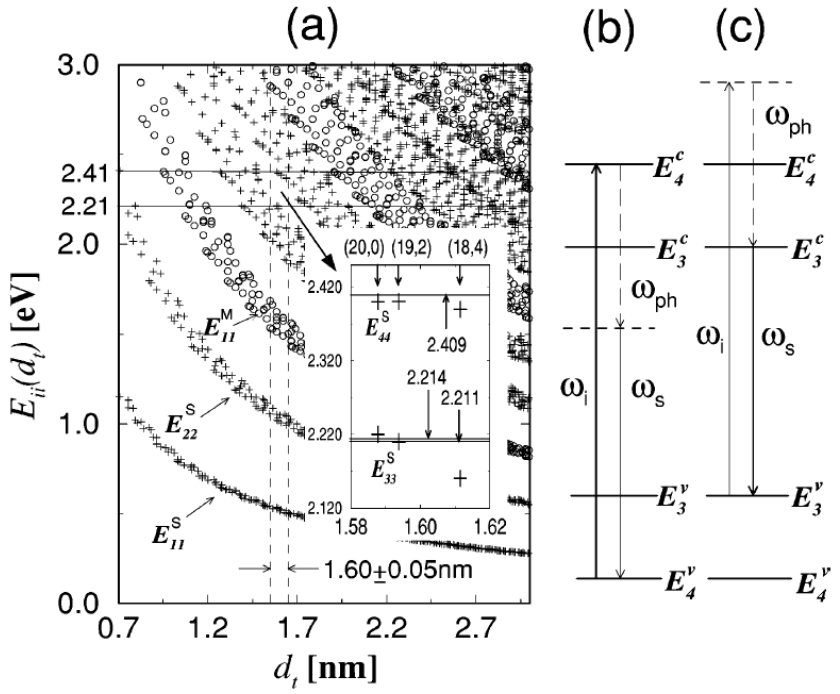

Figure 2.16: Special resonance condition. Plot of the electronic transitions E_{ii} for SWNTs with diameters between $0.7 < d < 3$ nm as a function of diameter, obtained from tight-binding calculations (Ref. [9]) with $\gamma_0 = 2.90$ eV. Crosses give the E_{ii}^S values for semiconducting SWNTs and circles give E_{ii}^M values for metallic SWNTs. The inset shows an enlargement of the region where the crosses correspond to the E_{33}^S and E_{44}^S electronic transitions for the three SWNTs with similar diameters ~ 1.60 nm. The vertical lines indicate the incident photon energy $E_{laser} = 2.409$ eV, and the scattered photon energies for the ω_G^+ ($E_{laser} - E_{ph} = 2.211$ eV) and ω_G^- ($E_{laser} - E_{ph} = 2.214$ eV) scattering processes. (b) and (c) show schematic figures for the two possible scattering processes for SWNTs with $d = 1.60 \pm 0.05$ nm (vertical dashed lines in (a)), where resonance can occur with either (b) the incident photon, or (c) the scattered photon ($E_{laser} - E_{ph} \sim 2.41 - 0.20 = 2.21$ eV). Adapted with permission from reference [80].

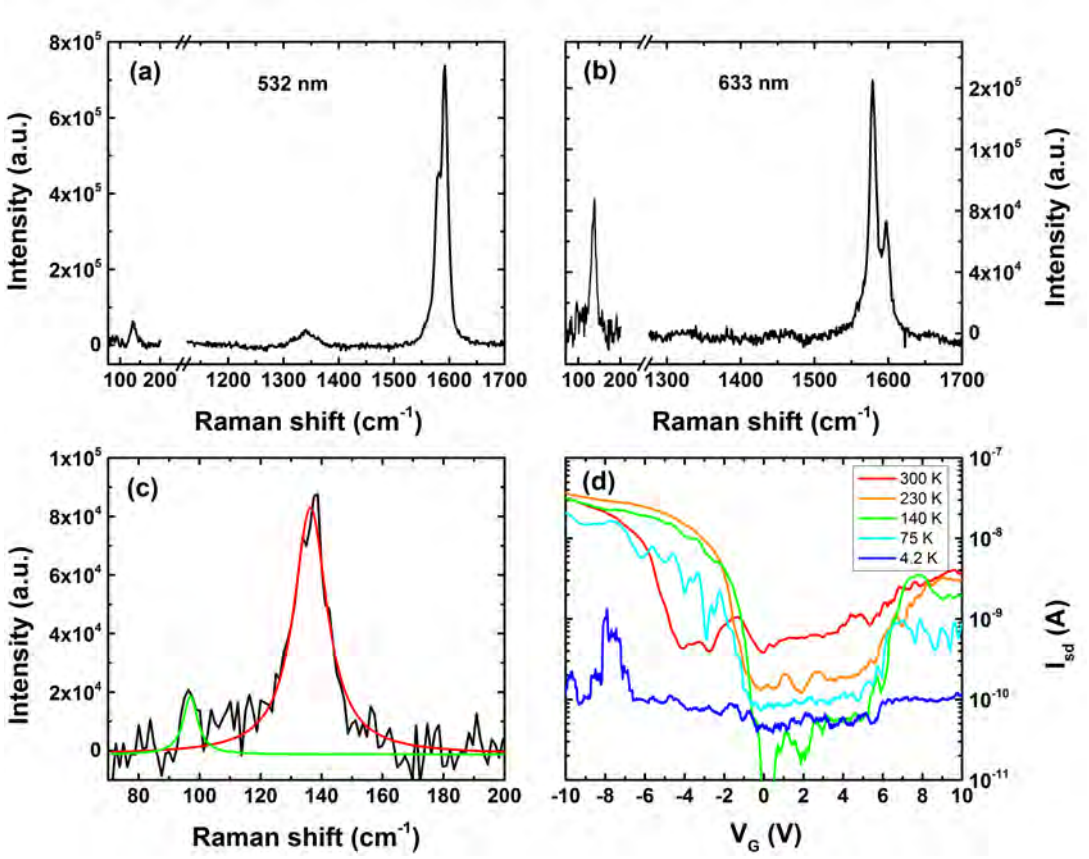

Figure 2.17: (a) Raman spectrum from sample S2 measured by using 532 nm excitation. (b)Raman spectrum of the same sample using 632.8 nm excitation. (c) Raman spectrum of the RBM region observed using 632.8 nm excitation. Green and red lines show Lorentzian fits to the data. (d) Corresponding gate curve at 10 mV source-drain bias. The color of each trace shows the sampling temperature. Adapted with permission from the paper **A.I.** from this thesis.

The Raman spectrum of device S2 shown in figure 2.17 (a) is measured using 532nm excitation. The *G*-band points towards semiconducting tube and the *D*-band is relatively weak. The semiconductivity is furthermore confirmed with the transport measurements as shown in figure 2.17(d). The RBM peak lies at 133.1 cm^{-1} which gives diameter of 1.9 nm. This is, however in clear disagreement with the AFM data that indicates the diameter to be around 2.6 nm. Raman spectrum was observed also with the 632.8 nm excitation as shown in figure 2.17 (b). Interestingly, the G-band features are totally different while the RBM remains the same within the calibration accuracy. With the 632.8 nm excitation, also another very weak RBM peak is observed at 97.0 cm^{-1} (see figure 2.17 (c)). This would then lead to a diameter of > 2.6 nm the exact value depending on the coefficients of equation (2.10). This is also consistent with the AFM value. Furthermore, if studying the AFM data closer, a shoulder

is observed in the cross-section data of the tube at the height of $\sim$ 1.8 nm which then would fit well with the observations of Raman data. Thus, the device is most likely a bundle of two tubes or then a double-walled tube. The G-band shows similar anomalous intensity ratio than S1 in 632.8 nm excitation which is furthermore absent in 532 nm excitation. This can be explained as a superposition of the smaller and larger tubes. It is impossible to simultaneously satisfy that the smaller tube is in resonance with both excitation wavelengths and that it has similar resonance condition than S1. For the larger tube such condition can be expected. The tube diameter obtained using coefficients form reference Meyer et al [32] gives a diameter of 2.91 nm which indeed would satisfy the resonance condition giving candidates such as $(21, 19)$, $(24, 16)$ and $(22, 17)$. The RBM of the smaller tube is observed also with both excitations so the tube has the resonant transitions for both excitation energies. From the Kataura plot it is obvious that the transitions in question have to be E_{33} and E_{44} and equation (2.12) gives several possibilities for indices such as $(16, 11)$ and $(14, 13)$.

2.6.3 Structural uniformity of long SWNT

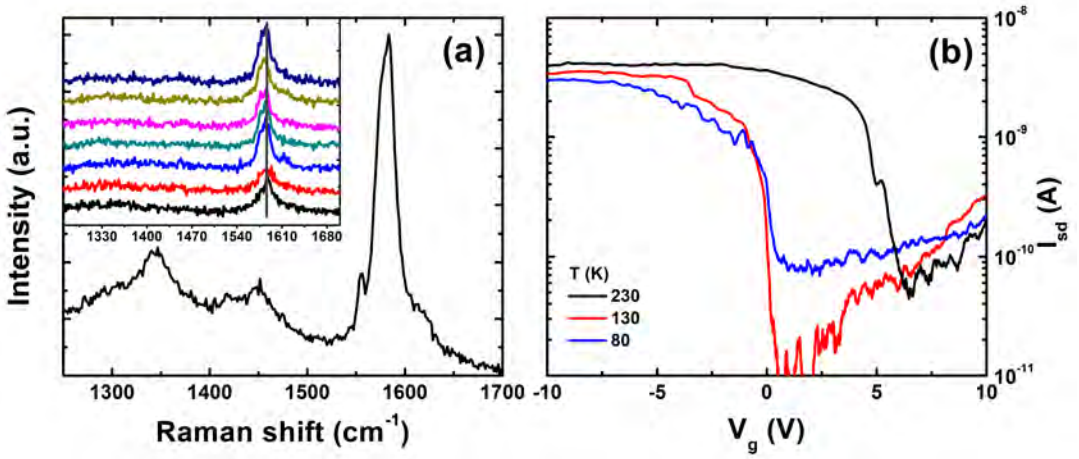

Figure 2.18: (a) Raman spectrum of a long CNT device. G-band indicating semiconducting tube and D-band is rather weak. Inset: Raman spectra taken at various positions along the tube axis indicating structural homogeneity within the tube. The separation of the positions is roughly 1 µm. The different plots are shifted upwards for clarity. (b) Source-drain current I_{sd} as a function of gate voltage V_g measured with 10 mV bias voltage at three different temperature indicating semiconducting behavior. Adapted with permission from the paper **A.II.** from this thesis.

One really long CNT device having a channel length of $\sim$ 20 µm was studied to check structural uniformity of such device. The sample processing is similar

to the shorter devices but the tubes were grown directly onto the substrate at Aalto University. The details of the growth are described in references [76, 81]. Raman spectrum of the device is given in figure 2.18 (a). The features of G-band clearly point towards semiconducting tube. Unfortunately RBM frequency is not visible but the AFM measurements give a diameter of $\sim$ 2.8 nm. The diameter seems to be the same at different locations along the tube. The D-band intensity is quite weak and broad and thus the tube seems to have low defect density. Furthermore, our laser spot size is $\sim$ 500 nm so it is possible to perform Raman measurements in different locations along the tube. This is seen at the inset of figure 2.18 (a). The G^+ peak stays put as the G^- peak seems to shift a little bit. Nevertheless, these two findings indicate a high quality of the tube without noticeable structural changes along the tube axis. The transport measurements furthermore confirm the tube to be semiconducting.

Chapter 3

Suspended CNT structures

The motivation to fabricate suspended samples was to combine transport measurements and optical spectroscopy with chirality indexed SWNTs i.e. knowing the electric structure of the tube. Here suspended means that the path for electrons is fully free i.e. the tubes are suspended over a slit. This will need more sophisticated sample geometry and sample processing and fabrication of such samples is described in this chapter. Before that a brief literature overview is given from the field of suspended CNTs.

3.1 Overview of the suspended CNT structures

Experimental studies of the elastic properties of CNTs required freely suspended structures. 1D conductors are also very sensitive to the surrounding environment where phonon relaxation and thermal conduction are major issues. Therefore suspended tubes show ideal transport properties like single quantum dot behavior [82]. The first study of suspended CNTs was published in 1999 by Salvetat et. al. dealing with elastic properties of CNTs. They dispersed SWNT bundles on top of a porous, polished alumina ultrafiltration membrane [83]. Almost at the same time Walters et. al. had a different approach to fabricate the suspended samples [84] which is presented in figure 3.1. They first deposited CNT bundles on top of a Si/SiO_2 chip, sealed the bundle by evaporating contacts and then etched the SiO_2 in aqueous HF (hydrogen fluoride) solution using contacts as an etching mask in order to get a section of tube that is freely hanging. An additional KOH etching can be done to get the trenches even deeper. Basically the same method has been used by other groups as well like in refs. [85, 86].

Tubes have to survive in this kind of process quite a hard chemical treatment that can affect the tubes [87], and therefore this kind of sample processing isn't necessary optimal especially for high quality transport measurements. So another processing branch was developed by Tombler et al. when they studied electromechanical properties of CNTs [88] by first opening the trench to SiO_2 and patterning a catalyst area next to the trench. Then the CNTs are grown via CVD method over the trench and finally metal electrodes are connected to

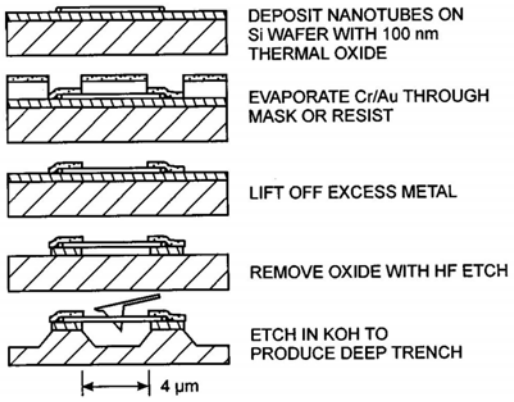

Figure 3.1: Fabrication method of suspended CNT sample for elasticity measurements by Walters et. al. Adapted with permission from reference [84].

the tube by using electron beam lithography (EBL). In this experiment, the electrodes are located around 2 µm away from the edges of the trench. This method presented by Tombler et. al. is developed further to introduce local gate electrode to the bottom of the trench [89] (see figure 3.2). The fabrication process varies a little bit compared to previous trench structures because here an extra Si_3N_4 layer is used as a mask on top of the SiO_2 layer. After making the opening to Si_3N_4 by using RIE the trench with undercut profile is etched in HF and prefabricated electrodes as well as the local back gate are patterned into the substrate. Finally tubes are grown from the catalyst islands deposited on top of the source and drain electrodes. The key factor here is not to etch the whole SiO_2 layer away so that the local gate is not connected to Si back gate. This technique is probably the one that has been used most widely, since the quality of the contact is relatively good and especially the tubes can be grown

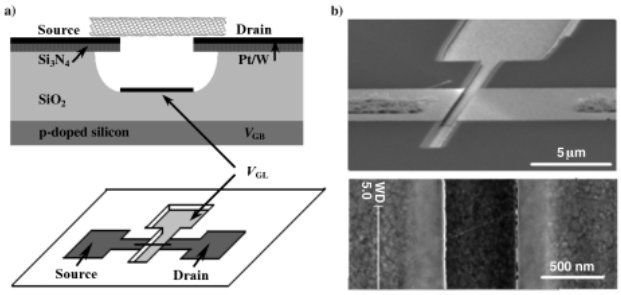

Figure 3.2: a) A schematic representation of the device structure; b) SEM images of a device consisting of a single suspended SWNT and two gates (local gate V_{GL} and global back gate V_{GB}). Adapted with permission from reference [89].

with really high quality without any further processing steps. The limiting factor is though that only certain electrode metals can withstand the high growth temperatures. First experiments were done with Mo electrodes [90] but the most standard material is to have W/Pt layers since Pt makes better contacts to the tube [89].

One interesting technique to overcome the problems discussed earlier is to directly transfer the nanotube on top of the target substrate i.e. direct printing [91]. Sangwan et al. grew SWNTs on a separate chip that was then pressed against a target chip with controllable pressure. The nanotubes stayed on top of the prefabricated gold electrodes and some tubes crossed the spacing between the two electrodes forming the suspended CNT device [87]. This kind of method is nowadays widely used with the CNT thin film transistors (TFTs) [92].

Another slightly sophisticated way is to grow the tube(s) in desired locations like in reference [93]. They patterned pillars to the quartz substrate and then grew the tubes between the pillars. By using markers they could press the pillars against the target chip so that the tube was transferred on top of the electrodes (see fig. 3.3). With the same method even more complex devices including split gates have been fabricated [94].

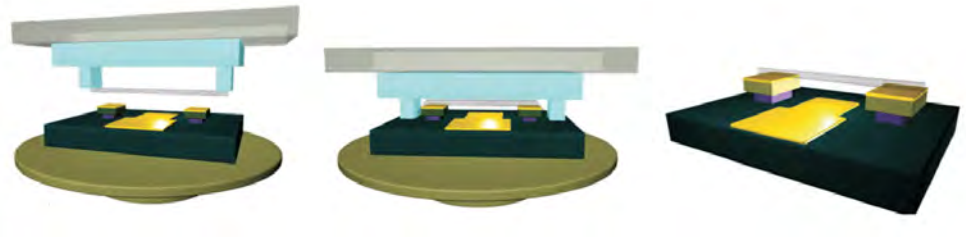

Figure 3.3: Schematic of direct transfer procedure. A suspended SWNT grown on a quartz substrate is mounted upside-down on a blank mask, and a device substrate with prefabricated electrodes is placed on the stage of the contact aligner (left panel). The quartz substrate is aligned to the device substrate and subsequently brought into contact by lifting the stage (middle panel). SWNTs are cut off at the contact points and span across the electrodes (right panel). Adapted with permission from reference [93].

Jiao et al. encapsulated nanotubes into a PMMA layer [95]. The tubes were grown normally into a Si/SiO_2 substrate and suitable tubes were chosen. Then the tubes were encapsulated into PMMA mediator and transferred inside the mediator on top of the desired location in the target chip. After dissolving the PMMA, the tubes stayed at the proper position. This method is suitable for normal as well as suspended structures but on the other hand resist can foul the surface of the tube.

3.1.1 Sample structures for combining TEM measurements

One ambitious goal is to perform measurements on chirality indexed nanotubes. The most reliable way to check the indices is to perform electron diffraction (ED) measurements in a transmission electron microscope (TEM). Unfortunately ED measurements need fully clear optical path which causes many problems into sample fabrication. First attempts to combine transport measurements with TEM was done by Kasumov et al. in 1999 [96]. There they fabricated a Si_3N_4 membrane and opened a slit by using a focused ion beam (FIB). The membrane was coated after that with a metal layer followed by opening of a slit and CNTs were deposited on top of that. In 2002 Kociak et al. performed transport measurements *in situ* in a TEM chamber to obtain the chiral indices of the tubes [97]. Both of these measurements were lacking the gate and therefore the transport measurements were quite limited. However, Meyer et al. in 2004 [98] were combining successfully transport measurements including gate and TEM measurements. The trick was to normally fabricate the CNT device, do the transport measurements and after that cleave the chip in the vicinity of the transistor device. The fully transparent path for electrons is done by simply etching the chip in KOH. The schematic of the sample is presented in figure 3.4.

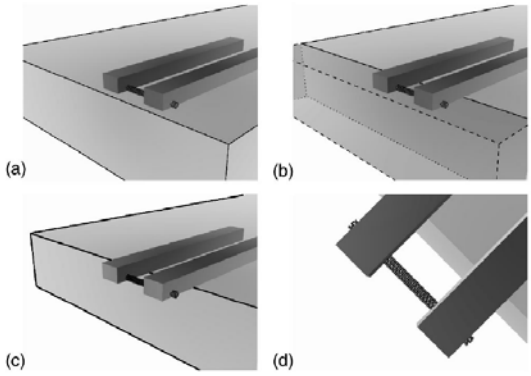

Figure 3.4: Principle of creating the free-standing structures. The substrate is cleaved close to the metallic contacts on a carbon nanotube (a). The substrate is etched in such a way that the structure is undercut from the side, removing the shaded volume in (b). This leaves the structure with the nanotube free-standing (c) so that the substrate is not in the line of sight of the TEM [(d), top view]. Adapted with permission from reference [98].

Later the same group performed also ED measurements on these type of samples [32] together with Raman measurements. Other groups have also managed to combine optical spectroscopy and ED measurements like Sfeir et al. [99] and Liu et al. [33, 100]. Sfeir et. al. fabricated relatively wide (20-120 µm) slits

through the substrate by using photolithography. The tubes were then grown across the slits giving the possibility to combine ED and optical spectroscopy (Rayleigh spectroscopy, in this case). Liu et al. used basically the same kind of process to fabricate the slits. After the tube growth they fabricated electrodes around 10 µm side from the slit so that they could do transport measurements on a different section of the tube compared to ED measurements [100].

The Hone group managed to combine TEM characterization with a novel transfer technique [101, 102]. They fabricated wide slits on Si/Si_3N_4 chip by first etching a normal membrane window and breaking it by ultrasonication. After that the tubes were grown across the slit. Now it is possible to do ED measurements to the tubes before transferring them onto the target chip. The target chip is then aligned and brought into contact with the slit chip. Then a droplet of resist is dropped from the backside of the slit to transfer the tube. Then it is easy to fabricate contact electrodes after dissolving the resist. This transfer procedure is shown in figure 3.5.

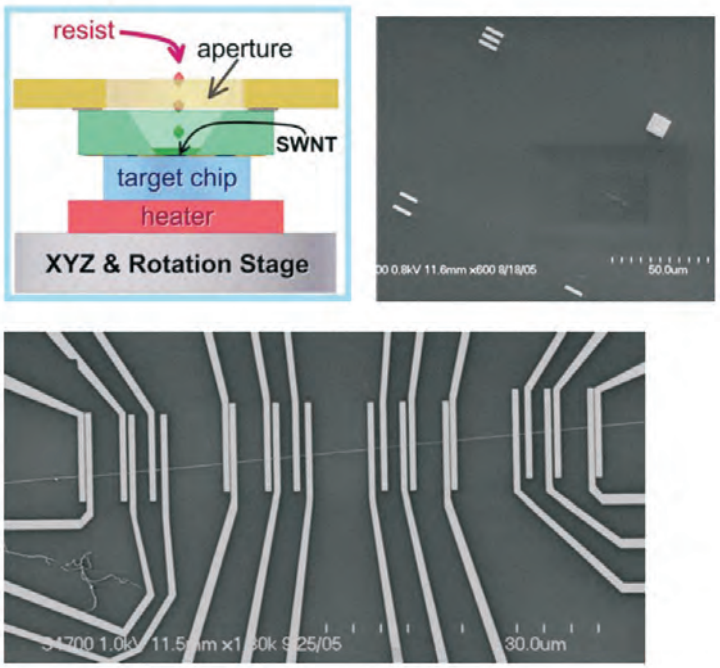

Figure 3.5: Nanotube transfer and device fabrication. Top left, setup for mechanical transfer of suspended nanotubes to target chip. Top right, transferred nanotube between alignment marks. Bottom, transferred nanotube with electrical leads defined by e-beam lithography. Adapted with permission from reference [102].

Kim et al. used silicon-on-isulator (SOI) wafer as a starting material [103] for combined transport and TEM measurements. They used deep RIE to etch a biq square to the backside of the chip. The oxide naturally acts as a stopping

layer then. Then they made another lithography round to etch the slits on the top side of the chip so that slits will be on the bigger square area. HF etching is needed to remove the oxide layer between the Si layers and furthermore additional lithography steps are needed to fabricate gate dielectric, gate and contact electrodes. Finally the tubes were grown on top of the contact electrodes.

3.2 Fabrication of the slit structures used in this work

The goal in suspended samples was to characterize fully the structure of the tube by using electron diffraction (ED) in TEM. Therefore the sample geometry was chosen to be like in figure 2.6 (e) in which the tube goes across narrow slits. This geometry allows the electron beam to pass freely through the sample. Such sample fabrication involves many micro- and nanofabrication steps involving e.g. plasma and wet etching techniques. The starting piece is a silicon chip. The chip is covered on both sides with a dielectric layer which can be used also as a masking material during sample processing. The idea is to fabricate a freestanding membrane window and then open a slit into it. The most widely used material is silicon nitride (Si_3N_4), since it has high mechanical strength and it is rather easy to fabricate low-stress films from it which is required for membranes.

The fabrication process for membranes contains e-beam lithography step with plasma etching followed by a wet etching step. The slit opening contains another lithography step with plasma etching and CNT deposition e.g. via CVD process (usually with lithographically defined catalyst areas). Adding electrical contacts and gate electrode to the device needs 1-2 additional lithography steps depending on the type of the gate.

Silicon nitride films

To coat a Si wafer, chemical vapor deposition is used. CVD is a general name of a process where reactive gas molecules, typically diluted with an inert carrier gas, reacts at a hot sample surface leading to a solid film growth. To form Si_3N_4 films, single crystal (100) silicon wafer is used as a starting material. The coating is done by using low pressure chemical vapor deposition (LPCVD) since that method provides low intrinsic stress to the film. Typically growth is done at $\approx 850°C$ and 500 mTorr pressure with 1:6 ratio of ammonia and SiH_2Cl_2 [104]. We have used LPCVD wafers purchased from Noel technologies.

Plasma etching

Plasma etching is used to etch Si_3N_4 films by using reactive gases. When the process is a combination of chemical and physical processes it is usually called

reactive ion etching (RIE). In those conditions the gas molecules are excited in RF-fields inside a vacuum chamber. The AC electromagnetic field rips off the electrons from the gas molecules creating plasma. The sample plate builds up negative voltage due to DC isolation from the rest of the chamber. The plasma itself is slightly more positively charged due the stripping of the electrons to the chamber walls and thus the positively charged ions in the plasma will collide with the sample plate. The ions then react chemically with the species on the sample surface, or they can also physically bombard i.e. sputter the material.

The anisotropy and selectivity of the process depends heavily on the reaction species. In the case of Si_3N_4, etching is done e.g. by using CHF_3 and oxygen (O_2). CHF_3 produces fluorine radicals that will etch the Si_3N_4 but the presence of carbon generates a passivation layer. Ion bombardment then removes the passivation layer from horizontal surfaces enhancing thus the anisotropy. Oxygen also increases the fluorine concentration enhancing the etch rate and selectivity. On the other hand, adding O_2 will increase also the etching rate of the resist mask. [104–106]

Wet etching

Wet etching is a process where liquid etchant reacts with solid forming soluble products. As in any etching, the process consists of transport of the reactants to the surface, surface reaction and transport of products from the surface. Silicon is typically etched using alkalines and potassium hydroxide (KOH) is the most universal etchant for that. KOH etching of Si lean on a base-reaction and the gross reaction is [107]

$$Si + 2H_2O + 2OH^- \rightarrow Si(OH)_2O_2^{--} + 2H_2. \tag{3.1}$$

The etching profile of Si is anisotropic and it is based on aligning the structures with the crystal planes of the wafer. The starting material in our case is (100) Si and the stopping layers are slow etching (111) planes and, of course, the Si_3N_4 layer. The selectivity between (100) and (111) directions is around 200:1. The angle between the (100) and (111) planes is 54.7° and therefore the end result is an inverted pyramide cut at its apex. This has to be taken into account when designing sizes of membranes by the following relation:

$$L = \frac{2d}{\tan 54.7} + l, \tag{3.2}$$

where L is the length of the square side in backside, d the thickness of the silicon and l the length of the square (window) side in topside. For example in order to have a 100 µm × 100 µm window, one has to do 525 µm × 525 µm openings to the backside.

3.2.1 Fabrication of slit substrates

The first step is to fabricate the membrane window. That can be done either by using photo- or e-beam lithography and using Si_3N_4 as a mask. Standard film thicknesses in our experiments were either 200 nm or 300 nm but also as thin as 30 nm films were tested. We used mostly e-beam lithography, which is described here. Fabrication starts by covering the substrate with resists from both sides and exposing a square to the resist into one side. The other side is covered to protect the nitride film in RIE etching. Then Si_3N_4 is etched away using resist as a masking material (figures 3.6 (a) and (b)). The etching is done in RIE (Oxford Instruments Plasmalab80Plus) with the following parameters: temperature 30 °C, pressure 55 mTorr, power 100 W, 50 sccm gas flow of trifluoromethane (CHF_3) and 5 sccm of O_2. Such recipe should provide roughly 26nm/min etching rate. Since the plasma etches also PMMA resist, the resist layer thickness needs to be high enough. Typically for a 300 nm thick Si_3N_4 film, around 1 µm thick resist layer is needed. Last, the resist is removed and the chip is ready for wet etching.

The wet etching of Si is done in a heated water sink. The samples are put into a 34 % KOH solution and placed into a water sink and the water is heated to around 98°C. These conditions should provide an etching rate of around 150 $\mu m/h$. The etching process can be seen clearly since it is bubbling strongly. After the etching is finished the samples are washed several times in hot water. The membrane window is now ready as seen in figure 3.6 (c).

The fabrication of the slit structure starts with another lithography round. Now the optimization of resist thickness is even more crucial since it affects to the resolution of the exposure and hence the actual width of the slit. Usually two layers of PMMA A7 with 3000 rpm is used which forms a resist layer around 800 nm thick. The slits and alignment markers are exposed at the same time. The opening of the slits is done again in RIE (figure 3.6 (d)). The etching time is important to optimize since also a too long etching widens the structures and can even etch the whole resist mask away. On the other hand narrow structures are slower to etch. Typically around 1 µm wide structures are etched in 15 minutes for 300 nm thick Si_3N_4. We have tested several different widths for the slits and the narrowest structures achieved have been roughly 500 nanometers for 300 nm thick membranes. The typical width of the slit is 2-3 µm though, since a too narrow slit causes problems in optical spectroscopy such as noisy background signals. A SEM image of a fabricated slit structure is seen on figure 3.6 (e). Also circular hole structures have been tested mostly for trying to optimize results of spin deposited nanotubes.

As a final step before CNT deposition a global gate electrode is fabricated if aiming to perform transport measurements. That is done by evaporating metal layer on the back side of the chip. There are however several problems with it. Firstly, too thick layers tend to bend the edges of the slits due to the stress. A second problem concerns the high growth temperatures of the CVD process

if growing the tubes as a last step. Several different materials were tested and many of them failed. This issue will be discussed more in section 3.4.

3.2.2 Deposition of CNTs across the slits

Once the sample is ready, the tubes need to be deposited across the slits. The first experiments were done in regular 1 µm wide slit structures using traditional spin deposition method. However the yield was very low and practically no individual tubes were obtained. Either there was really dense network of tubes at the slit (see figure 3.7) or if using more dilute suspensions the tubes followed the edges of the slits without going across it. Dilute suspensions were tested also without spinning by just putting a droplet of the suspension on top of the sample and letting that dry. This method fouled the sample even more and left a thin film of residues containing CNTS into the slit.

One proposed solution was to make the slits narrower. A thicker membrane film has its limitations in resolution but thinner films enable also thinner resist layers improving the resolution. As thin as 30 nm thick layers were tested and indeed narrower slits were easier to fabricate. The drawback was that the films were very fragile and broke easily. Some samples of thicker films were processed using FIB (focused ion beam) milling. The milling was done at Aalto University in Professor Ilkka Tittonen's group. Slits as narrow as 100 nm wide were fabricated. The deposition on those samples was a little bit more successful but the limited number of samples and fairly low yield in CNT deposition was the reason to abandon this path also. These samples were not optimal for optical spectroscopy either since the laser spot was larger than the slit, which naturally induces a noisy background to the signal. An example of such a sample is shown in figure 3.8.

Another approach was to change the shape of the openings in the membrane. A hole matrix was developed and tested as seen in figure 3.9. The yield was a bit better but still not good enough. Some devices were fabricated but unfortunately they were not working for example due to leakage to the gate. Overall, same type of problems was present with both types of opening geometries (slit or circle). It seemed that there was a flow through the openings but during the spin deposition CNTs somehow favor to go either directly through the opening or land at the edges of the slit. Another big issue was that the CNT solution needed to be much cleaner compared to solutions used for normal substrate supported CNT samples. The liquid flow through the opening caused choking due to large dirt particles.

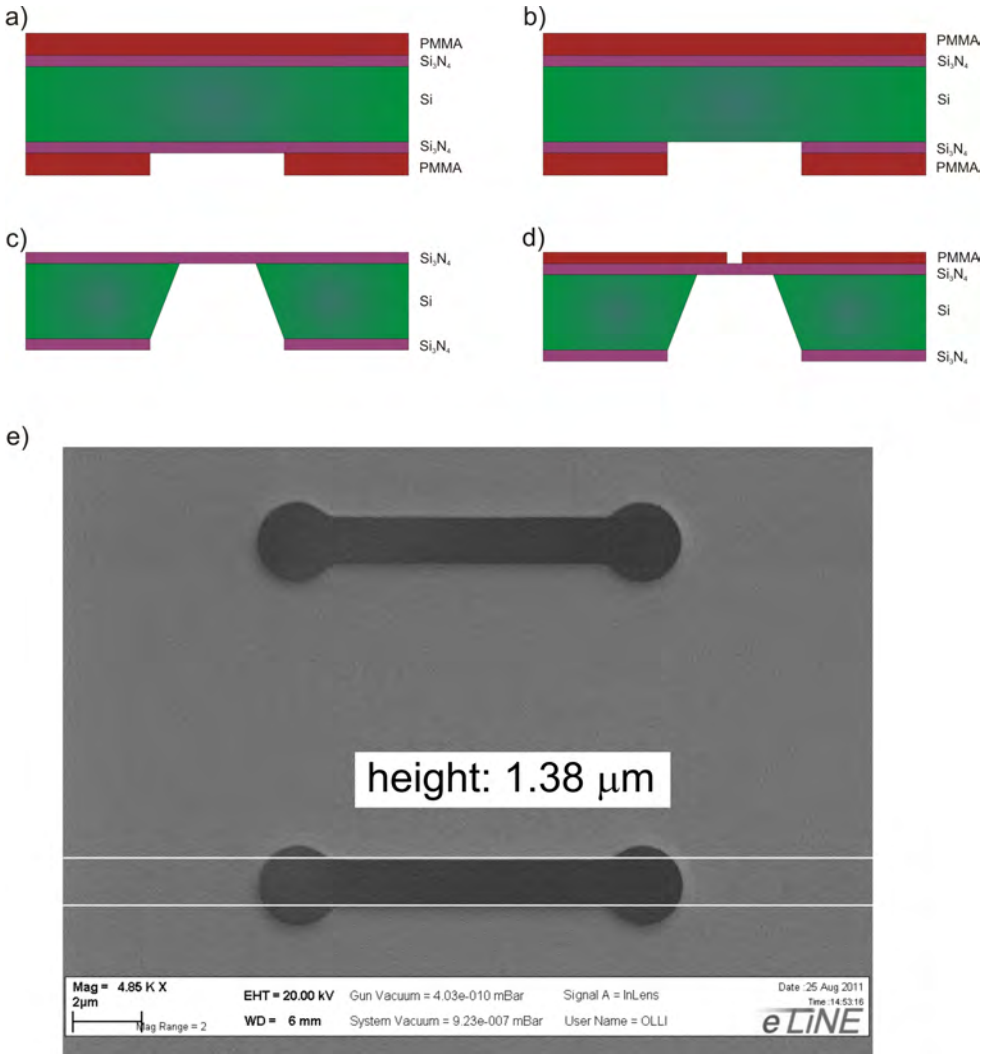

Figure 3.6: Fabrication of a slit into membrane window. (a) The sample is covered both sides with the resist and a square is patterned into other side of the chip. (b) Silicon nitride is etched away in RIE and resist washed away in acetone. (c) Anisotropic wet etching in KOH is performed to form freestanding membrane window. (e) Another e-beam patterning is done to fabricate an opening to the membrane window. (d) SEM image of a fabricated slit.

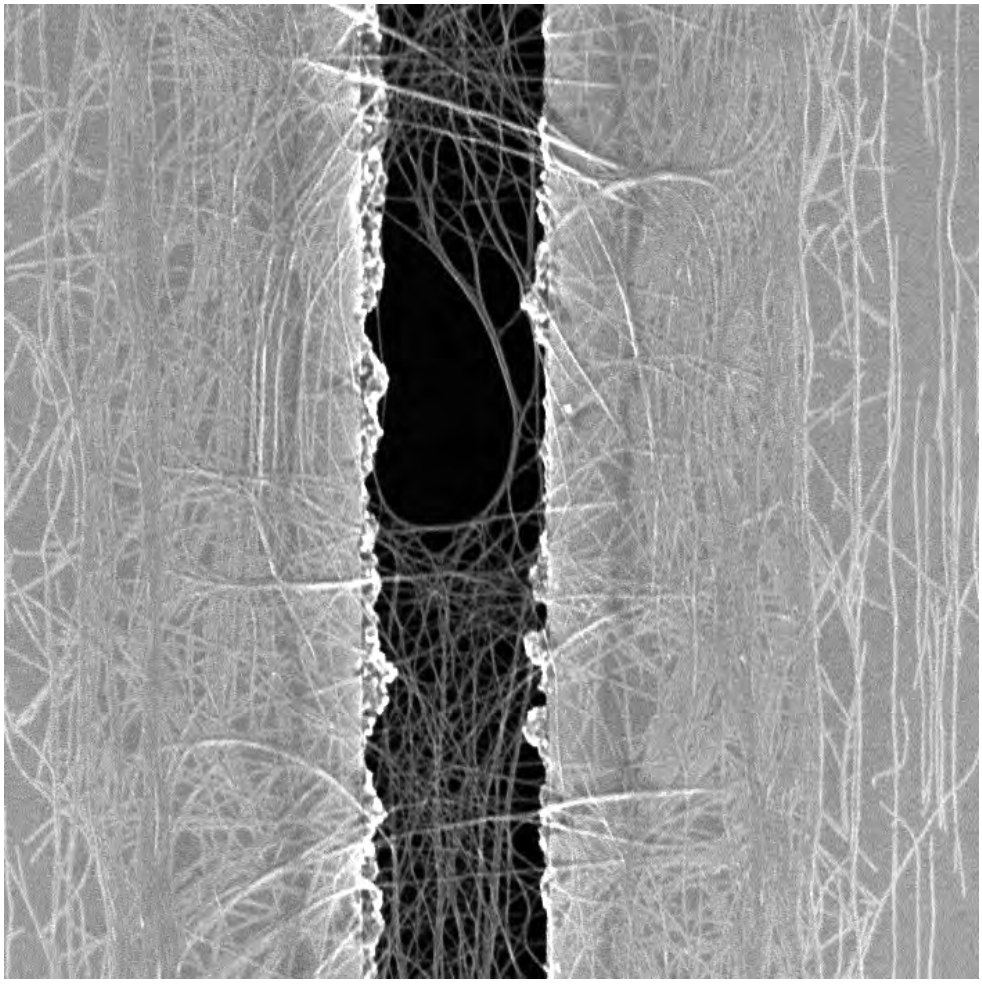

Figure 3.7: Carbon nanotubes from high concentration spin deposited onto slit sample. The tube density is high and only network is bridging the slit. Note that most of the tubes are aligned to the vertical direction at the slit edges. The image size is roughly 11 × 11 µm and width of the slit 2 µm.

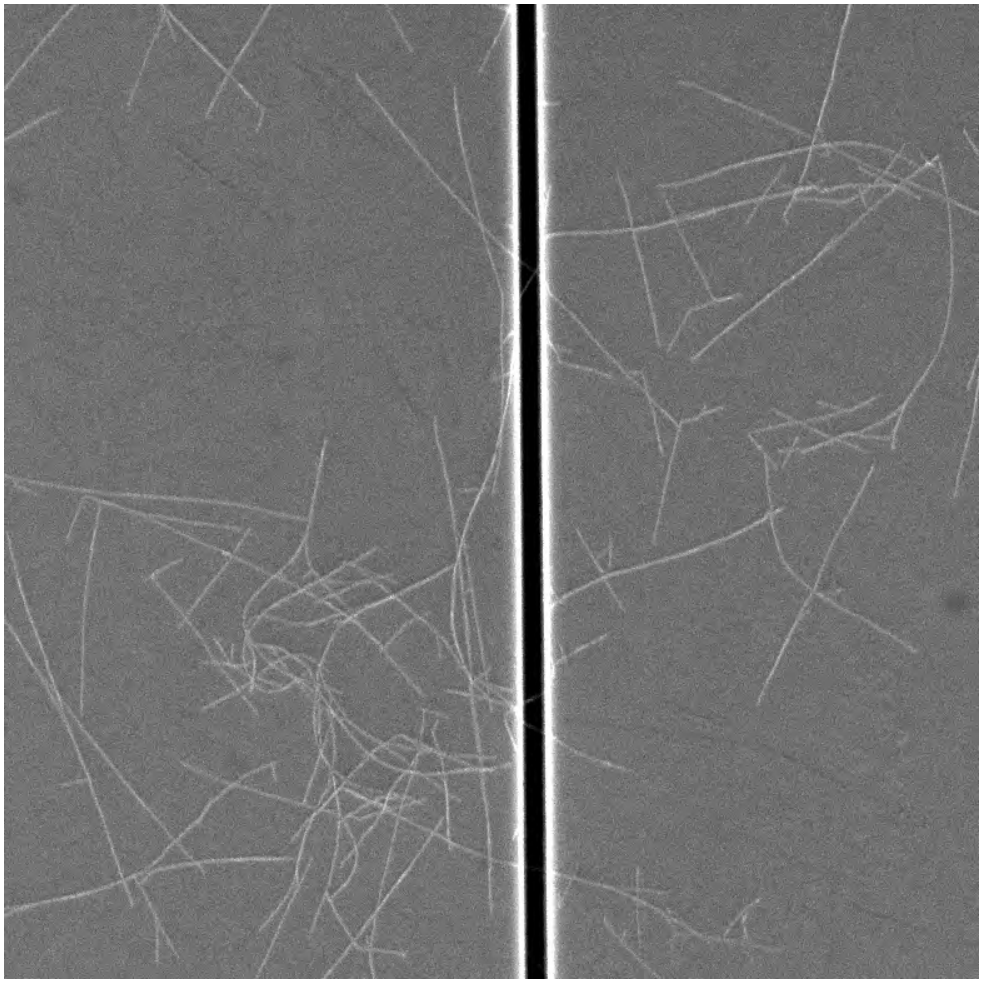

Figure 3.8: Around 100 nm wide slit fabricated by FIB. CNTs are spin deposited onto substrate and going across the slit. The image size is roughly 3.7×3.7 µm.

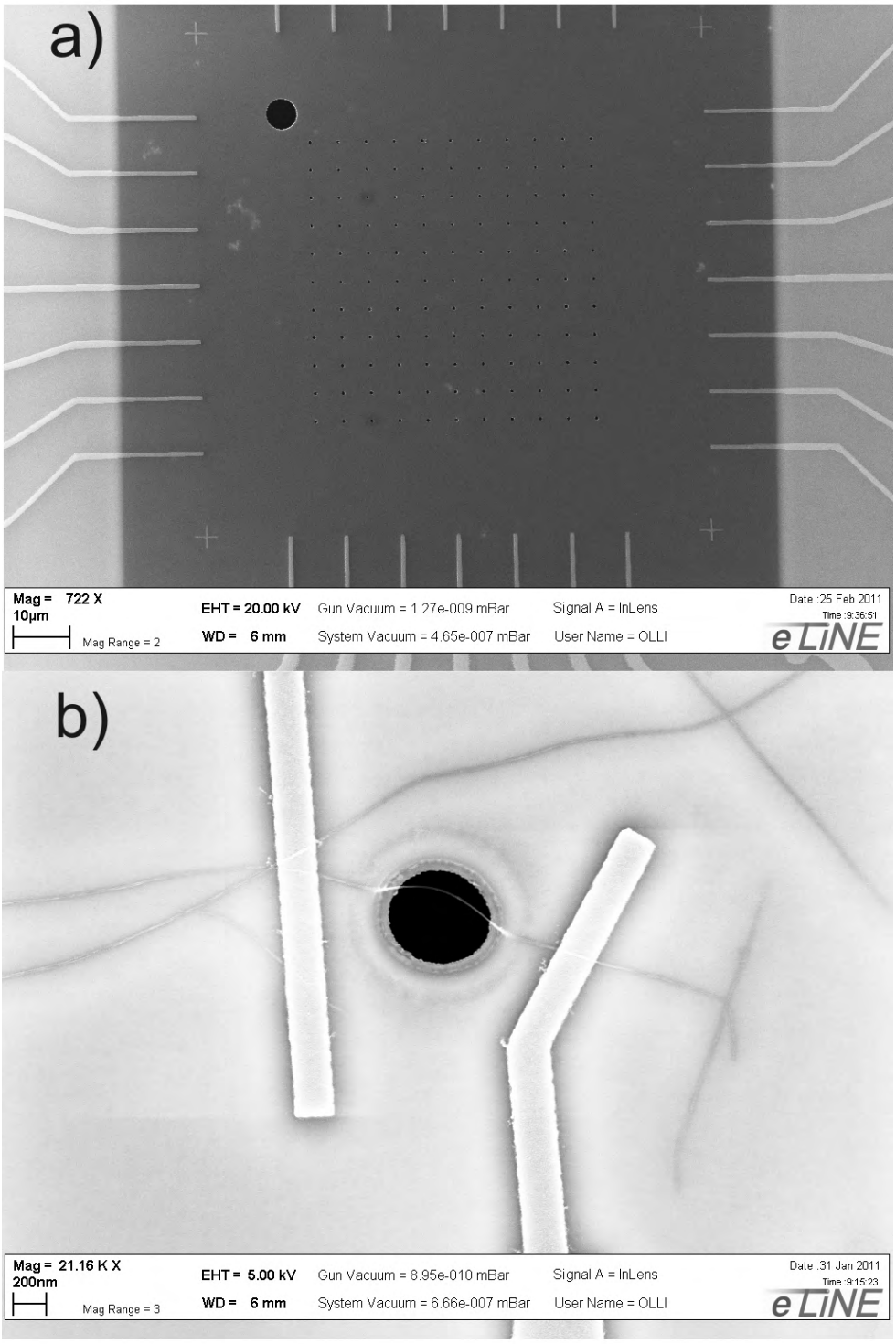

Figure 3.9: (a) An 11 ×11 hole matrix for spin deposition experiments. (b) Contacted nanotube device bridging over the hole. This device was not working and the yield of fabricated samples was fairly low.

DEP trapping

As another solution we tested dielectrophoretic trapping to get CNTs across the slit. That has been done earlier for CNTs as described in section 2.4.1 and there was lots of in-house experience of the method in trapping DNA origamis [108]. We fabricated electrode pairs at the opposite sides of the slit and did some DEP testing. The electrodes were connected and a droplet of CNT suspension was put on top of the sample. The frequency could be chosen between 300 kHz and 10 MHz and the peak to peak amplitude $V_{pp} = 1 - 5$ V. The main problem in the end was that the samples were too dirty for any measurements even though some trapping was noticed as seen in figure 3.10.

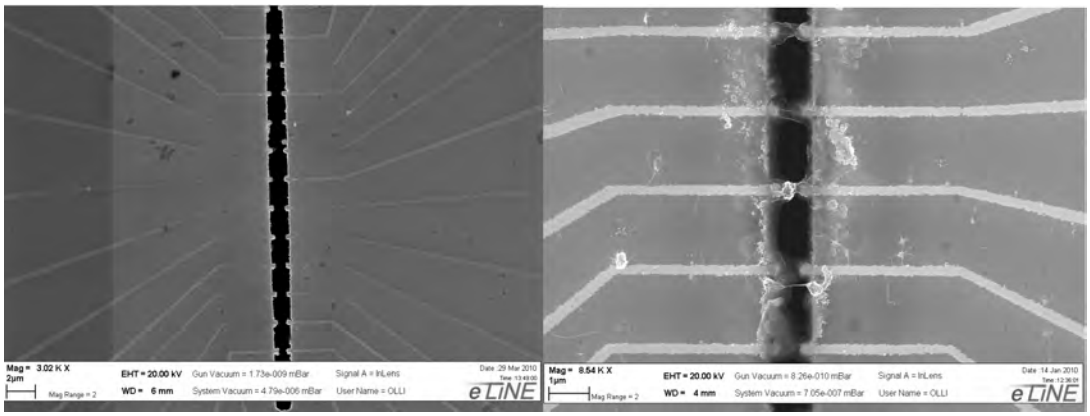

Figure 3.10: Sample for DEP experiments showing opposite electrode structure (left) and sample after trapping (right). Some tubes cross the slit but they are covered with foul film.

3.3 Nanotube synthesis via CVD method

Overall, the best alternative seems to be to grow the tubes directly across the slits by using the substrate CVD method. First the samples were sent to professor Esko Kauppinen's group to Otaniemi for growth and the details of the process is described in reference [76]. Since the catalyst was typically sputtered all over the sample, it was difficult to contact individual tubes even though these samples were suitable for optical spectroscopy. To speed up the processing and fabricate patterned catalyst areas, we built our own CVD setup based on ethanol vapor to grow aligned CNTs. This section describes first general background of CNT synthesis by using CVD method and then the detailed growth steps we have used.

3.3.1 Basic chemistry of CNT synthesis

Chemical vapor deposition (CVD) of CNTs is based on decomposition of a hydrocarbon vapor in the presence of a metal catalyst. It is nowadays the most widely used technique to synthesize SWNTs. The process needs hydrocarbon vapor passing the catalyst. The catalyst is typically in high temperature (600-1200) °C and the hydrocarbon vapor will flow through the catalyst area with inert carrier gas. The hydrocarbon vapor can be obtained from different precursor sources that can be either gas, liquid or solid. Likewise, many different catalysts have been used either on top of the substrate (substrate-CVD) or floating freely in the chamber. Usually the catalysts are metal nanoparticles. [109]

There are many different growth mechanisms in the process and the most general mechanism is described in this section. When hydrocarbon vapor encounter a metallic catalyst particle, it decomposes into carbon and hydrogen species. Hydrogen goes away and carbon dissolves into catalyst. When the carbon solubility limit at a given temperature is reached in the metal, it precipitates as-dissolved carbon out and crystallizes into a cylindrical network. This network has no dangling bonds and is hence energetically stable. A thermal gradient inside the metal due to hydrocarbon decomposition (releases heat to the metal) and carbon crystallization (absorbs heat from the metal) keeps the process going on. In substrate-CVD there are two growth mechanisms depending on the interaction strength between the metal catalyst particle and the substrate. If the interaction is weak (sharp contact angle) decomposition happens on top of the metal, carbon diffuses down through the metal and the nanotube precipitates out from the metal bottom pushing the metal catalyst particle off from the surface of the substrate. The growth continues as long as the top of the catalyst particle is open and thus active for hydrocarbon decomposition. This case is called tip-growth model. The other case is called base-growth model and then the interaction between substrate and metal is strong (obtuse angle). Now carbon precipitates out from the apex of the metal and hydrocarbon decomposition happens on the lower peripheral surface. So CNTs grow up and the catalyst

stays on its place. These two mechanisms are depicted in figure 3.11. [109]

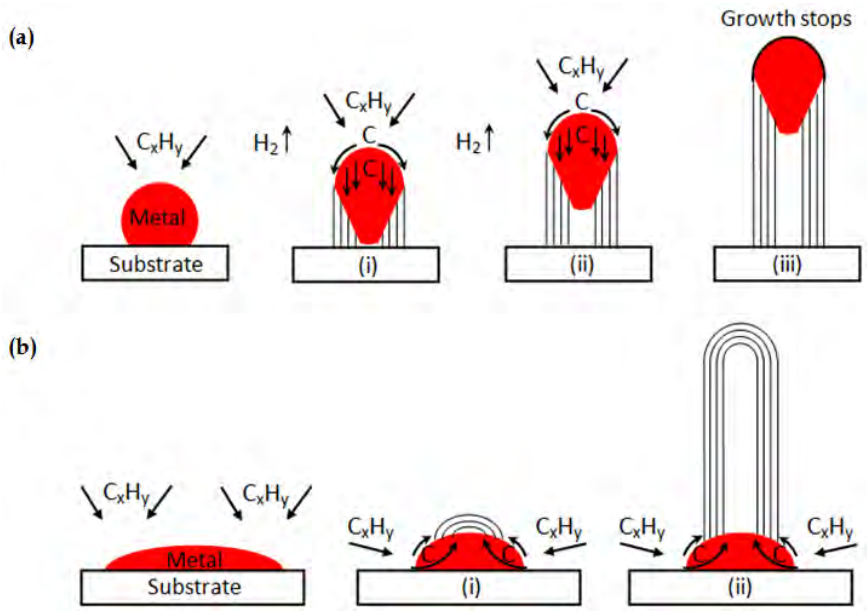

Figure 3.11: Growth mechanisms for carbon nanotubes. (a) Hydrocarbon decomposes on top of catalyst, carbon diffuses through catalyst and nanotube crystallizes lifting catalyst up. (b) Hydrocarbon decomposes close to substrate at the edges and carbon diffuses toward apex where it crystallizes out. Adapted with permission from reference [110].

3.3.2 Alcohol-CVD

Ethanol based CVD method has been used successfully to grow ultalong, oriented CNTs by many different groups and both the instrumentation and chemicals are rather simple, cheap and safe. Alcohol-based recipes are also reported to synthesize high quality tubes free of amorphous carbon. The idea of this method is to introduce alcohol as a carbon source. Maruyama et al. [111] proposed that OH radical will efficiently remove amorphous carbon and that the reaction of OH radical to solid carbon will prevent formation of soot. OH radical is decomposed on the catalyst surface from the alcohol molecule and will attack nearby carbon atoms etching amorphous carbon. Usually a mixture of Argon and hydrogen is used as a carrier gas since hydrogen reduce metal catalyst nanoparticles faster but needs higher growth temperatures to reduce the amount of amorphous carbon [112].

The process for long and aligned tubes needs constant laminar flow through the tube. One of the first ethanol-based CNT growth report by Zhu's group, claimed that the CNTs grow mostly with tip-growth model [113] and the limiting factor to the length is the size of the chip (if other parameters favor long

growth). Afterwards also base-growth model is proposed to form long, oriented tubes [114] even though the tip-growth model is the majority in long tubes [115]. Kong's group also claimed that the crucial factor in growing long CNTs is the nanoparticle's catalytic lifetime and that the alignment with the gas flow happens only after the CNTs reach critical length [114]. They studied these effects with ethanol-CVD and methane-CVD using two different catalysts (ferritin and $FeCl_3$) and different pretreatment steps for the catalyst. The issue of long, aligned tubes has been studied lot in the past decade and several mechanisms have been proposed to affect the results. In general, there is always both short, randomly oriented CNTs and long, oriented ones present. Wei group [116] concluded based on previous literature and their own experiments that the tubes can follow the gas flow after they are approximately 20µm long. There were several reasons discussed about the short nanotube formation. First, short tubes quite often grow in base-growth mechanism. One important issue for that is the agglomeration of catalyst particles in high temperature. This will lead to bigger catalyst particles and hence to MWNTs which grow mostly on base-growth mechanism. Same agglomeration causes also entanglement of short tubes (even if they are thin) before reaching the critical length terminating the growth. Last, falling down of growing tip of floating CNTs causes also growth termination. Possible reasons for that include reasons such as temperature stability, catalyst lifetime or deactivation, gas flow disturbances etc. Therefore, the yield of long, oriented CNTs is always fairly low compared to short ones. Overall, the optimal growth conditions can be sometimes challenging to achieve, since so many different parameters contribute on that.

3.3.3 CNT synthesis results in this work

The first growth experiments were done by following Zhu's group [113] growth recipe and Burke's group catalyst preparation [117] procedure. The hydrocarbon source was ethanol and carrier gas a mixture of Ar/H_2 (6 % of hydrogen). The catalyst material at the beginning was $FeCl_3$ which was then mixed in PMMA A4 solution (10 mM concentration). The catalyst was spin deposited on the sample and e-beam lithography step was done to pattern catalyst areas. Very large overdose causes the polymers to crosslink even stronger resulting positive exposure. The lift off was originally relatively difficult, so later an extra layer of pure PMMA was deposited underneath the catalyst-PMMA layer to ease the lift off. The CVD setup consisted of tube furnace (6 cm ceramic tube element) and load lock system with a ball valve separating the load chamber from the actual furnace (see figure 3.12). With such system it is possible to load and unload samples while the furnace is on and hot saving time. The samples are loaded in through the load lock in Ar flow and placed into 700 °C temperature zone to burn out the resist. The calcination step was done in constant O_2 flow for 10 minutes. The flow was changed back to Ar and the sample was brought to growth temperature zone and finally changed to AR/H_2 (6 % of H_2) flow for

growth. The growth was done at 920 °C and carrier gas was bubbled through ice chilled ethanol to get the alcohol into the furnace. The actual growth step was done in 1.5 l/min (1500 sccm) flow rate for 30 minutes. After that the samples were unloaded in Ar flow.

Figure 3.12: CVD system at NSC lab. Tube furnace with 1 m long and 4 cm wide tube element and the load lock system attached on it (On the right). Gas flow meters are seen on the left corner and alcohol bubbler placed in the heat sink of Peltier plate is visible next to those.

Already the first experiments were successful and long tubes were obtained to bridge over $\sim$ 60 µm wide trench in the substrate as seen in figure 3.13. In that case the sample had 20 nm thick palladium (Pd) electrodes which served as a catalyst also. Soon it became clear, however, that even though good quality tubes were obtained they were not usually that long and straight but mostly short and random-oriented. As described earlier there are many different parameters that affect to the yield. In gas-flow directed growth one of the key parameters is to achieve laminar flow in the growth zone [118]. Since our flow rate was relative high compared to literature (e.g. 20 sccm in ref. [113]) the first aid was to decrease the flow rate. Our flow meter in that setup managed reliable flow rates of roughly 200 sccm but we didn't notice any difference in the growth result. Generally, the flow conditions are described using Reynolds number:

$$R_e = \frac{\rho v d}{\gamma}, \tag{3.3}$$

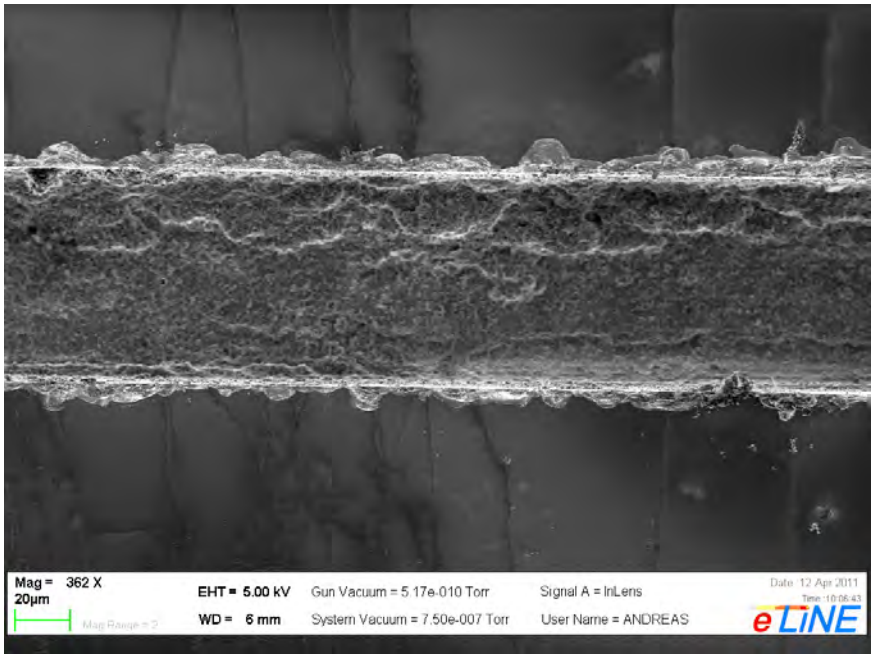

Figure 3.13: First growth experiments revealing long CNTs bridging over $\sim$ 60 µm trench.

where ρ is the density of the gas, v the speed of the gas, d diameter of the tube element and γ viscosity of the gas. Reynolds number can be estimated with a relative straightforward calculation and is on the order of 20. In these conditions the flow should be already laminar so that should not be the limiting factor even though lower flow rate was used later followed by other articles. On the other hand too low flow rates are reported to cause skidding on the substrate [113] which can also terminate the growth too early. We tried to optimize the flow also more laminar by adjusting the flow speed and putting the sample into smaller tube which was then brought into the growth zone [119]. Since our flow conditions should be already laminar, no big differences was expected and seen. But small and short quartz tube serves as a good sample stage that doesn't contaminate the furnace and it is compatible to our loadlock system. We also have tested several different sample stages made from e.g. Inconel, Cu and ceramic materials but they all had some issues of contamination.

After the first tests that showed rather good quality but usually short tubes, a new dedicated system for CNT growth was purchased. The main difference is that the new setup has 4 cm quartz tube element and vacuum pumping line connected to setup. Otherwise the system is the same than the previous. Also the catalyst preparation was changed mainly due to the problems of lift off in resist-mixed resist. Therefore an alternative recipe based on evaporated ultra-thin films was used. The idea is to pattern the catalyst areas and then evaporate

very thin film of suitable metal. We used either cobalt or iron and followed reference [120] to obtain similar growth conditions. The results were usually pretty much the same regardless the catalyst material and only occasionally really long tubes were obtained. Typical growth result for Co film is seen in figure 3.14. On the other hand, such films are easy to fabricate simultaneously into several samples.

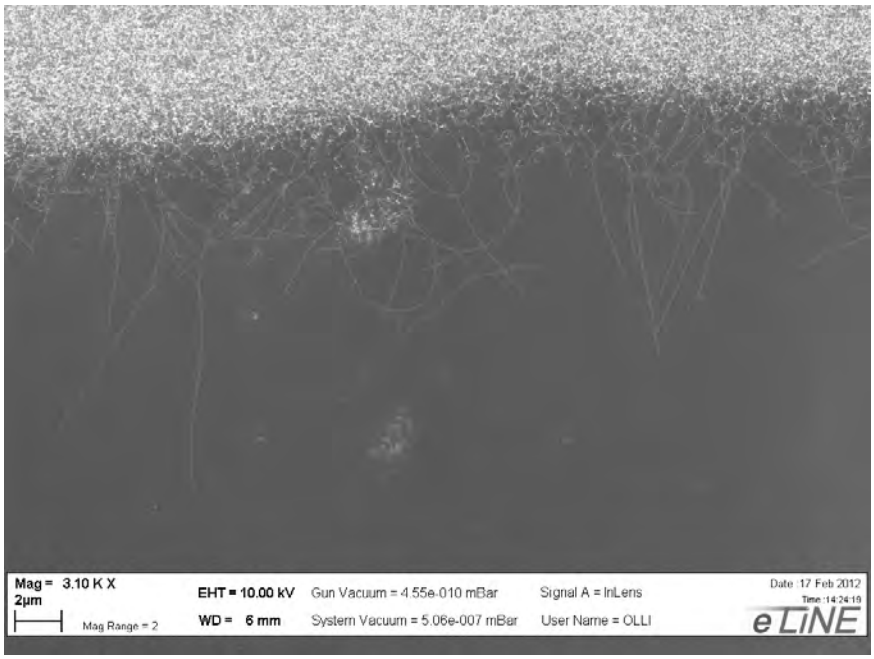

Figure 3.14: Typical growth result of thin Co catalyst layer taken in SEM. The longest tubes are around 10 µm long.

The most widely used method to grow tubes became established from Fe thin film as catalyst with following conditions: reduction step in ∼500 sccm Ar/H_2 flow for 20 minutes, growth step in ∼200 sccmAr/H_2 flow bubbled through 0 °C ethanol for 20 minutes with a growth temperature of 850 °C. That gives good quality tubes with long tubes bridging the slit. We have also tested the effect of different temperatures between 800–920 °C with negligible effect on results, especially on length. The yield of long tubes bridging over slit and reaching far enough on top of the membrane was usually fairly low and that needs to be developed still in the future.

3.4 Attempts to fabricate electrical contacts on suspended tubes

Even though the yield of observing good single nanotubes bridging across slit was fairly low, tubes were still contacted and measurements attempted already on spin deposited tubes as seen in figure 3.9 (b). As mentioned earlier, the yield enhanced substantially when moving to CVD grown samples but still several problems were encountered.

The electrical contacts have been done mainly by using top contacts i.e. the electrodes are evaporated on top of the CNT. A gate electrode is also needed to perform comprehensive transport measurements. One big issue in the fabrication yield is the PMMA deposition when patterning contacts. Since the tubes are hanging freely, they are really sensitive and spinning the resist can break the tube. Our setup is even more sensitive than in the case of a tube going across a trench since there is a flow of resist through the opening. However, some nice samples could be made but there were some other issues then making the samples unworkable.

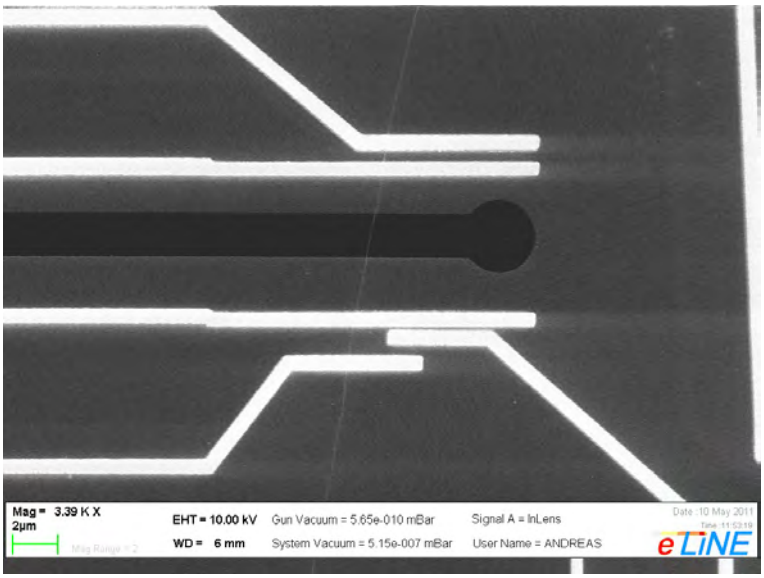

Figure 3.15: A SEM image of a suspended CNT device with a side gate (section underneath the slit).

A major problem was the leakage between the source or drain and gate electrode through the Si_3N_4 dielectric. The gate was originally done by evaporating a thin (few tens of nanometers) metal layer on the back side of the chip. It seemed that the RIE etching of the openings induced pinholes. These pinholes could be avoided when protecting the back side of the chip with the resist layer and by cleaning the front side of the chip carefully. However, we started to do

side gate structures when trying to fabricate suspended FET instead of making a global back gate since it saves one processing step and saves time before all issues would be solved. A SEM image of a nice suspended CNT with a side gate is shown in figure 3.15. The tube is CVD grown but this device, as many others, didn't work while trying to measure it. Examining the tubes afterwards revealed that there were blown sections in the tubes. This was possibly due to some charging effects affecting the tubes. However, a few working samples without gate electrode were fabricated and figure 3.16 shows an I-V curve of such a tube. To enhance the yield alternative options are tested in the future. The first one is already quite a standard process when contacting suspended tubes relying on bottom contacts i.e. the contact metal is deposited first and the nanotubes are grown after that contacting source and drain electrodes. The other option is more sophisticated and should provide really clean contacts. There the tube is connected using a physical mask that is aligned very precisely on top of the target chip containing the tube. This mask could be done from a similar kind of Si_3N_4/Si chip with bigger membrane window.

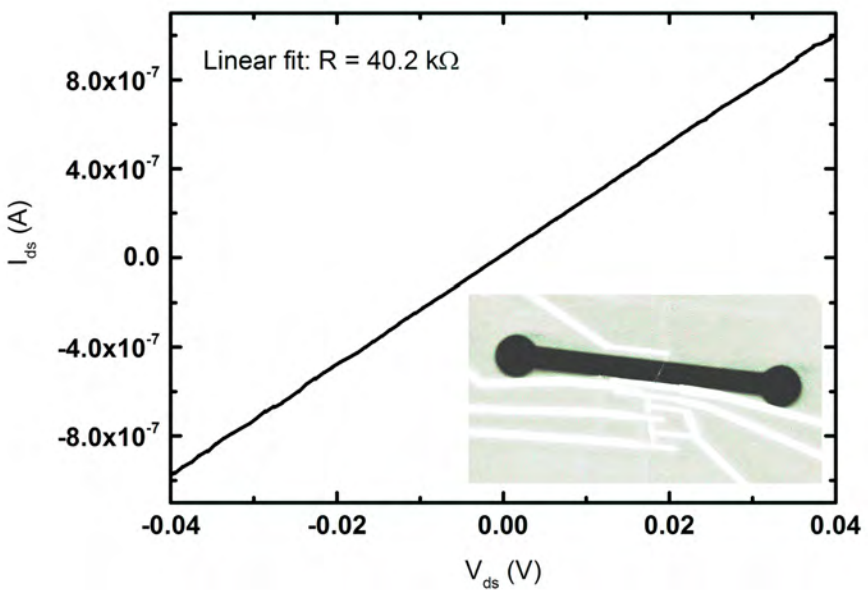

Figure 3.16: An IV curve of a suspended CNT device at room temperature. The tube resistance is 40.2 kΩ.

Chapter 4

Electron diffraction and optical measurements on suspended CNT structures

This chapter describes the measurements that have been performed on the suspended tubes. First, the background of electron diffraction is described and the experimental diffraction pattern with index assignment from our suspended tubes is presented. The second section describes nonlinear optics and presents the results we have obtained from nonlinear spectroscopy measurements.

4.1 Electron diffraction

With electron diffraction (ED) one can study crystallographic properties of specimen. Electron diffraction relies on information of the spatial distribution of scattered electrons and it arises from the wave nature of electrons.

4.1.1 Crystal structure

A lattice is an infinite array of points in 3D space which looks identical from each lattice points. Furthermore every lattice point have the translational periodicity so the lattice can be defined as three primitive vectors spanning translation vector connecting two lattice points [121]:

$$\vec{R} = u\vec{a} + v\vec{b} + w\vec{c}, \tag{4.1}$$

where u, v and w are integers. Equivalent representation of crystal structure can be made by the use of crystal planes using notation of Miller indices (hkl). Crystal planes can be described by using a vector normal to the planes $\hat{n}_{hkl}$ and interplanar spacing d of two similar planes. Since this representation is rather complicated, one can define the vector

$$\vec{G}_{hkl} = \frac{2\pi\hat{n}_{hkl}}{d}, \tag{4.2}$$

which will define the reciprocal lattice and have the dimension of inverse length each index denoting a plane orthogonal to a basis of reciprocal lattice vectors. The vector is thus equivalently described as $\vec{G}_{hkl} = h\vec{a}^* + k\vec{b}^* + l\vec{c}^*$, where $\vec{a}^*$, $\vec{b}^*$ and $\vec{c}^*$ are reciprocal lattice vectors. So every crystal thus has both a real space lattice and a reciprocal lattice and furthermore each point in reciprocal space corresponds to a family of planes in real space and vice versa.

4.1.2 Bragg's diffraction

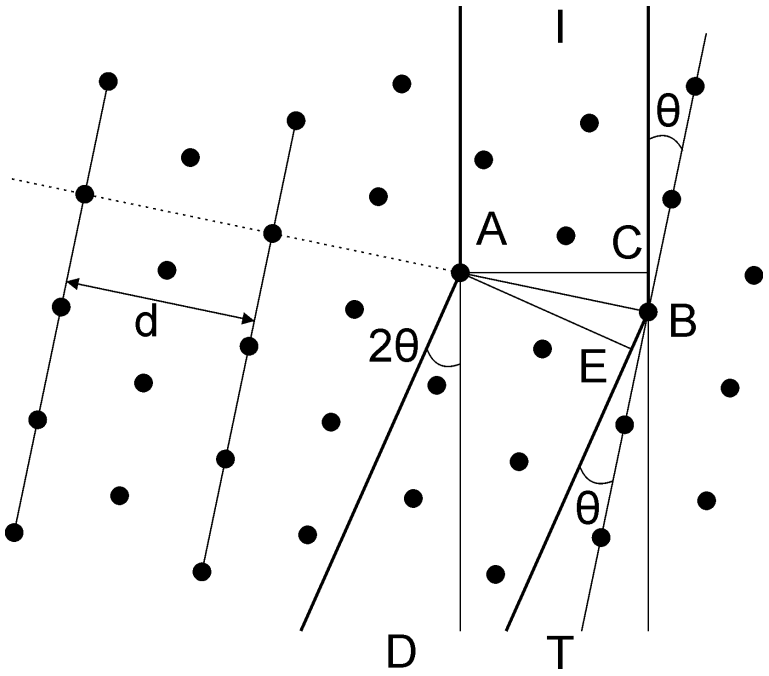

Figure 4.1: The scattering of an incident beam of electrons (I) by a crystalline specimen. Intense beams of electrons may emerge from the other side of the specimen undeviated (T) or having diffracted (D) from atomic planes of spacing d. In other directions no intense beams will be formed. Adapted from reference [122].

Let us first consider the lattice of a 3D crystal as in figure 4.1. The incident electron beam (I) is scattered from the lattice at points A and B. The scattered beam at D will be in phase (constructive interference) if the phase shift is $2\pi m$, (m is integer number) and thus the path lengths differ by an integer number of λ (in fig. 4.1 CB + BE = $n\lambda$). This will lead then to Bragg's law:

$$2d \sin\theta = n\lambda, \tag{4.3}$$

where d is the interplanar spacing, θ the angle between incident beam and lattice

plane and n integer number. In other words, there are only few elastically scattered electrons that have different angle than θ. [122]

In practice, there are always different lattice planes with different interplanar spacing and density of atoms. Therefore also the intensity of diffraction is different. The scattering amplitude can be expressed by using the structure factor

$$F(\vec{G}) = \int V(\vec{R}) e^{2\pi i \vec{G} \cdot \vec{R}} d\vec{R}, \tag{4.4}$$

where $V(\vec{R}) = ((2\pi m_e e)/h^2) U(\vec{R})$ is the modified scattering potential, $U(\vec{R})$ the coulombic potential of the scatterer, m_e relativistic mass of the electron and e elementary charge. The diffraction intensity distribution is simply $I(\vec{G}) = |F(\vec{G})|^2$ [123].

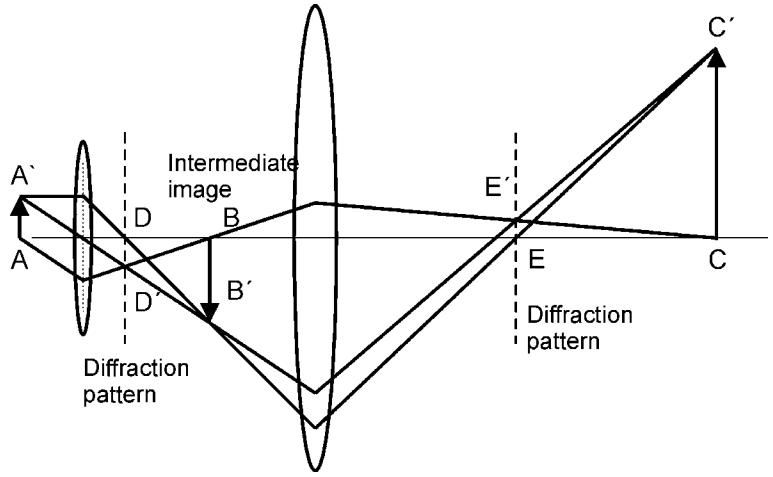

Figure 4.2: The ray diagram of a two-stage projection microscope showing the positions of the diffraction pattern (DD and EE) and image (BB and CC‘). Adapted from reference [122].

The electron diffraction experiments are done mostly by using a transmission electron microscope with very short wavelengths (High electron energy) compared to typical distances of lattice planes. Therefore $\sin\theta \approx \theta$ and equation (4.3) simplifies to $\lambda = 2d\theta$. Furthermore, it means that strong diffraction occurs only from the planes that are almost parallel to the electron beam. The diffraction pattern formation can be understood by studying the optics of such device. The ray diagram of the two stage projection lenses reveals the position of diffraction pattern and image as in figure 4.2. The rays that are parallel to each other will coincide at diffraction plane DD' and following them through the second projector lens at plane EE'. The image is then formed at BB' and CC'. Thus By using simple geometry, one can show that the spacing of lattice planes d can be easily determined from the pattern by simply measuring the distance between the spot of unscattered beam and scattered beam. A single

crystal sample generates a regular array of spots as for a multicrystal sample the structure is more complicated since more planes can diffract. But still the possible lattice spacing's d are limited (and therefore, the spacing of the spots r) and the generated pattern on spots are not randomly distributed but fall on rings. If the grain size of a different crystal is even smaller the pattern eventually is a continuous ring because the individual spots are so close to each other's. [122]

4.1.3 Laue formulation of diffraction

Let's consider again diffraction of the incident electron beam from the lattice. The beams can be represented as a plane waves $e^{i\vec{k}\cdot\vec{r}}$ and $e^{i\vec{k'}\cdot\vec{r}}$, where $\vec{k}$ is the wave vector of incident beam and $\vec{k'}$ wave vector of diffracted beam, respectively. Then the change in the wave vector can be described as $\Delta\vec{K} = \vec{k'} - \vec{k}$ and is defined as scattering vector (see figure 4.3). Note that the constructive interfer-

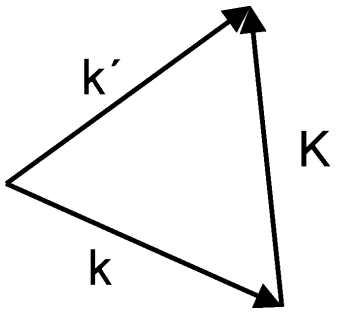

Figure 4.3: Definition of the scattering vector.

ence occurs when the phase shift between incident and diffracted beams are $2\pi n$ and thus $e^{i\vec{K}\cdot\vec{R}} = 1$ ($\vec{K}\cdot\vec{R} = 2\pi n$), where $\vec{R}$ is the translational vector of real lattice. The abovementioned condition can occur only when scattering vector $\vec{K}$ is equal to the reciprocal lattice vector $\vec{G}$. This leads to the Laue condition [121]

$$\vec{K} = \vec{G}. \tag{4.5}$$

The reciprocal lattice is very useful in diffraction analysis since reciprocal lattice points can be constructed from real space lattice planes. So in principle the diffraction pattern can be constructed from any known crystal. This can be seen from the Ewald sphere construction (figure 4.4). First, the diffracting crystal is represented by its reciprocal lattice. The wave vector $\vec{k}$ of the incident beam is drawn such that it will terminate at a reciprocal lattice point. Then a sphere of radius $|\vec{k}| = 2\pi/\lambda$ is drawn about the origin of $\vec{k}$. Now the diffracted beam exists only if the sphere intersects any other reciprocal lattice points. Only then $\vec{k'} = \vec{k} + \vec{G}$ and the Laue condition is fulfilled.

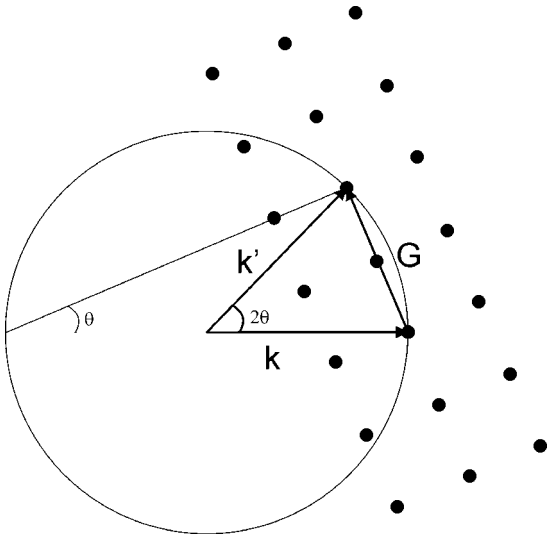

Figure 4.4: Ewald sphere construction.

4.1.4 Electron diffraction from carbon nanotubes

The first electron diffraction patterns of CNTs were taken in the famous pioneering paper on nanotubes by Iijima in 1991 [2] since the whole characterization was done with TEM. After that many detailed ED studies have been performed (see e.g. [124, 125].

Understanding of diffraction pattern of carbon nanotubes needs kinematical diffraction theory. As mentioned earlier the electron scattering amplitude can be expressed by using the structure factor $F(\vec{G})$. First we need to examine the scattering potential and structure factor of a helix as illustrated in figure 4.5. In nanotubes the situation is more complicated since there are many atomic helices and the structure factor is thus more complicated. The diffraction pattern of CNTs is different compared to graphene and the spots are elongated to the axial direction of the tube due to the curvature and small diameter of the tubes. The details of the formation of diffraction patterns in CNTs are e.g. given in reference [123].

Two main branches are developed in the structure determination of CNTs. The other method relies on chiral angle determination using correction factor [124] as the other one relies on the ratio of layer lines [125]. Analyzing the diffraction patterns in our samples relies on the method described in reference [126] which is based on layer line analysis. Briefly, the indices of a nanotube can be determined by calculating the spacing's of layer lines d_i (see figure 4.6) from the equatorial line. The layer line spacing's can be expressed as a function of the chiral indices (n, m) and thus it is possible to assign the indices by solving simultaneously any two expressions for layer-lines d_i. The benefit of this method is that the tilt angle of the CNTs are evaluated and hence automatically

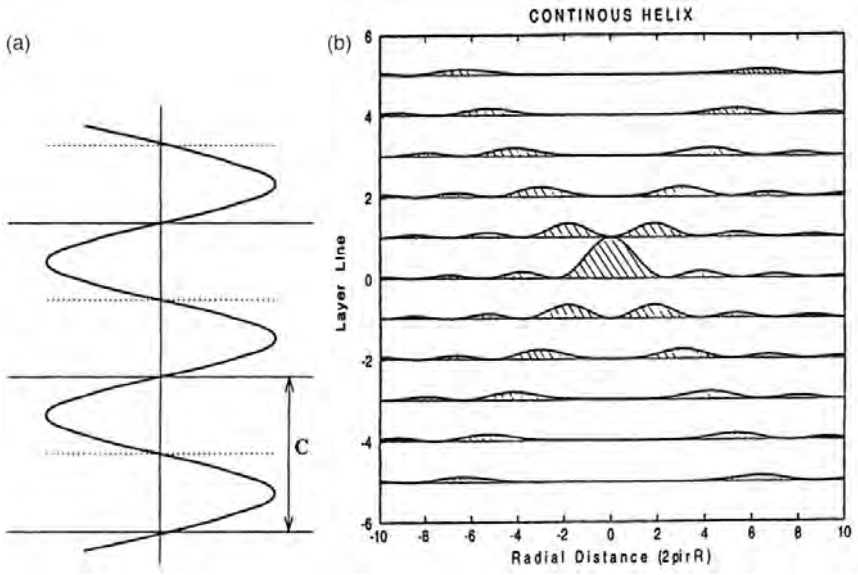

Figure 4.5: (a) Schematic of a continuous helix of pitch length C. The scattering potential in polar coordinates is $V(r, \phi, z) = V_0\delta(r - r_0)\delta\left(\frac{2\pi z}{C} - \phi\right)$ (b) Corresponding electron diffraction pattern of the continuous helix. It consist of a set of layer lines separated by 1/C and the intensity on layer line l is proportional to $|J_l(X)|^2$, where J_l is the lth order Bessel function. Adapted with permission from reference [123].

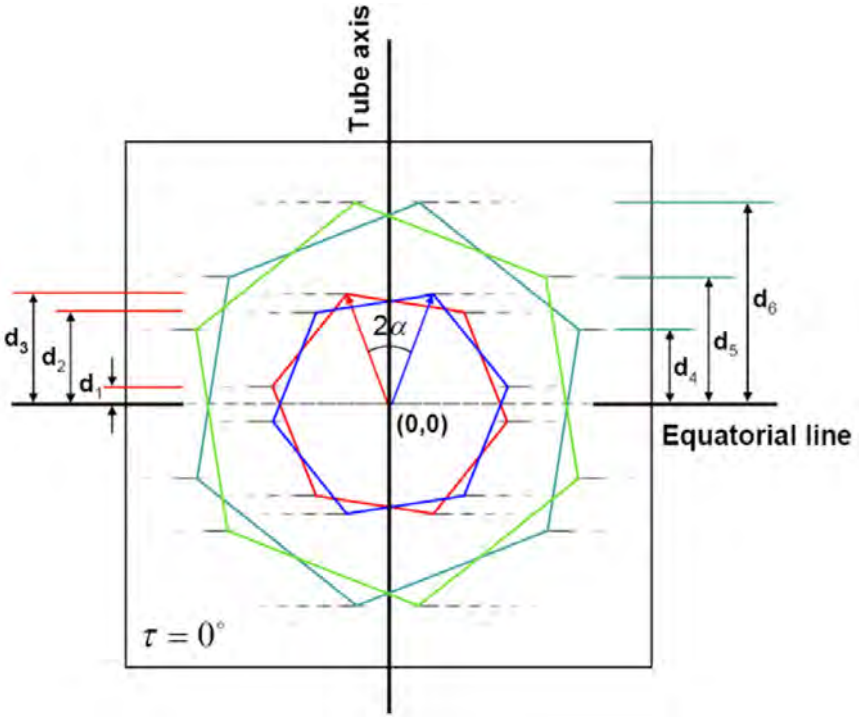

Figure 4.6: A simulated electron diffraction pattern from a $(12, 7)$ SWNT in normal incidence ($\tau = 0°$); discrete hexagons are constructed from layer lines as schematically illustrated. Layer line spacing's are specified by d_i. α is the chiral angle of the nanotube. Adapted with permission from reference [126].

compensated in index determination. The diffraction studies were performed in Aalto University at Professor Esko Kauppinen's group. Two different TEM setups have been used: Philips CM200-FEG TEM system and JEOL JEM-2200FS Cs-corrected high resolution TEM system. In addition, a separate TEM holder for our slit samples was designed and fabricated. The accelerating voltage was 80 kV and short exposure times of 3 s was used to avoid the possible damage of the tubes caused by the electrons. Examples of electron diffraction patterns with index assignment from our tubes are given in figure 4.7.

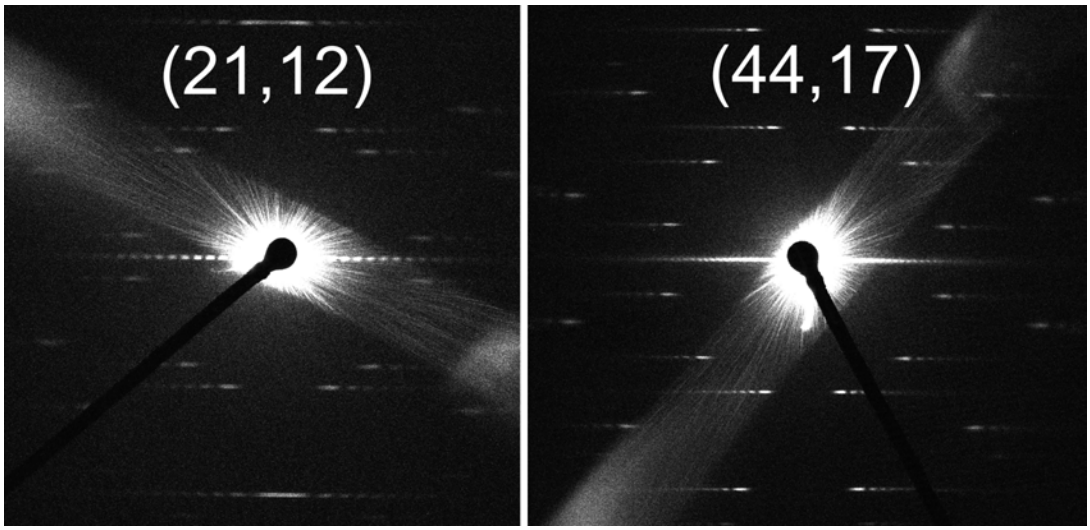

Figure 4.7: Experimental diffraction pattern from $(21, 12)$ tube (left) and $(44, 17)$ tube (right). The index assignment is done by Dr. Hua Jiang using method described in reference [126]. They both are metallic tubes exhibiting small band gap. $(21, 12)$ has a diameter of 2.27 nm and chiral angle of 21.05 degree as the $(44, 17)$ tube is really thick ($d = 4.12$ nm, $\theta_c = 15.66°$.)

4.2 Nonlinear optics

Nonlinear optics relies on higher order polarization of the material i.e. the polarization is dependent nonlinearly on the electric field. Nonlinear optical components include e.g. amplifiers or frequency tunable generators and they are nowadays widely used in many applications. Since nano-objects have high nonlinear polarization, they are interesting building blocks in different nonlinear optics applications. Furthermore nonlinear processes can be used to study the properties of an object and get new information on e.g. dynamics of the system [127]. This chapter describes briefly the nonlinear techniques we have performed to the suspended tubes, and the results we have obtained.

In general, the electric polarization is related to the electric field as $\tilde{P}(t) = \chi^{(1)}\tilde{E}(t)$, where $\chi^{(1)}$ is the linear susceptibility. However, polarization has also nonlinear components (contrary to treatment in section 2.2) and thus it can be expressed as a power series

$$\begin{aligned}\tilde{P}(t) &= \chi^{(1)}\tilde{E}(t) + \chi^{(2)}\tilde{E}(t)^2 + \chi^{(3)}\tilde{E}(t)^3 + ..., \\ &= \tilde{P}^{(1)}(t) + \tilde{P}^{(2)}(t) + \tilde{P}^{(3)}(t) + ...,\end{aligned} \tag{4.6}$$

where $P^{(1)}$ is the linear polarization and the other terms nonlinear components. Good examples of processes related to linear polarization are absorption, reflection, refraction and light propagation. Generally, the electric field is a vector field and hence the susceptibility a tensor but the treatment done in here is for scalars. The nonlinear wave equation has the form

$$\nabla^2\tilde{E} - \frac{n^2}{c^2}\frac{\partial^2\tilde{E}}{\partial t^2} = \frac{4\pi}{c^2}\frac{\partial^2\tilde{P}^{NL}}{\partial t^2} \tag{4.7}$$

and whenever a P^{NL} containing term is nonzero electromagnetic radiation is generated (P^{NL} stands for nonlinear polarization). [128]

4.2.1 Second-harmonic generation

A good example of nonlinear optical interaction is second-harmonic generation (SHG) which is a second-order process as represented in figure 4.8. Let's consider an incident laser beam $\tilde{E}(t) = Ee^{-i\omega t} + c.c.$ (*c.c.* means complex conjugate) aimed on a crystal with nonzero second-order susceptibility. Then the generated second order polarization has the form

$$\begin{aligned}\tilde{P}^{(2)}(t) &= \chi^{(2)}\tilde{E}(t)^2 \\ &= 2\chi^{(2)}EE^* + (\chi^{(2)}E^2e^{-2\omega t} + c.c.).\end{aligned} \tag{4.8}$$

So the second order polarization has a zero frequency term and a frequency dependent 2ω term which can generate radiation at that frequency. However, SHG is possessed only by materials that break the centrosymmetry [129] and e.g. chirality is such a structural property that by default does so [130].

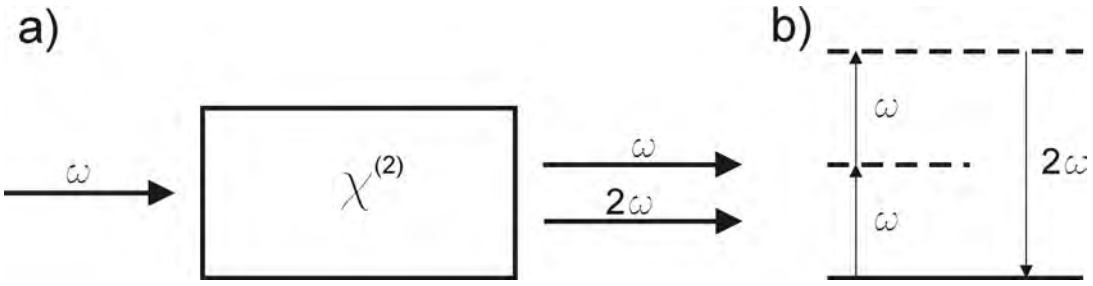

Figure 4.8: (a) Geometry of second-harmonic generation. (b) Energy-level diagram describing the process. Adapted with permission from reference [128].

4.2.2 Four-wave-mixing

Four-wave-mixing is a process which involves third-order polarization and generally the expression of $P^{(3)}(t)$ is very complicated. If the applied field contains three frequency components $\tilde{E}(t) = E_1 e^{-i\omega_1 t} + E_2 e^{-i\omega_2 t} + E_3 e^{-i\omega_3 t} + c.c.$ the polarization is dependent on $\tilde{E}(t)^3$ that leads already to 44 different frequency components ($\omega_4 = \pm\omega_1 \pm \omega_2 \pm \omega_3$)) if distinguishing between positive and negative components.

Time-resolved four-wave mixing relies on short laser pulses and it can be used to study e.g. dynamic processes of the material. It will need laser pulses which are shorter than the coherence time of the system being typically on the order of picosecond or femtosecond. One example of FWM process is CARS (coherent anti-Stokes Raman scattering) which is described in figure 4.9. The first laser pulse (wave vector k_1, energy ω_1) called as the pump pulse excites the system from the energy level i to k. Another pulse, namely the Stokes pulse ($-k_2,\ \omega_2 < \omega_1$) then excites the system to a lower level j. Furthermore, if the energy difference of the pulse is in resonance with one of the vibrational states i.e. $\omega_1 - \omega_2 = \omega_v$ the process is resonance enhanced. Third pulse, the pump ($k_3,\ \omega_3$) excites the system to l level and the photon emitted from there ($k_4,\ \omega_4$) is the measured signal. The energy levels represent states between two electronic states so i and j states are rotational or vibrational states of the electronic ground state and k & l are rotational and vibrational states of the excited electronic state. The time dependence is obtained by varying the time delays between the pulses. In the case of CARS, the pump and Stokes pulses are overlapped in time whereas the time delay between the Stokes and probe pulses is varied and thus the vibrational dynamics of the system is probed. [128] The wave vectors $k_1,\ k_2$ and k_3 determine the direction of the CARS signal k_4. Therefore the signal can be separated spatially from the incident beams. However, when studying small nano-objects the beams have to be focused tightly typically in a collinear geometry and thus spatial separation cannot be used. Therefore, the signal needs to be filtered spectrally from the incident beams.

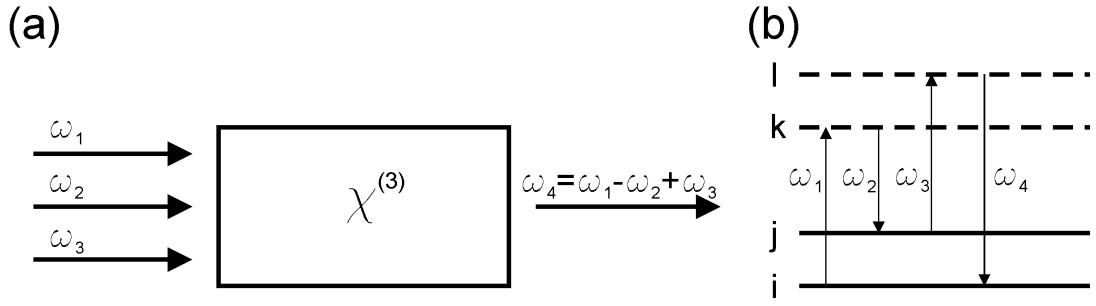

Figure 4.9: (a) Qualitative description of a CARS process. The three incident beams penetrated the sample has been left out for clarity and only the generated, fourth beam is shown. (b) Energy-level diagram describing the process.

4.3 Nonlinear optical measurements from CNTs

4.3.1 FWM measurements on individual CNTs

FWM measurements have been performed earlier by Kim et al. [131] They imaged individual tubes using picosecond pulses and observed signal only from metallic tubes due to the higher polarizability of such tubes. The tubes were lying on top of the substrate hence making the signal-to-noise ratio poor. Later, Sheps et al. [132] from the same group managed to image also semiconducting tubes with lower intensity than metallic tubes. Due to the poor signal-to-noise ratio, suspended tubes over a slit would be easier to study. Previous time-domain spectroscopic studies of SWNTs are made on ensembles that contain thus highly averaged information [133–137].

Suspended samples were fabricated as described in sections 3.2 and 3.3. Then electron diffraction measurements using TEM were performed at Aalto University with Dr. Hua Jiang to obtain the chiral indices and hence the electronic structure of the measured tubes. Furthermore, Raman measurements were performed and with the help of ED and Raman it is possible to design the excitation wavelengths properly for the nonlinear measurements. Raman measurements of suspended CNTs were performed the same way as on the substrate supported samples and are described in chapter 2. However, the diameter dependence from the RBM frequency for the suspended tubes seems to follow the trend obtained in the references [33, 35].

Two different measurement setups have been used to study CNTs. The older system (setup 1) is a home-built system. It contains an amplified femtosecond laser (Quantronix Integra-3.5) with a 1 kHz pulse repetition rate (PRR). The laser is used to pump three homebuilt non-collinear optical amplifiers (NOPA) to produce femtosecond laser pulses of 50 fs. The laser beams are focused to the sample using a microscope objective and additional tube lens and camera is used to view the sample. The signal is detected using a cooled photomultiplier tube

(PMT). Later, a new setup was purchased (setup 2) (see figure 4.10). It uses a Pharos-10, 600 kHz pulse repetition rate (PRR)) laser and two commercial NOPAs (Orpheus-N, Light Conversion) reaching $\sim$ 30 fs pulses. The signal detection is based on photon counting scheme (single photon avalanche photo diode, SPCM-AQRH-14, Excelitas technologies). In both systems residuals of the laser radiation are removed using a dichroic long pass filters (Semrock) and detection wavelength is selected using a band pass filter (Semrock). Detection can be done in either forward or backscattering directions. Timing between the pulses is controlled using optical delay lines in the CARS measurement scheme.

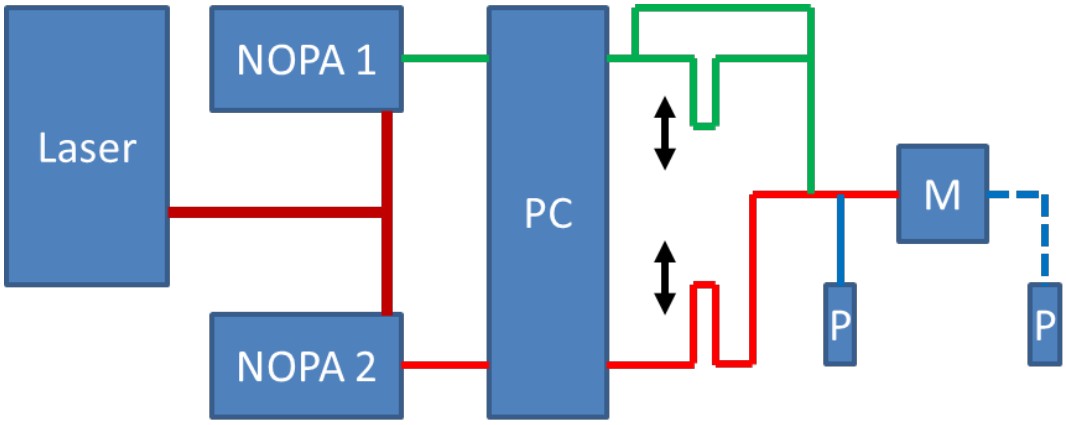

Figure 4.10: Optical arrangement for two color time resolved Four Wave Mixing Microscopy (setup 2). PC pulse compressors, P Photon Counting Avalanche Photodiode, M Microscope.

Samples were moved using piezo-stages and the pulse energies used in spectroscopy measurements were $1 - 2$ nJ/pulse and < 12 pJ/pulse for imaging purposes. The individual spectrum was averaged typically from 1000 pulses per data point. The experiment was done by fixing the pump and Stokes pulses to zero time delay and varying the time delay between the Stokes and probe pulses. The pump wavelength was tuned to 532 nm based on the Raman measurements and the transition energies of the higher electronic resonances were furthermore calculated using equation (2.12) in order to estimate which electronic transitions are in resonance for particular CNT.

A femtosecond FWM signal of a $(24, 9)$ tube is shown in figure 4.11 as a function of the probe delay time. The signal is originated from zero delay between all the pulses when all electronic, vibrational as well as nonresonant effects contribute to $P^{(3)}(t)$. The measured signal is assigned to the electronic response since the time scales in vibrational coherence are longer. The situation, when the exact origin of the contributing process at zero delay is unknown, can be modeled with electronic dephasing (convolution of three pulses with an expo-

nential decaying average system response) which yield to a dephasing time of ~ 45 fs. Even though the result is a crude estimate it is consistent with literature [135, 138]. Both, the ED and Raman measurements confirm that the signal originates from an individual semiconducting tube which was observed for the first time. The FWM signal was measured also from a BBO (barium borate) crystal in forward geometry. The BBO crystal is a well known nonlinear optical material and it gives essentially the convolution of the three pulses. Figure 4.12 shows spectra of SWNT and BBO which are first of all matching with each other and secondly having an energy larger than any of the incident beams. This confirms that the measured signal really originates from FWM process. In addition, a scan across the tube also shows clearly that the signal vanishes outside the tube.

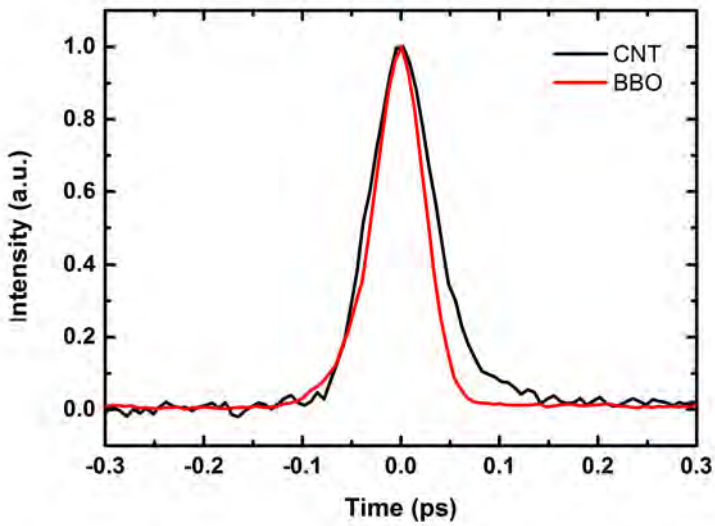

Figure 4.11: Femtosecond FWM signal of a $(24, 9)$ tube assigned using electron diffraction. The signal is measured as a function of time delay between the Stokes and probe pulses.

FWM imaging was done besides recording single spectra. Typical detection time now was $0.2 - 0.4$ s/point. This technique can be used for mapping a large area relatively fast. Figure 4.13 (a) shows a slit that was measured with 590 nm pump (and probe) and 650 nm Stokes pulses. The samples were moved in 0.2 µm steps and the collecting time was 0.2 seconds at each point so the total time to image the slit area took around five minutes. When imaging individual tubes, the collection time can be increased and the step size decreased resulting more accurate images as seen in figure 4.13 (b).

The FWM signal is strongly polarization dependent [131] and the strongest

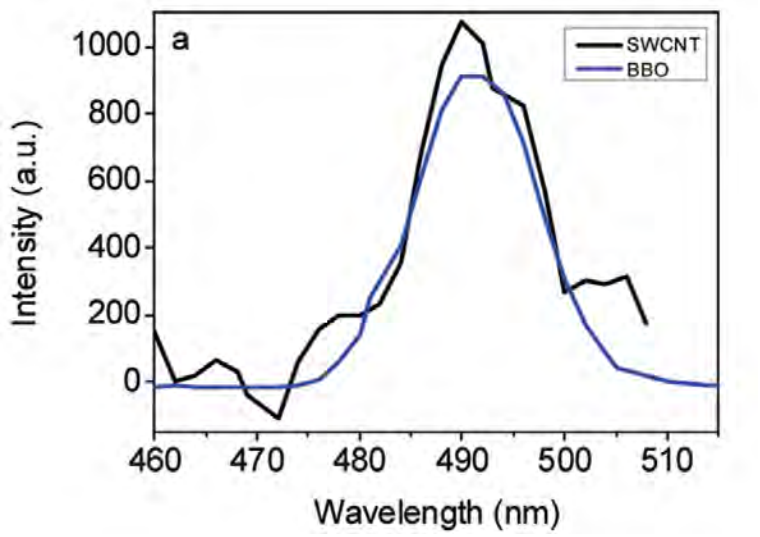

Figure 4.12: Spectrum from BBO (blue line) and from SWNT (black line). Adapted with permission from the paper **A.III.** of this thesis.

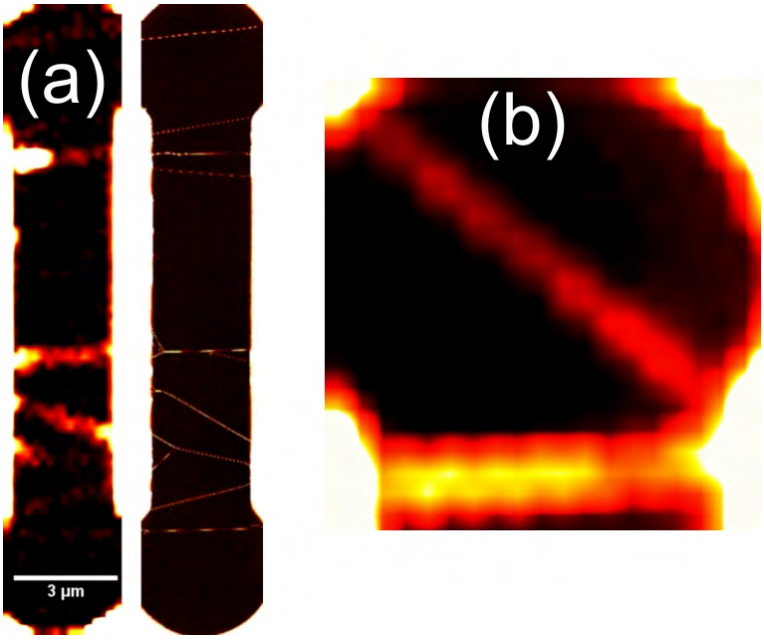

Figure 4.13: (a) FWM (left) and TEM (right) images of SWNTs hanging over a slit. (b) More accurate FWM image of two SWNTs over a slit.

signal is observed when the polarization of the excitation is parallel to SWNT. One nanotube formed a loop and that could be tested for polarization dependent measurements as shown in figure 4.14. The tube is imaged in vertical polarization with respect to image axes (a) and in horizontal polarization (b). Only those sections of the tube that are parallel to the polarization are clearly seen.

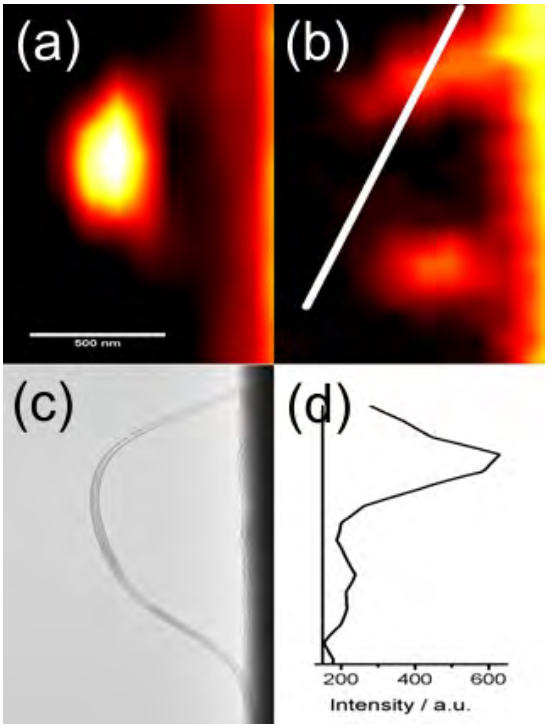

Figure 4.14: FWM images of a loop sample of SWNT with (a) vertical and (b) horizontal polarizations of excitation beams. (c) Corresponding TEM image. (d) Intensity profile along the line marked in (b) with horizontal polarization.

4.3.2 Second harmonic generation from CNTs

SHG has been observed earlier in SWNT thin films [139–141] and SWNTs trapped in zeolites [142]. In the latter study of Su et al. SHG was associated to chirality and large $\chi^{(2)}$ on the order of ~ 400 pm $\cdot V^{-1}$ was obtained which was consistent also with theoretical predictions [143, 144]. However, it was not even evident that SHG signals could be observed from individual SWNTs before this study.

The samples were similar as in the FWM measurements and were first characterized with the electron diffraction. The SHG measurements were performed at Tampere University of Technology under supervision of professor Martti Kauranen. The measurement setup is shown in figure 4.15. The laser pulses (200 fs) were generated using mode-locked Nd:glass laser with 82 MHz PRR and 1060 nm excitation wavelength. The average power of the pulses were ~ 1 mW to avoid damaging the sample and the focused laser spot size was around 800 nm. Since the second-order susceptibility tensor depends on material symmetry and hence the polarization dependent SHG response, a calcite Glan polarizer was used to clean up the linear polarization and furthermore a quarter-wave plate was used to change the polarization circular. The SHG signal was collected in backscattering geometry and separated from the fundamental and possible two-photon fluorescent light by dichroic long pass filter and the detection wavelength is selected using a band pass filter. The detection is done with photomultiplier tube connected to a photon counting unit. The imaging was done by scanning the sample using piezostages and images were acquired using 150 ms pixel dwell time averaged twice within a 5×5 µm scanning area.

The SHG image is shown in figure 4.16 together with SEM and ED images. A strong background on top of the SiN surface hides the signal from the CNTs but it is clearly visible at the slit area corresponding well with the TEM data. The SHG signal vanishes quite soon below the noise level when excitation power is reduced and hence it was difficult to measure the single spectrum reliably. The estimation of the second order susceptibility for the $(42, 1)$ tube is ~ 57 pm $\cdot V^{-1}$ and the possible sources of a SHG signal include chirality, lattice defects and tube deformations. Since the signal intensity is similar in bent and straight sections the deformation was discarded as a possible reason. The ED patterns confirm the lack of defects so the chirality seems to be the most plausible origin of the SHG signal.

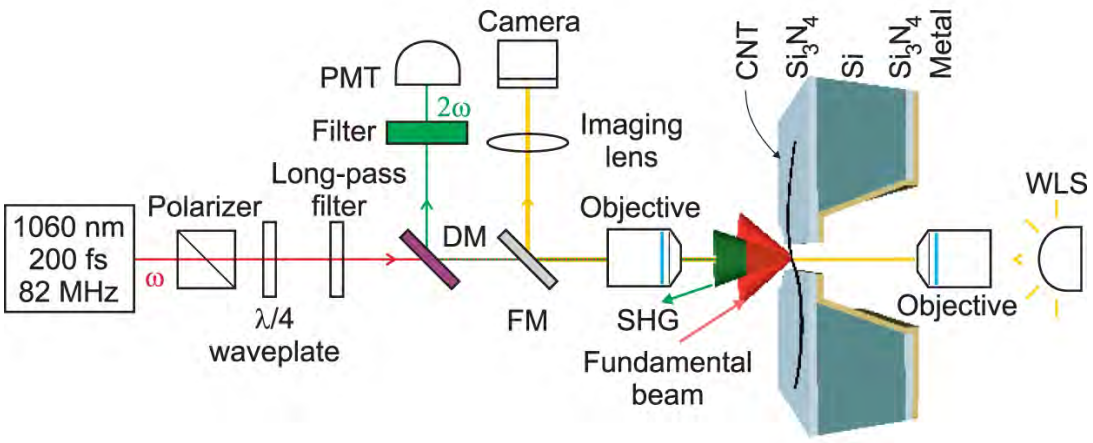

Figure 4.15: Schematics of sample geometry and SHG microscopy setup. A pulsed and collimated beam from an ultrafast laser was passed through a polarizer and a quarter-wave plate to generate circularly polarized light and focused to the sample by an objective ($NA = 0.8$). A long-pass filter was used after the polarization optics to block SHG from those elements. Reflected SHG (2ω) was separated from the fundamental excitation wavelength (ω) by a dichroic mirror (DM) and an interference filter and detected by a photomultiplier tube (PMT). A white-light source (WLS), camera and flip mirror (FM) were used to find the sample before SHG imaging. Adapted with permission from the paper **A.IV.** of this thesis.

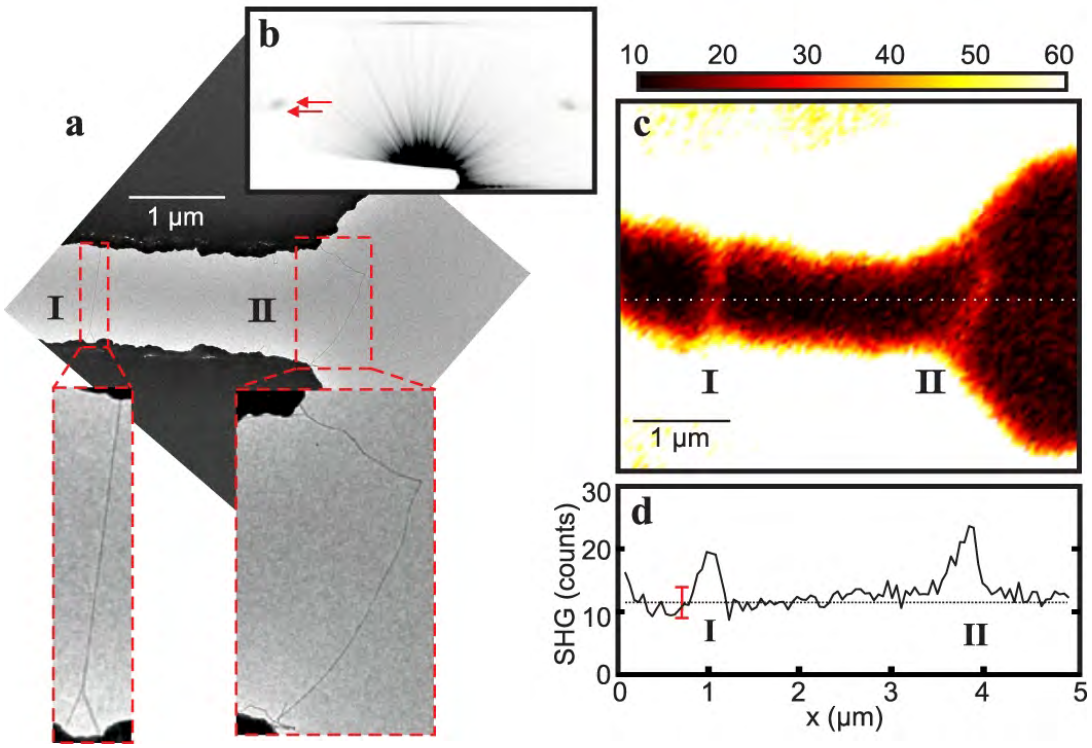

Figure 4.16: TEM and SHG characterization of suspended SWNTs. (a) TEM image of the sample, featuring a bundle of 45 CNTs on the left (I) and an individual SWNT on the right (II) suspended across the horizontal slit opening (bright area) in the SiN membrane (dark area). (b) ED pattern from (II) identified as $(42, 1)$ tube. The separated layer-lines indicated by two arrows clearly demonstrate that the nanotube has a chiral structure, which is very close to a zigzag tube. (c) SHG image of the sample showing the two suspended SWNT structures (I and II) over the air slit. (d) A line profile, formed by averaging eight adjacent line profiles, was taken from the SHG image (dotted white line in (c)) to visualize the signal-to-noise ratio (around 2) of the measurement. The mean background value (11.5 counts) of the measurement is shown as a dotted line and the calculated standard deviation (5 counts) as a red bar. Adapted with permission from the paper **A.IV.** of this thesis.

Chapter 5

$1/f$ noise in MWNTs

There are only few systematic studied of the origin of low-frequency noise in ballistic CNTs and earlier noise studies have been mainly concentrated on SWNTs in diffusive regime. Even fewer studies of noise properties have been done on MWNTs and they present an interesting research field since they can exhibit ballistic conduction with negligible Schottky barriers at the contacts. In general, low frequency noise in CNTs is dominated by the $1/f$ noise and hence other types of noise such as shot noise or thermal noise is left out of the discussion here.

$1/f$ noise was discovered in 1925 when J. B. Johnson studied current fluctuations of electronic emission in a thermionic tube. He noticed that besides of the frequency independent shot noise, there was other kind of noise which was increasing with decreasing frequency. Next year, in 1926, W. H. Schottky proposed that this noise arises from slow random changes of the thermocathode's surface and called it flicker noise. In the following years, such noise was found in several semiconductor devices and later on in metals, semimetals etc. An example of the spectrum of such noise is given in figure 5.1. [145]

5.1 General properties

Noise originates from random processes. Random process can be described as a random function $x(t)$ of time. Furthermore, if $< x >$ is the mean value of the random function, then deviation from the mean value is $\delta x(t) = x(t - < x >)$ which is also random. The correlation function is used to analyze the kinetics of the random fluctuations and it shows how the fluctuations evolve in time on average. The correlation function averaged over long time of measurement t_m is defined as

$$\psi_x(t_1 - t_2) \equiv \overline{\delta x(t_1)\delta x(t_2)} = \lim \frac{1}{t_m} \int_{-t_m/2}^{t_m/2} dt \delta x(t_1 + t)\delta x(t_2 + t). \qquad (5.1)$$

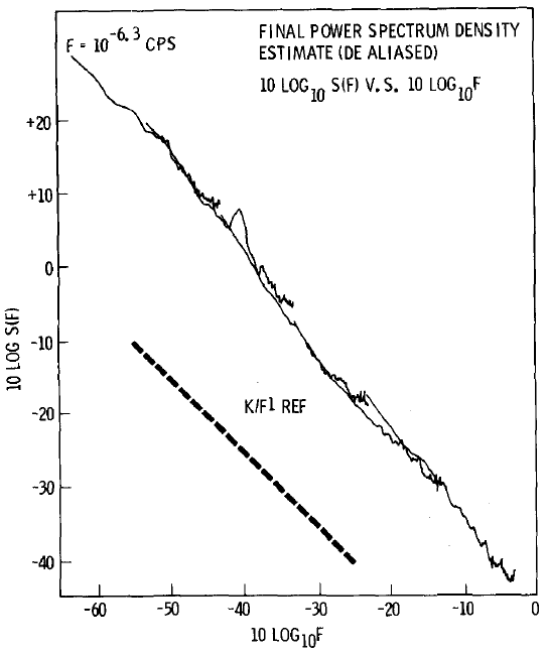

[h]

Figure 5.1: Spectral density of noise in an operational amplifier. Adapted with permission from reference [146].

Furthermore, the random noise signal can be represented as a Fourier integral

$$\delta x(t) = \int_{-\infty}^{\infty} \frac{d\omega}{2\pi} \delta x(\omega) e^{-i\omega t} \tag{5.2}$$

which reduces as an integral over positive frequencies ($\delta x(t)$ is a real quantity)

$$\delta x(t) = \int_{0}^{\infty} \frac{d\omega}{2\pi} (\delta x(\omega) e^{-i\omega t} + \delta x^*(\omega) e^{i\omega t}). \tag{5.3}$$

If considering a signal analyzer containing a band-pass filter where $\bar{f}$ is the central frequency and δf the bandwidth of the filter measuring fluctuating signal $\delta x(t)$ (see figure 5.2), the signal at the output is then $\delta x(t|\bar{f}, \Delta f)$ and it contains only the frequencies from $f_1 = \bar{f} - \delta f/2$ to $f_2 = \bar{f} + \delta f/2$. Thus the output signal is

$$\delta x(t|\bar{f}, \Delta f) = \int_{\bar{\omega}-\Delta\omega/2}^{\bar{\omega}+\Delta\omega/2} \frac{d\omega'}{2\pi} [\delta x(\omega') e^{-i\omega' t} + \delta x^*(\omega') e^{i\omega' t}]. \tag{5.4}$$

The noise power is by definition this signal squared and it fluctuates around its mean value $\overline{[\delta x(t|\bar{f}, \Delta f)]^2}$. If averaging over identical noise sources and over measurement time, we get the expression

$$\overline{[\delta x(t|\bar{f}, \Delta f)]^2} = 2 \int_{\bar{f}-\Delta f/2}^{\bar{f}+\Delta f/2} df \psi_x(\omega) \approx S_x(\bar{f}) \Delta f, \tag{5.5}$$

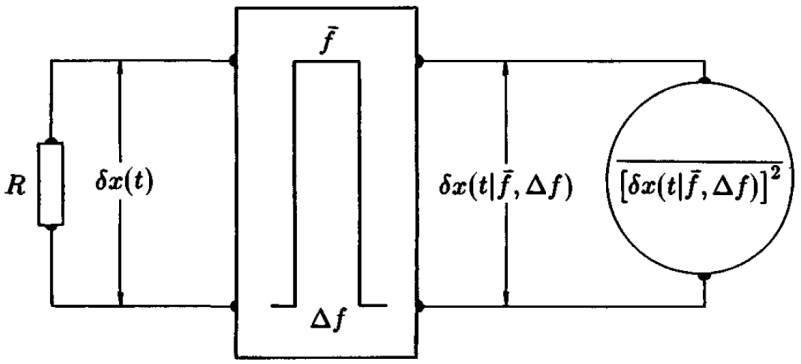

[h]

Figure 5.2: Schematic diagram of a spectral analyzer for spectral density of noise measurement. R is the source of time-dependent fluctuations $\delta x(t)$. The rectangular box in the middle denotes a bandwidth filter with pass-band Δf and central frequency $\bar{f}$. $\delta x(t|\bar{f},\Delta f)$ is the output (filtered) random signal. $\overline{[\delta x(t|\bar{f},\Delta f)]^2}$ is the power of the filttered signal. Adapted with permission from reference [145].

where $\psi_x(\omega)$ is the Fourier transform of the correlation function $\psi_x(t_1-t_2)$. This equation defines then the spectral density of noise which is noise power per unit frequency band. Furthermore,

$$S_x(f) = 2\int_{-\infty}^{\infty} d(t_1-t_2)e^{i\omega(t_1-t_2)}\psi_x(t_1-t_2) \equiv 2\psi_x(\omega) \tag{5.6}$$

meaning that the spectral density is twice the correlation function. This is also known as the Wiener-Khintchine theorem. [145]

$1/f$ noise seems to be universal and occurring in all materials. The experimental noise spectra from different materials reveal that the spectral density $S(f) \propto f^{-\alpha}$, where α is usually between 0.8 and 1.4 [147] over a broad frequency range, not exactly one. At high frequencies, depending on material, $1/f$ noise becomes negligible since other, frequency independent sources of noise such as shot noise becomes dominant.

In field effect devices such as MOSFETs (metal-oxide-semiconductor field-effect transistor) and CNT transistors, the dominating sources of the $1/f$ noise are the interface effects between the gate dielectric and the channel. Hence the noise theory discussed here focuses mainly on device noise.

5.1.1 Hooge's relation

Since $1/f$ noise very often follows the abovementioned power law and is also proportional to the square of a measured quantity, F.N. Hooge postulated in 1969 [148] that there is a universal coefficient and an empirical formula describing the

noise:

$$\frac{S_R(f)}{R^2} = \frac{\alpha_H}{N_c f}, \tag{5.7}$$

where α_H is a universal coefficient called Hooge's constant having a value of $2 \cdot 10^{-3}$, R resistance and N_c the number of charge carriers. Often α_H / N_c is defined as the noise parameter A. The original experiments by Hooge were done in Au films which were doped differently to modulate the mean free path. It is good to remember that this relation is mainly empirical and the value of Hooge's constant can differ significantly in different materials [145]. Yet, Hooge's model is the only model which gives a crude estimate of the noise magnitude in various different materials and should thus not be underestimated.

5.2 Random telegraph signal noise

The states of charge carriers in semiconductors can be divided into localized or delocalized ones. Delocalized states contribute to the conduction through the valence (holes) or conduction band (electrons). The trapping (by localized states) and detrapping (back to the band) of the charge carriers is called generation and recombination, respectively. These generation-recombination processes are random and hence the number of carriers in delocalized states fluctuates around a mean value determining the conductance and the resulting noise is called generation-recombination (G-R) noise. The exact processes of generation and recombination mechanisms are quite complex and vary from material to material. [145]

Such noise in MOSFETs is usually thought to originate from the charge traps at the oxide near the interface of the semiconductor caused by either carrier number or carrier mobility fluctuations (see section 5.3).

Let's consider a single fluctuation which can be described by a Lorentzian function

$$S_I(\omega) = \frac{4\tau I^2}{1 + \omega^2 \tau^2}, \tag{5.8}$$

where τ^{-1} is the characteristic time constant and $\omega = 2\pi f$. The $1/f$ spectrum is then easily formed by the superposition of these elementary acts. Sometimes clear switching between two (or more) values of e.g. current as a function of time is clearly observed and called as random telegraph noise (RTN) as seen in figure 5.3. This can happen especially in small devices where a single trap can have a big influence on device performance. This is reflected in the appearance of Lorentzian components in the line shape of the noise spectrum in the frequency domain. [145, 147, 150]

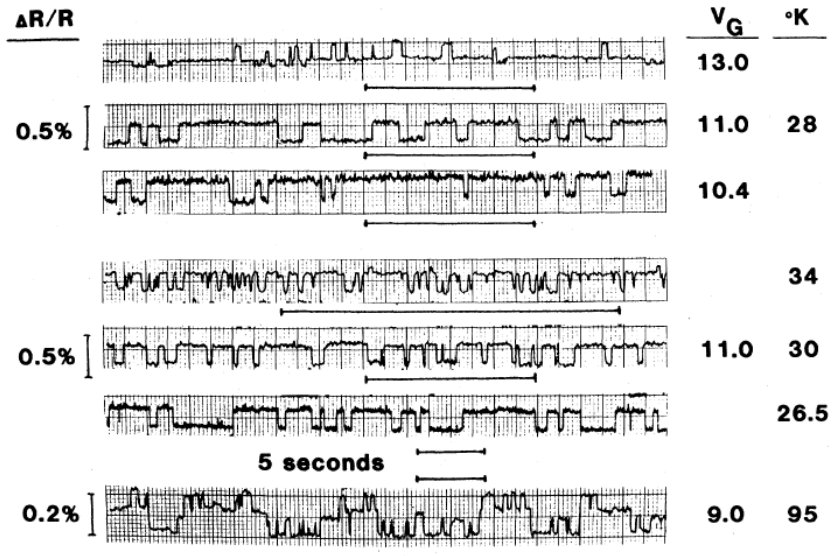

Figure 5.3: Resistance switching observed in a small MOSFET in a particular range of temperatures and gate voltages. The duty cycle depends on gate voltage, while the overall rate decreases with temperature (note scale changes). The last trace demonstrates that superposition can lead toward $1/f$ noise. Adapted with permission from reference [149].

5.3 Interface effects

An increasing number of models explaining fluctuations arising from the interface effects have been developed which fall into two categories: mobility fluctuation or number fluctuation models [151]. We will concentrate on those models since CNT-FET as well as the MOSFET can be regarded as interface dominated devices.

McWhorter suggested in 1957 that the $1/f$ noise in semiconductors originates from fluctuations at the interface of the semiconductor and the oxide [147, 152]. These fluctuations arise from trapping and detrapping of charge carriers between the surface layer of the conductor and the oxide. The transfer from or into a trap is simple quantum tunneling and the main reason of the noise level is the trap density near the interface. Such a model is essentially the number fluctuation model and is widely used in MOSFETs. However, much debate about the origin of the noise still remains as Vandamme et al. [153] concluded. In order to study the validity of the models they studied the noise as a function of gate voltage and found that in models based on mobility fluctuations α_H is independent of gate voltage and hence $S_I/I^2 \propto 1/V_g$ while in number fluctuations based models $\alpha_H \propto 1/V_g$ and hence $S_I/I^2 \propto 1/V_g^2$. Later on, unified noise models based on carrier number fluctuations and correlated mobility fluctuations have been proposed to describe MOSFETs. Correlated mobility fluctuations are attributed to Coulomb scattering of free carriers at trapped interface charges by Vandamme & Vandamme [154]. They concluded that the unified noise models predict that $\alpha_H \propto V_g$ as in number fluctuation models which is in clear contradiction of the experiments done in p-type MOSFETs.

Dmitriev et al. [151] studied the noise mechanisms by using a unified approach. The carrier number fluctuations can be understood within the framework of generation-recombination noise. The noise of one elementary act is well known and described by the Lorentzian (see section 5.2) and the spectral density of current noise caused by trapping and detrapping of carriers is given as

$$\frac{S_I}{I^2} = \frac{\lambda k T N_{tv}}{f A_g n_s^2}, \tag{5.9}$$

where λ is the tunneling constant, A_g the gate area, n_s the 2D electron concentration in the channel and N_{tv} the trap concentration in the oxide. They concluded that noise is proportional to $1/n_s^2$ and not as $1/N_c$ as stated in equation (5.7). Mobility fluctuations can be understood also as a result of superposition of elementary acts. The channel has scattering centers with associated scattering cross sections σ (probability of scattering event) which will fluctuate between the two values σ_1 and σ_2. In case of the interface effect, trapping of carriers can be such an elementary act but also the tunneling transition between two nonequivalent positions of an atom, motion of dislocations etc. can be the mechanism. Again the elementary act is described by a Lorentzian and the spectral density of the

noise is expressed as

$$\frac{S_I}{I^2} = \frac{4N_{t\mu}}{V} \frac{\tau w(1-w)}{1+(\omega\tau)^2} l_0^2(\sigma_2 - \sigma_1)^2, \tag{5.10}$$

where $N_{t\mu}$ is the concentration of scattering centers, l_0 the mean free path of the charge carriers, and w the probability for a scattering center to be in state associated to the cross section σ_1. Since N_c is not present in the equation, they suggested that mobility fluctuations cannot be explained by using Hooge's relation (5.7). Furthermore, Dmitriev et al. studied correlated noise to form a 1/f spectrum that includes components from both number and mobility fluctuations.

There is still a lot of debate about the origin of the noise in MOSFETs and many different models including number fluctuation, mobility fluctuation or correlated models have been developed each having their own supporters.

5.4 Noise in ballistic systems

Most of the noise models concentrate on diffusive transport and not on ballistic. Progress in semiconductor technology in the 80's opened possibilities to realize ballistic conduction in a relatively easy way. Such systems were called quantum point contact (QPC) devices and they were made by shaping the two-dimensional electron gas (2DEG) with gate electrodes [145] to form narrow constriction.

Noise studies of QPC revealed $1/f$ type noise with either clearer $1/f$ or a more Lorentzian spectrum and the origin of the noise was related to switching between two or more states of an electron trap [145, 155, 156] and is hence attributed to RTN. These switching events affect the transmission and reflection probabilites and hence modulate the conductance. Dekker et al. [155] suggested that trap states near the contact will induce a fluctuating electric field acting as a local gate so noise $S_G \propto (\delta G/\delta\epsilon_f)^2 \propto (\delta G/\delta V_g)^2$, where ϵ_f is the Fermi energy in the effective part of the contact.

5.5 $1/f$ noise in carbon nanotubes

The first noise study of individual CNTs was published in 2000 by Collins et al. [157]. Beside individual tubes they studied also nanotube networks with different thicknesses. They noticed unexpectedly large noise levels and a Hooge constant many orders of magnitude larger than expected in Hooge's law. They attributed the origin of the noise to surface fluctuations as distinguished from the bulk fluctuations. After that more studies of $1/f$ noise have been done and the source of the noise has been attributed to both number [158, 159] and mobility [160–162] fluctuations.

RTN is quite common in CNTs [163, 164] as they are one realization of nanoscale FETs. RTN have been found from both metallic and semiconducting tubes with current variability as high as 50 % reaching even to the ON-state

where the noise have the smallest value. The origin of the RTN in CNTs is consistent with the models of trapping and detrapping of charges at the interface and verified also for ballistic CNT devices [165]. In multiwalled tubes, however, RTN was also ascribed to the fluctuations at the contact [166].

5.5.1 Diffusive transport models

Since Hooge's relation (5.7) states that the noise is inversely proportional to the number of charge carriers N_c and on the other hand in one dimensional FET working in the ON-state [160] $N_c = c_g L|V_g - V_{th}|/e$ (c_g is the gate capacitance per unit length, L the device length, V_g the gate voltage, V_{th} the threshold voltage of the FET and e electronic charge) the inverse noise magnitude can be rewritten as

$$\frac{1}{A} = \frac{c_g L|V_g - V_{th}|\ f}{\alpha_H e} \tag{5.11}$$

and therefore $1/A \propto |V_g - V_{th}|$ for mobility fluctuations and $1/A \propto |V_g - V_{th}|^2$ for number fluctuations ($\alpha_H \propto 1/|V_g - V_{th}|$). Ishigami et al. [160] showed that their semiconducting individual SWNTs with channel lengths from microns to tens of microns measured in ultra-high vacuum follow the mobility fluctuation model. Furthermore, they noticed that the coefficient $D = c_g L/\alpha_H e$ is proportional to the channel length as expected for diffusive transport.

Briman et al. [158] on the other hand, ended up at the opposite conclusion and stated that the noise originated from number fluctuations. They minimized interface effects by using an electrolyte gate. They also used nanotube networks instead of individual tubes with relatively large distance between source and drain electrodes. The main conclusion was that since A/R, where A is the noise parameter and R the device resistance was dependent on gate voltage (which furthermore reduces so that $A/R \propto \alpha_H$), the noise has to originate from number fluctuations. Actually they distinguished two different noise sources that come from the surrounding environment and from the nanotube channel itself and claimed that their setup probes the noise from the nanotube itself.

The abovementioned studies were done in the diffusive transport regime. However, especially single walled nanotubes have long mean free paths and are hence regarded as ballistic conductors. On the other hand, SWNTs will form noticeable Schottky barriers at the metal electrode interface and they operate as Schottky barrier (SB) FETs [16, 18, 67]. Lin et al. [159] studied such Schottky barrier FETs working in the ballistic or close to ballistic i.e. quasi-ballistic regime made of individual semiconducting SWNTs. They showed that the noise followed Hooge's relation (5.7) with the Hooge constant comparable to many bulk materials and that the relation is valid also for ballistic transport. Furthermore they attributed the origin of the noise to the carrier number fluctuations and the relatively large noise levels to the small total amount of charge carriers in the 1D system.

5.5.2 Charge noise model

About one year later in 2007 Tersoff [167] made a study of noise in ballistic FETs using simulations and Lin's data [159]. Since diffusive transport models don't have theoretical basis in ballistic systems (even though they could explain noise reasonable well), he proposed a charge noise model which has its origin in noise of ballistic conduction done in quantum point contacts in the early 90's [155]. The same analysis is valid regardless of having Schottky barriers or not at the contacts. In both cases the fluctuations affect to transmission probability either at the contacts or then at the channel itself. The normalized spectral density of the noise can be presented as

$$\frac{S_I}{I^2} = \gamma^2 S_g^2 \left(\frac{d\ \ln I_d}{d\ V_g} \right)^2 , \tag{5.12}$$

where γ describes either the intrinsic electrostatic fluctuations at the SB contact or the fluctuation of the barrier along the channel (channel-limited FET) since in channel-limited CNT-FETs the Fermi level at the channel can be modulated with the gate voltage and hence the channel itself acts as a tunnel barrier.

The analysis carries very well over the subthreshold region as seen in figure 5.4 (b) (dashed line) even though it is derived by making many simplifications. As seen, the slope is correct but the coefficient $\gamma^2 S_g^2$ is adjusted to shift the data vertically. Equation (5.12), however, doesn't seem to explain the data very well, when the device is switched to the ON-state and the current starts to saturate. The given explanation according to Tersoff was that the analysis didn't take into account any scattering in the channel but just the SB contacts itself. And furthermore, fluctuations of the charge traps will induce fluctuations to the transmission probability also in truly ballistic devices as described in subsection 5.4. Therefore a model of two resistors in series is introduced: the other one the charge noise term describing either the fluctuations to the contacts or to the channel (that holds in the subthreshold region) and the other one the noisy resistor independent from the gate voltage. This is justified because the transmittivity of the contacts and the transmittivity of the channel can be handled separately being in series. In the linear regime then the effect of the channel is equivalent to adding classical noisy resistance. The interpretation of the noisy resistor for the SB-device is that in the ON-state the contacts become more transparent and the effects of the channel cannot be neglected (e.g. scattering in quasi-ballistic devices). In the channel-limited case the interpretation is not that straightforward and the second term might come either from the contact or from the channel so the noise might have a different original mechanism that is dominating in the given region. Adding the noisy resistor in the analysis we get,

$$\frac{S_I}{I^2} = \gamma^2 S_g^2 \left(\frac{d\ \ln I_d}{d\ V_g} \right)^2 + \alpha_c I_d^2, \tag{5.13}$$

where $\alpha_c = A_c(R_c/V_d)$ and $A_c = (\delta R_c)^2/R_c^2$ is the noise parameter of a classical

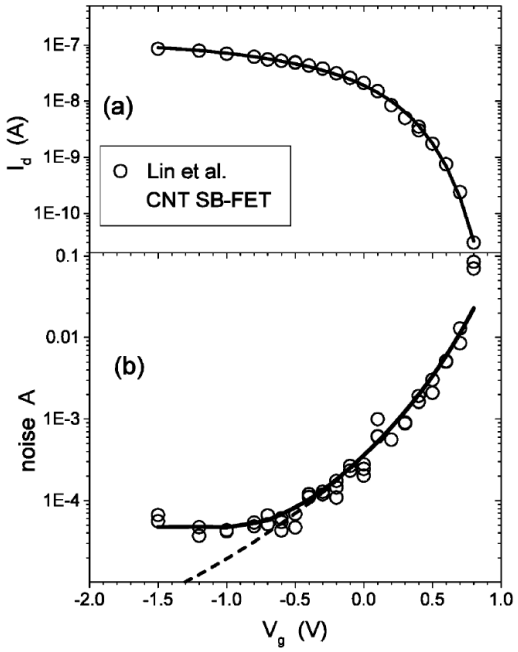

Figure 5.4: Comparison of theory with experiment (Lin et al.[159]) for noise in a CNT SB-FET. (a) Circles are measured current I_d vs V_g. Solid line is a smooth fit to allow differentiation. (b) Circles are measured noise A vs V_g. Dashed curve is equation (5.12), the predicted noise for a ballistic SB-FET; the coefficient giving the overall magnitude (a vertical shift on this log scale) is the only adjustable parameter. Solid curve is the same prediction including additional scattering (modeled as a series resistor) as in equation (5.13), with one additional parameter chosen to fit the noise in the high-current regime. Adapted with permission from reference [167].

resistor. As seen from figure 5.4, equation (5.13) fits well in the entire range. Tersoff verified the accuracy of the model also for the channel-limited FET where the SBs were minimized using local gates underneath the contacts [167]. Soon later, Mannik et al. [168] reported noise behavior following a charge noise model in liquid-gated SWNT-FETs. They concluded that in this case the origin cannot be the gate oxide but rather some other charge fluctuations in the vicinity of the tube. The same group also validated the model for liquid-gated graphene transistors [169] after that.

5.5.3 Noise in MWNTs

Roschier et al. [170] in 2001 studied a noise in MWNT-SET (single electron transistor). They tried to minimize the interface effects caused by the oxide by fabricating hanging tubes i.e. depositing tubes on top of the contacts. They got

total noise levels comparable to state-of-the-art metallic devices and concluded that white noise will dominate the noise in frequencies above 3 kHz. Next year Quacha et al. [171] studied noise properties of MWNT and made the conclusion that the noise indeed is $1/f$-type originating from conductance fluctuations. Tarkiainen et al. [166] studied the noise also at low temperatures. They observed RTN at low temperatures and concluded that the noise was originating mainly from the CNT-metal contact. All the previous studies were made, however, in nanotubes larger than 10 nm or channel lengths so long, that the devices were working in the diffusive transport regime (channel length > 1 µm). Lassagne et al. [172] studied tubes with diameters ranging from $3-15$ nm. Their high quality quasi-ballistic MWNT's were demonstrated to be low-noise conductors with the noise originating from extrinsic sources, probably from the contacts. The temperature studies of noise in MWNTs reveals that the noise is temperature independent for quasi-ballistic tubes [172] but decreases by a factor of $10-100$ in diffusive tubes [166] which is also consistent for diffusive SWNTs [162]. None of these studies, however, concentrated on the actual noise mechanisms and were interpreted by using diffusive noise models.

5.6 Results

In this work, low-frequency noise properties of small-diameter MWNTs were studied. In general, there are very few systematic studies of even electrical transport [173] not to mention noise in such nanotubes. More studies have been done in larger diameter MWNTs (> 10 nm), e.g. [55, 174, 175]. Usually such devices are more disordered leading to diffusive transport. Most of the electrical current in MWNTs is carried by the outermost tube layer when using normal top contacts but intershell effects also attribute to the conduction leading to unexpected quantum conductance through the system even with fractional values of quantum conductance [176]. On the other hand values of even $\sim 400\, G_0$ have been obtained in large diameter MWNTs using end contacts forming ohmic contacts to all the different shells in the tube [177].

Intermediate sized nanotubes ($d < 10$ nm) were chosen since such tubes are reaching ballistic limit, have negligible or small Schottky barriers at the contacts which is an unexplored field in the CNT literature. In principle these tubes in low temperatures leads to the realization of truly channel-limited FETs offering a good platform to study noise in ballistic systems. The samples were fabricated as described in section 2.4 and the measurements were performed using a similar kind of setup as in section 2.5.1. Now just a low pass filter is applied to the setup after the current preamplifier to remove any aliasing effect. A voltage preamplifier (DL instruments 1201) was used for that purpose. The time series with different gate voltages were recorded using a 250 Hz bandwidth with a LabView program and Matlab was used furthermore to analyze the data. The details of the measuured tubes are given in table 5.1.

Table 5.1: Diameter d, channel length L_C, ON-state resistance R_{ON}, fitting parameter γS_g (p-side), fitting parameter α_c (p-side) and gate capacitance c_g per unit length for three measured devices and one from ref. [159]

	d (nm)	L_C (nm)	R_{ON} (kΩ)	γS_g (meV)	α_c (1/Hz)	c_g (pF/m)
Tube A	7.1	130	6.2	0.5	$1x10^4$	42
Tube B	6.0	420	18.4	0.6	$5x10^5$	41
Tube C	3.0	390	15.0	0.3	$4x10^5$	36
Tube D	7.1	570	10.0	0.3	$5x10^4$	42
Ref. [159]	1.8	600	~ 10	7.0	-	70

Typical noise spectra are seen in figure 5.5 where the power spectral density of current is shown as a function of frequency at different bias and gate voltage values. In some values the spectrum is more $1/f$ type as other values reveal a Lorentzian line shape pointing towards two-level fluctuations i.e. RTN. Basic transport measurements with gate curves were carried out and the functional dependence of $I_{sd}(V_g)$ was found to be exponential in the subthreshold regions. Furthermore, the noise was recorded as a function of gate voltage (see figure 5.6). The normalized noise was obtained by averaging over a $20 - 40$Hz frequency octave. Interestingly the normalized noise was found to be one to two orders of magnitude lower than reported in SWNTs [159–162] and one order of magnitude lower than previously studied in quasi-ballistic MWNTs [172]. The lower noise in MWNT-FETs might be owing to the larger diameter of the tubes as the sensitivity of the current through the CNT channel on individual traps is reduced compared to SWNTs.

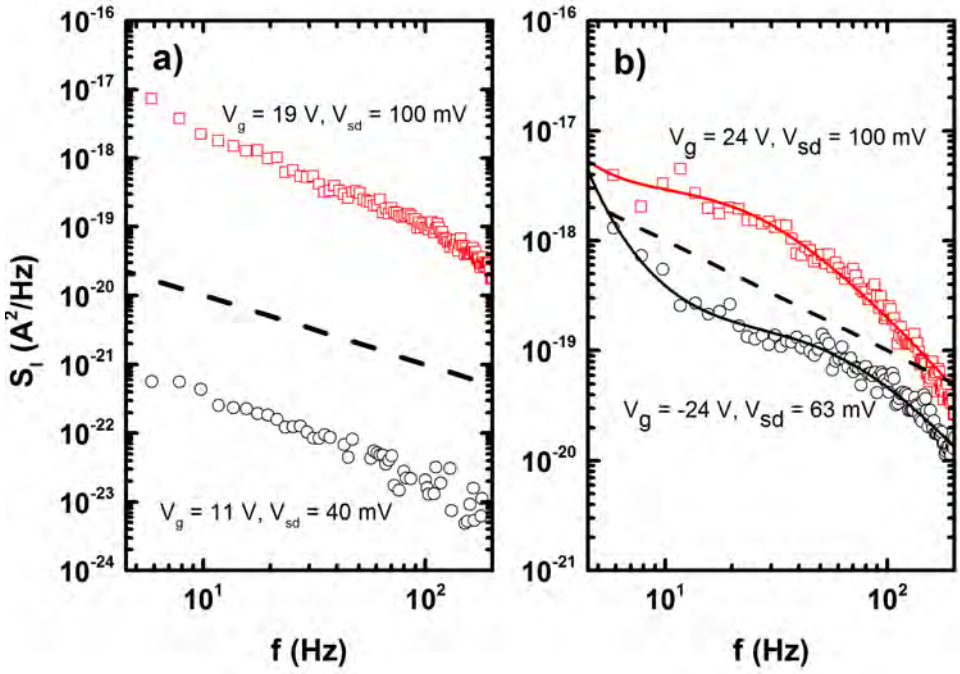

Figure 5.5: Current power spectral density S_I as a function of frequency for tube A at various V_{sd} and V_g voltages. (a) Noise spectra following $1/f$ line shape (indicated by the dashed line). (b) Noise spectra revealing Lorentzian line shapes. The continuous curves are Lorentzian fits to the data.

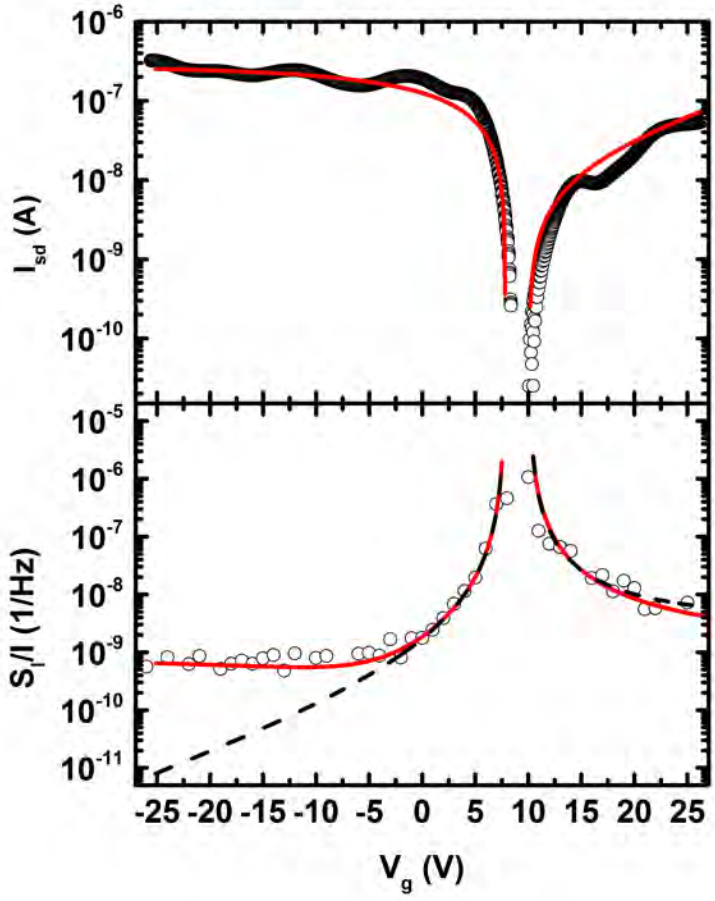

Figure 5.6: (a) Smoothed source-drain current as a function of gate voltage for tube A (dots) and exponential fit to the data (red curve). Gate curve is measured with 1 mV bias voltage. (b) Normalized noise amplitude vs. gate voltage for the same device. Dots are the experimental data, dashed lines fits made by using charge noise model and solid lines using charge noise model including noisy resistor.

5.6.1 The McWhorter model

We can analyze the noise in the framework of the McWhorter model by studying its gate voltage dependence. As described in the section 5.5.1 the inverse normalized noise I^2/S_I is proportional to $|V_g - V_{th}|^2$ in the case of number fluctuations ΔN and $|V_g - V_{th}|$ in the case of mobility fluctuations $\delta\mu$. Therefore, plotting the inverse noise on a log $-$ log-scale as a function of $|V_g - V_{th}|$ will provide an approximation of the exponent of $|V_g - V_{th}|$ and thus discrimination between ΔN and $\Delta\mu$ models and even the applicability of the whole McWhorter model. The plotting is done in figure 5.7. The exponent is 1.89 from 1 to 10

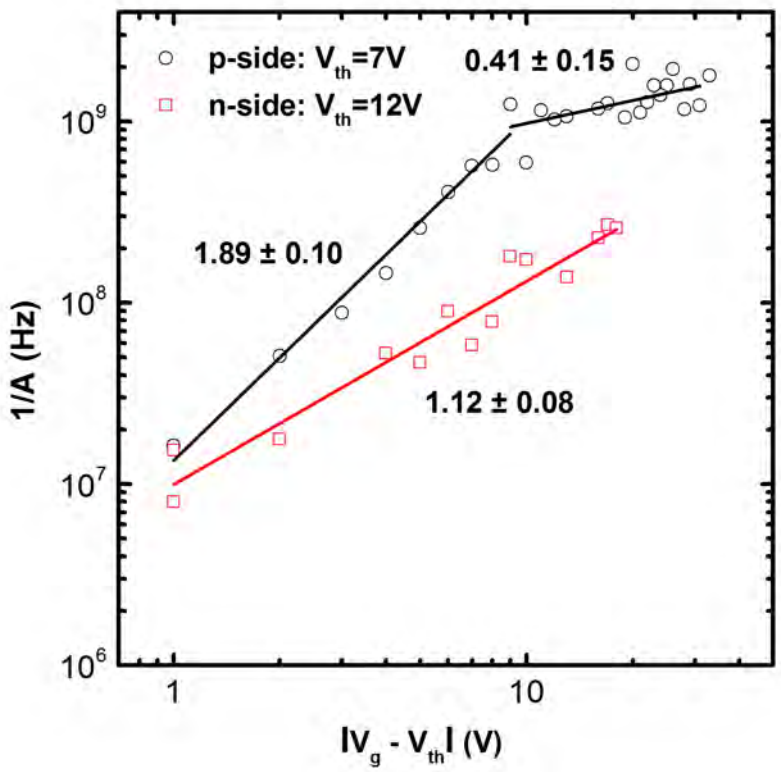

Figure 5.7: Inverse noise magnitude of tube A as a function of $|V_g - V_{th}|$ for p-side (black dots, $V_{th} = 7$V) and for n-side (red dots, $V_{th} = 12$V). Solid lines are liner fits to the experimental data revealing the exponents. Two different exponents (1.89 and 0.41) are present in the p-side and one value of 1.12 in the n-side.

Volts. This could be a sign of number fluctuations. On the other hand in the high voltage regime, the exponent deviates significantly from the expected value of 2 ($0.41 \pm +.15$). This is in clear disagreement with the McWhorter model. In

the n-side the exponent 1.12 could indicate mobility fluctuations as the source of noise. However, the voltage range is fairly small on the n-side so the behavior in the high voltage regime might stay hidden. Let's determine the coefficients from equation (5.10) as $D := C_g L_c/\alpha_H e$. The gate capacitance of the tube can be estimated from $C_g = 2\pi\epsilon_0\epsilon_r/\ln(4h/d)$, where ϵ_r is the dielectric constant, d the tube diameter and h the thickness of the gate oxide. If taking as the literature value for α_H [160] of $\sim 10^{-2}$ and other parameters as in table 5.1, we get the value of $\sim 10^{-6}$ which is many orders of magnitude off from experimentally obtained values of $1.5 \cdot 10^7$ for n-side and $5 \cdot 10^7$ for p-side. Based on the observed facts, it is clear that the McWhorter model fails to explain the noise in our devices. It should not come as surprise since the devices are working in the ballistic region. The noise magnitude seems to be independent from the channel length in the studied range (see table 5.1) which also supports the evidence of ballistic conduction.

5.6.2 The charge noise model

Next we analyze the results by using the charge noise model. First, an exponential fitting is done to the obtained $I_{sd}(V_g)$ curve which is furthermore differentiated. The parameter γS_g is used to fit the data in the subthreshold region. As seen from figure 5.6 the fitting is excellent in the subthreshold region. However, in the ON-state of the p-side the deviation from the noise starts to grow as the current starts to saturate. By adding the noisy resistor to the analysis, the data fits well through the whole gate range. In the n-side there is not much of a difference if adding the second term to analysis which is quite expectable since gate range and gate modulation are smaller. The analysis is done separately to the p- and n-sides and thus there is a gap in the data at the OFF-state. The charge noise model thus explains the noise behavior accurately throughout the whole gate range.

The fitting parameter γS_g (given in table 5.1 for all tubes) is one order of magnitude smaller than in the analysis done by Tersoff [167] to the data by Lin et al. [159]. The parameter γS_g is related to the gate capacitance [168] as $\gamma S_g \propto (1/C_g)^2 S_q$, where S_q is the charge distribution fluctuation. The capacitance per unit length c_g for the SWNT used in Lin's work is over twice the values obtained for our MWNTs. Since total gate capacitance $C_g \propto L_c$ and charge distribution $S_q \propto L_c$ (if assuming uniform distribution of fluctuators along the channel), $\gamma S_g \propto 1/L_c$. In liquid gated CNT [168] and graphene [169] transistors such length dependence was observed. However, such observation was not done here mainly due to the fact that in those liquid gated studies the channel lengths were varied up to the diffusive regime, which was not the case in this study.

5.6.3 RTN

As discussed earlier, the characteristic time τ of the Lorentzian spectrum can be expressed as $1/\tau = 1/\tau_1 + 1/\tau_2$, where $1/\tau_1$ and $1/\tau_2$ are the generation and recombination times, respectively. The characteristic time is expected to reduce with applied bias [178] and hence the spectrum shows an evolution from Lorentzian to $1/f$ type as a function of source-drain voltage.

Our measured devices exhibit RTN which is quite typical in CNT devices especially at low temperatures. However, there is no particular V_{sd} or V_g dependence of the RTN but they seem to be distributed randomly throughout the bias range and gate range from OFF-state to ON-states as seen from figure 5.8. The current variation in the samples are between 0.1% and 5% being similar than in typical MOSFETs but lower than in SWNTs [165].

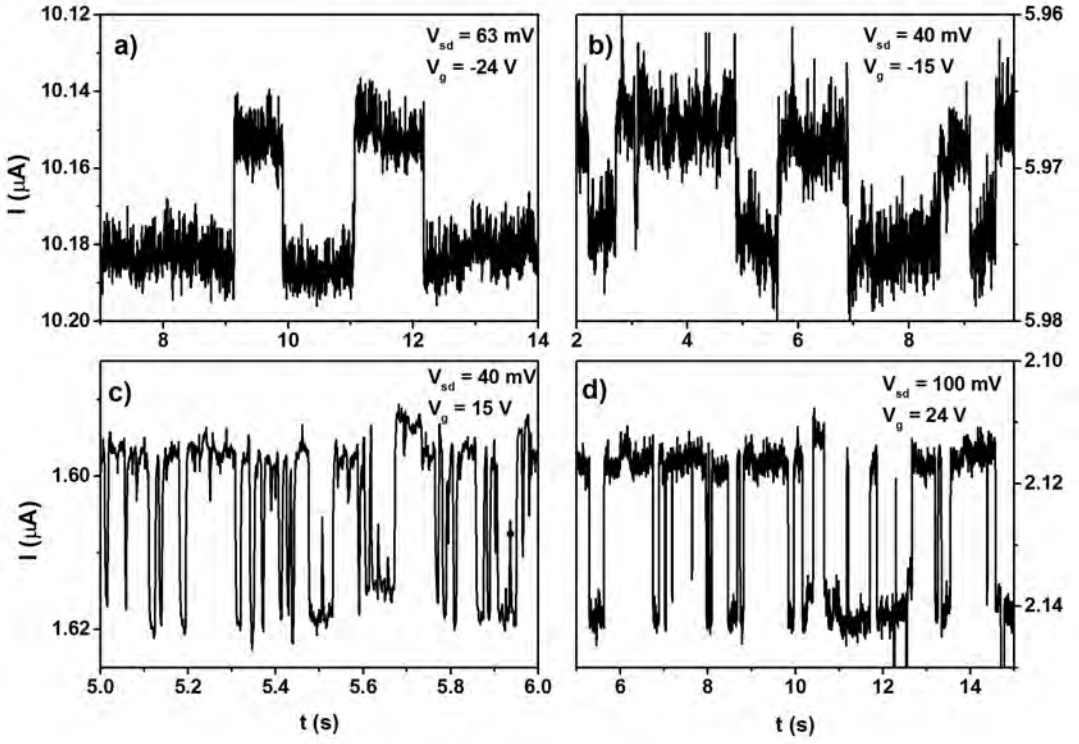

Figure 5.8: RTN signals of nanotube A with different gate and bias voltages. The data shows random and independent configuration of RTN in respect to V_g and V_{sd}. RTN in (a) ON-state (p-side), $V_g = -24$V and $V_{sd} = 63$mV, (b) near the subthreshold region ($V_g = -15$V and $V_{sd} = 40$mV), (c) subthreshol region (n-side) $V_g = 15$V and $V_{sd} = 40$mV, (d) ON-state (n-side) $V_g = 24$V and $V_{sd} = 100$mV.

5.6.4 Discussion

Overall, the noise behavior is qualitatively similar to SWNTs but the noise magnitude is smaller than in SWNTs probably because of the larger diameter of MWNTs. SWNTs being smaller objects are more sensitive to interface effects leading to larger RTN and noise magnitude. The fluctuations of current can be explained better by using a charge noise model pointing towards the modulation of transmission probability in ballistic device as in SWNTs. The McWhorter model which is used in diffusive systems fails to explain the data accurately. The crucial factors for optimizing the noise in CNT-FETs seem to be the diameter control and the quality of the gate oxide. A fully suspended structure in vacuum should therefore result in better low noise transistors. Our results can be generalized for other types of ballistic nanoscale transistors describing their noise properties.

Chapter 6

Conclusions

Combined Raman and transport studies Individual single-walled carbon nanotube devices were studied by using two mutually independent methods as is discussed in the papers **I**–**II** and in the chapter **2** of this thesis. With these two methods it is possible to compare the validity of an individual method and especially obtain more detailed information about the structure of a single tube. Raman measurements of one semiconducting SWNT suggest a special resonance condition which will explain the anomalous intensity ratio of Raman G-band. Transport measurements of metallic tubes indicate the other tube to exhibit a small band gap which was furthermore supported by the data obtained from Raman measurements.

Suspended CNT structures Suspended CNT devices were utilized by bridging nanotubes across a microfabricated slit. The ultimate goal was to combine transport as well as optical measurements and electron microscopy on the same individual device. Unfortunately, further development is needed to make reliable electrical contacts to the devices and thus the main contribution of the author of this thesis was to develop the sample structure and establish CNT synthesis setup in-house. The sample processing of such tubes is described in the chapter **3** and papers **III**–**V** and chapter **4** presents novel nonlinear optical measurements together with electron diffraction that have been utilized for the suspended tubes. The FWM signal from semiconducting SWNT as well as SHG signal from individual SWNT was seen for the first time and furthermore, FWM imaging of nanotubes were presented. Overall, the designed sample structure is advantageous in basic research since it allows to perform electrical transport measurements and optical spectroscopy to a tube with known electronic structure.

$1/f$ noise from MWNTs Paper **VI** and chapter **5** deals with $1/f$ noise in multiwalled carbon nanotube FETs. The results suggest that intermediate sized MWNTs have similar transport properties compared to SWNTs exhibiting quasi-ballistic transport. Thus the proper model explaining the $1/f$ noise char-

acteristics has to be a ballistic model opposite to the McWhorter model which has its origin in diffusive transport. Our results verify that the noise behavior can indeed be explained very well by using the charge noise model which has its origin in ballistic transport. Furthermore, the noise magnitude is around two orders of magnitude smaller than in SWNTs. These results give important information about noise properties of channel-limited ballistic transistors and can be utilized in the future on different ballistically conducting devices.

Bibliography

[1] De Volder, M. F. L., Tawfick, S. H., Baughman, R. H., and Hart, A. J. *Carbon nanotubes: Present and future commercial applications.* Science, **339**, 535 (2013).

[2] Iijima, S. *Helical microtubules of graphitic carbon.* Nature, **354**, 56 (1991).

[3] Radushkevich, L. V. and Lukyanovich, V. M. *O strukture ugleroda, obrazujucegosja pri termiceskom razlozenii okisi ugleroda na zeleznom kontakte.* Soviet Journal of Physical Chemistry, **26**, 88 (1952).

[4] Oberlin, A., Endo, M., and Koyama, T. *Filamentous growth of carbon through benzene decomposition.* Journal of Crystal Growth, **32**, 335 (1976).

[5] Reibold, M., Paufler, P., Levin, A. A., W., K., Pätzke, N., and Meyer, D. C. *Carbon nanotubes in an ancient damascus sabre.* Nature, **444**, 286 (2006).

[6] Kroto, H. W., Heath, J. R., O'Brien, S. C., Curl, R. F., and Smalley, R. E. C_{60}*: Buckminsterfullerene.* Nature, **318**, 162 (1985).

[7] Novoselov, K. S., Geim, A. K., Morozov, S. V., Jiang, D., Zhang, Y., Dubonos, S. V., Grigorieva, I. V., and Firsov, A. A. *Electric field effect in atomically thin carbon films.* Science, **306**, 666 (2004).

[8] Charlier, J.-C., Blase, X., and Roche, S. *Electronic and transport properties of nanotubes.* Rev. Mod. Phys., **79**, 677 (2007).

[9] Saito, R., Dresselhaus, G., and Dresselhaus, M. S. *Physical Properties of Carbon Nanotubes.* First edition. Imperial College Press (1998).

[10] Mintmire, J. W. and White, C. T. *Universal density of states for carbon nanotubes.* Phys. Rev. Lett., **81**, 2506 (1998).

[11] Kittel, C. *Introduction to Solid State Physica.* Eight edition. John Wiley & Sons (2005).

[12] Datta, S. *Quantum Transport: Atom to transistor.* First edition. Cambridge University Press (2007).

[13] Datta, S. *Electronic Transport in Mesoscopic Systems.* First edition. Cambridge University Press (1997).

[14] Kong, J., Yenilmez, E., Tombler, T. W., Kim, W., and Dai, H. *Quantum interference and ballistic transmission in nanotube electron waveguides.* Phys. Rev. Lett., **87**, 106801 (2001).

[15] Mann, D., Javey, A., Kong, J., Wang, Q., and Dai, H. *Ballistic transport in metallic nanotubes with reliable pd ohmic contacts.* Nano Letters, **3**, 1541 (2003).

[16] Javey, A., Guo, J., Lundstrom, M., and Dai, H. *Ballistic carbon nanotube field-effect transistors.* Nature, **424**, 654 (2003).

[17] White, C. T. and Todorov, T. N. *Carbon nanotubes as long ballistic conductors.* Nature, **393**, 240 (1998).

[18] Heinze, S., Tersoff, J., Martel, R., Derycke, V., Appenzeller, J., and Avouris, P. *Carbon nanotubes as schottky barrier transistors.* Phys. Rev. Lett., **89**, 106801 (2002).

[19] Biercuk, M. J., Ilani, S., Marcus, C. M., and McEuen, P. L. *Electrical transport in single-wall carbon nanotubes.* In *Carbon Nanotubes: Advanced Topics in the Synthesis, Structure, Properties and Applications*, edited by A. Jorio, M. S. Dresselhaus, and G. Dresselhaus, volume 111 of *Topics in Applied Physics*, first edition, pp. 455–493. Springer, Berlin (2008).

[20] Pop, E., Mann, D., Cao, J., Wang, Q., Goodson, K., and Dai, H. *Negative differential conductance and hot phonons in suspended nanotube molecular wires.* Phys. Rev. Lett., **95**, 155505 (2005).

[21] Zhou, X., Park, J.-Y., Huang, S., Liu, J., and McEuen, P. L. *Band structure, phonon scattering, and the performance limit of single-walled carbon nanotube transistors.* Phys. Rev. Lett., **95**, 146805 (2005).

[22] Gmez-Navarro, C., De Pablo, P. J., Gmez-Herrero, B., J. Biel, Garcia-Vidal, F. J., Rubio, A., and Flores, F. *Tuning the conductance of single-walled carbon nanotubes by ion irradiation in the anderson localization regime.* Nature materials, **4**, 534 (2005).

[23] Minot, E. D., Yaish, Y., Sazonova, V., Park, M., J-Y.and Brink, and McEuen, P. L. *Tuning carbon nanotube band gaps with strain.* Phys. Rev. Lett., **90**, 156401 (2003).

[24] Postma, H. W. C., Teepen, T., Yao, Z., Grifoni, M., and Dekker, C. *Carbon nanotube single-electron transistors at room temperature*. Science, **293**, 76 (2001).

[25] Purewal, M. S., Hong, B. H., Ravi, A., Chandra, B., Hone, J., and Kim, P. *Scaling of resistance and electron mean free path of single-walled carbon nanotubes*. Phys. Rev. Lett., **98**, 186808 (2007).

[26] Liang, W., Bockrath, M., Bozovic, D., Hafner, J. H., Tinkham, M., and Park, H. *Fabry-perot interference in a nanotube electtron waveguide*. Nature, **411**, 665 (2001).

[27] Long, D. A. *The Raman Effect*. First edition. John Wiley & Sons (2002).

[28] Turrell, G. *The raman effect*. In *Raman Microscopy*, edited by G. Turrell and J. Corset, first edition, pp. 1–25. Academic Press, London (1996).

[29] Dresselhaus, M. S., Dresselhaus, G., Jorio, A., Souza Filho, A. G., and Saito, R. *Raman spectroscopy on isolated single wall carbon nanotubes*. Carbon, **40**, 2043 (2002).

[30] Dresselhaus, M. S., Dresselhaus, G., Saito, R., and Jorio, A. *Raman spectroscopy of carbon nanotubes*. Physics Reports, **409**, 47 (2005).

[31] Araujo, P. T., Doorn, S. K., Kilina, S., Tretiak, S., Einarsson, E., Maruyama, S., Chacham, H., Pimenta, M. A., and Jorio, A. *Third and fourth optical transitions in semiconducting carbon nanotubes*. Phys. Rev. Lett., **98**, 067401 (2007).

[32] Meyer, J. C., Paillet, M., Michel, T., Morac, A., Neumann, A., S., D. G., Roth, S., and Sauvajol, J.-L. *Raman modes of index-identified freestanding single-walled carbon nanotubes*. Phys. Rev. Lett., **95**, 217401 (2005).

[33] Liu, K., Wang, W., Wu, M., Xiao, F., Hong, X., Aloni, S., Bai, X., Wang, E., and Wang, F. *Intrinsic radial breathing oscillation in suspended single-walled carbon nanotubes*. Phys. Rev. B, **83**, 113404 (2011).

[34] Levshov, D., Than, T. X., Arenal, R., Popov, V. N., Parret, R., Paillet, M., Jourdain, V., Zahab, A. A., Michel, T., Yuzyuk, Y. I., and Sauvajol, J.-L. *Experimental evidence of a mechanical coupling between layers in an individual double-walled carbon nanotube*. Nano Letters, **11**, 4800 (2011).

[35] Araujo, P. T., Maciel, I. O., Pesce, P. B. C., Pimenta, M. A., Doorn, S. K., Qian, H., Hartschuh, A., Steiner, M., Grigorian, L., Hata, K., and Jorio, A. *Nature of the constant factor in the relation between radial breathing mode frequency and tube diameter for single-wall carbon nanotubes.* Phys. Rev. B, **77**, 241403 (2008).

[36] Kataura, H., Kumazawa, Y., Maniwa, Y., Umezu, I., Suzuki, S., Ohtsuka, Y., and Achiba, Y. *Optical properties of single-wall carbon nanotubes.* Synthetic Metals, **103**, 2555 (1999).

[37] Maultzsch, J., Telg, H., Reich, S., and Thomsen, C. *Radial breathing mode of single-walled carbon nanotubes: Optical transition energies and chiral-index assignment.* Phys. Rev. B, **72**, 205438 (2005).

[38] Kane, C. L. and Mele, E. J. *Electron interactions and scaling relations for optical excitations in carbon nanotubes.* Phys. Rev. Lett., **93**, 197402 (2004).

[39] Jorio, A., Kauppinen, E., and Hassanien, A. *Carbon-nanotube metrology.* In *Carbon Nanotubes: Advanced Topics in the Synthesis, Structure, Properties and Applications*, edited by A. Jorio, M. S. Dresselhaus, and G. Dresselhaus, volume 111 of *Topics in Applied Physics*, first edition, pp. 63–100. Springer, Berlin (2008).

[40] Saito, R., Grneis, A., Samsonidze, G. G., Brar, V. W., Dresselhaus, G., Dresselhaus, M. S., Jorio, A., Canado, L. G., Fantini, C., Pimenta, M. A., and Souza Filho, A. G. *Double resonance raman spectroscopy of single-wall carbon nanotubes.* New Journal of Physics, **5**, 157 (2003).

[41] Souza, M., Jorio, A., Fantini, C., Neves, B. R. A., Pimenta, M. A., Saito, R., Ismach, A., Joselevich, E., Brar, V. W., Samsonidze, G. G., Dresselhaus, G., and Dresselhaus, M. S. *Single- and double-resonance raman g-band processes in carbon nanotubes.* Phys. Rev. B, **69**, 241403 (2004).

[42] Piscanec, S., Lazzeri, M., Mauri, F., and Ferrari, A. C. *Optical phonons of graphene and nanotubes.* The European Physical Journal Special Topics, **148**, 159 (2007).

[43] Piscanec, S., Lazzeri, M., Robertson, J., Ferrari, A., and Mauri, F. *Optical phonons in carbon nanotubes: Kohn anomalies, peierls distortions, and dynamic effects.* Phys. Rev. B, **75**, 035427 (2007).

[44] Brown, S. D. M., Jorio, A., Corio, P., Dresselhaus, M. S., Dresselhaus, G., Saito, R., and Kneipp, K. *Origin of the breit-wigner-fano lineshape of the tangential g-band feature of metallic carbon nanotubes.* Phys. Rev. B, **63**, 155414 (2001).

[45] Jiang, C., Kempa, K., Zhao, J., Schlecht, U., Kolb, U., Basché, T., Burghard, M., and Mews, A. *Strong enhancement of the breit-wigner-fano raman line in carbon nanotube bundles caused by plasmon band formation.* Phys. Rev. B, **66**, 161404 (2002).

[46] Kempa, K. *Gapless plasmons in carbon nanotubes and their interactions with phonons.* Phys. Rev. B, **66**, 195406 (2002).

[47] Paillet, M., Poncharal, P., Zahab, A., Sauvajol, J.-L., Meyer, J. C., and Roth, S. *Vanishing of the breit-wigner-fano component in individual single-wall carbon nanotubes.* Phys. Rev. Lett., **94**, 237401 (2005).

[48] Bose, S. M., Gayen, S., and Behera, S. N. *Theory of the tangential g-band feature in the raman spectra of metallic carbon nanotubes.* Phys. Rev. B, **72**, 153402 (2005).

[49] Langer, L., Stockman, L., Heremans, J. P., Bayot, V., Olk, C. H., Van Haesendonck, C., Bruynseraede, Y., and Issi, J.-P. *Electrical resistance of a carbon nanotube bundle.* Journal of Materials Research, **9**, 927 (1994).

[50] Langer, L., Bayot, V., Grivei, E., Issi, J.-P., Heremans, J. P., Olk, C. H., Stockman, L., Van Haesendonck, C., and Bruynseraede, Y. *Quantum transport in a multiwalled carbon nanotube.* Phys. Rev. Lett., **76**, 479 (1996).

[51] Stockman, L., Neuttiens, G., Van Haesendonck, C., and Bruynseraede, Y. *Submicrometer lithographic patterning of thin gold films with a scanning tunneling microscope.* Applied Physics Letters, **62**, 2935 (1993).

[52] Langer, L., Stockman, L., Heremans, J. P., Bayot, V., Olk, C. H., Van Haesendonck, C., Bruynseraede, Y., and Issi, J.-P. *Electrical measurements on submicronic synthetic conductors: carbon nanotubes.* Synthetic Metals, **70**, 1393 (1995).

[53] Dai, H., Wong, E. W., and Lieber, C. M. *Probing electrical transport in nanomaterials: Conductivity of individual carbon nanotubes.* Science, **272**, 523 (1996).

[54] Ebbesen, T. W., Lezec, H. J., W., B. J., Ghaemi, H. F., and Thio, T. *Electrical conductivity of individual carbon nanotubes.* Nature, **382**, 54 (1996).

[55] Frank, S., Poncharal, P., Wang, Z. L., and Heer, W. A. d. *Carbon nanotube quantum resistors.* Science, **280**, 1744 (1998).

[56] Yamamoto, K., Akita, S., and Nakayama, Y. *Orientation and purification of carbon nanotubes using ac electrophoresis.* Journal of Physics D: Applied Physics, **31**, L34 (1998).

[57] Nagahara, L. A., Amlani, I., Lewenstein, J., and Tsui, R. K. *Directed placement of suspended carbon nanotubes for nanometer-scale assembly.* Applied Physics Letters, **80**, 3826 (2002).

[58] Krupke, R., Hennrich, F., Weber, H. B., Kappes, M. M., and v. Lhneysen, H. *Simultaneous deposition of metallic bundles of single-walled carbon nanotubes using ac-dielectrophoresis.* Nano Letters, **3**, 1019 (2003).

[59] Zhang, Z.-B., Zhang, S.-L., and Campbell, E. E. B. *All-around contact for carbon nanotube field-effect transistors made by ac dielectrophoresis.* Journal of Vacuum Science & Techonology B, **24**, 131 (2006).

[60] Tans, S. J., Devoret, M. H., Dai, H., Thess, A., Smalley, R. E., Geerlings, L. J., and Dekker, C. *Individual single-wall carbon nanotubes as quantum wires.* Nature, **386**, 474 (1997).

[61] Tans, S. J., Verschueren, A. R. M., and C., D. *Room-temperature transistor based on a single carbon nanotube.* Nature, **393**, 49 (1998).

[62] Bockrath, M., Cobden, D. H., McEuen, P. L., Chopra, N. G., Zettl, A., Thess, A., and Smalley, R. E. *Single-electron transport in ropes of carbon nanotubes.* Science, **275**, 1922 (1997).

[63] Bockrath, M., Liang, W., Bozovic, D., Hafner, J. H., Lieber, C. M., Tinkham, M., and Park, H. *Resonant electron scattering by defects in single-walled carbon nanotubes.* Science, **291**, 283 (2001).

[64] Martel, R., Derycke, V., Lavoie, C., Appenzeller, J., Chan, K. K., Tersoff, J., and Avouris, P. *Ambipolar electrical transport in semiconducting single-wall carbon nanotubes.* Phys. Rev. Lett., p. 256805 (2001).

[65] Bachtold, A., Hadley, P., Nakanishi, T., and Dekker, C. *Logic circuits with carbon nanotube transistors.* Science, **294**, 1317 (2001).

[66] Freitag, M., Radosavljevic, M., Zhou, Y., Johnson, A. T., and Smith, W. F. *Controlled creation of a carbon nanotube diode by a scanned gate.* Applied Physics Letters, **79**, 3326 (2001).

[67] Chen, Z., Appenzeller, J., Knoch, J., Lin, Y., and Avouris, P. *The role of metal-nanotube contact in the performance of carbon nanotube field-effect transistors.* Nano Letters, **5**, 1497 (2005).

[68] Javey, A., Kim, H., Brink, M., Wang, Q., Ural, A., Guo, J., McIntyre, P., McEuen, P., Lundstrom, M., and Dai, H. *High-κ dielectrics for advanced carbon-nanotube transistors and logic gates.* Nature Materials, **1**, 241 (2002).

[69] Wind, S. J., Appenzeller, J., Martel, R., Derycke, V., and Avouris, P. *Vertical scaling of carbon nanotube field-effect transistors using top gate electrodes.* Applied Physics Letters, **80**, 3817 (2002).

[70] Javey, A., Guo, J., Farmer, D. B., Wang, Q., Wang, D., Gordon, R. G., Lundstrom, M., and Dai, H. *Carbon nanotube field-effect transistors with integrated ohmic contacts and high-κ gate dielectrics.* Nano Letters, **4**, 447 (2004).

[71] Lee, J. U., Gipp, P. P., and Heller, C. M. *Carbon nanotube p-n junction diodes.* Applied Physics Letters, **85**, 145 (2004).

[72] Steele, G. A., Gotz, G., and Kouwenhoven, L. P. *Tunable few-electron double quantum dots and klein tunneling in ultraclean carbon nanotubes.* Nature nanotechnology, **4**, 363 (2009).

[73] Chen, Z., Farmer, D., Xu, S., Gordon, R., Avouris, P., and Appenzeller, J. *Externally assembled gate-all-around carbon nanotube field-effect transistor.* Electron Device Letters, IEEE, **29**, 183 (2008).

[74] Nagy, J. B., Bister, G., Fonseca, A., Mhn, D., Knya, Z., Kiricsi, I., Horvth, Z. E., and Bir, L. P. *On the growth mechanism of single-walled carbon nanotubes by catalytic carbon vapor deposition on supported metal catalysts.* Journal of Nanoscience and Nanotechnology, **4**, 326 (2004).

[75] Koshio, A., Yudasaka, M., and Iijima, S. *Metal-free production of high-quality multi-wall carbon nanotubes, in which the innermost nanotubes have a diameter of 0.4 nm.* Chemical Physics Letters, **356**, 595 (2002).

[76] Queipo, P., Nasibulin, A. G., Gonzalez, D., Tapper, U., Jiang, H., Tsuneta, T., Grigoras, K., Dueas, J. A., and Kauppinen, E. I. *Novel catalyst particle production method for $\{CVD\}$ growth of single- and double-walled carbon nanotubes.* Carbon, **44**, 1604 (2006).

[77] Makarovski, A., Zhukov, A., Liu, J., and Finkelstein, G. *Four-probe measurements of carbon nanotubes with narrow metal contacts.* Phys. Rev. B, **76**, 161405 (2007).

[78] Sasaki, K., Saito, R., Dresselhaus, G., Dresselhaus, M., Farhat, H., and Kong, J. *Chirality-dependent frequency shift of radial breathing mode in metallic carbon nanotubes.* Phys. Rev. B, **78**, 235405 (2008).

[79] Zhou, C., Kong, J., and Dai, H. *Intrinsic electrical properties of individual single-walled carbon nanotubes with small band gaps.* Phys. Rev. Lett., **84**, 5604 (2000).

[80] Jorio, A., Souza Filho, A. G., Dresselhaus, G., Dresselhaus, M. S., Swan, A. K., Ünlü, M. S., Goldberg, B. B., Pimenta, M. A., Hafner, J. H., Lieber, C. M., and Saito, R. *g-band resonant raman study of 62 isolated single-wall carbon nanotubes.* Phys. Rev. B, **65**, 155412 (2002).

[81] Mudimela, P., Nasibulin, A. G., Jiang, H., Susi, T., Chassaing, D., and Kauppinen, E. I. *Incremental variation in the number of carbon nanotube walls with growth temperature.* The Journal of Physical Chemistry C, **113**, 2212 (2009).

[82] Homma, Y., Chiashi, S., and Kobayashi, Y. *Suspended single-wall carbon nanotubes: synthesis and optical properties.* Rep. Prog. Phys., **72**, 066502 (2009).

[83] Salvetat, J.-P., Briggs, G. A. D., Bonard, J.-M., Bacsa, R. R., Kulik, A. J., Stöckli, T., Burnham, N. A., and Forró, L. *Elastic and shear moduli of single-walled carbon nanotube ropes.* Phys. Rev. Lett., **82**, 944 (1999).

[84] Walters, D. A., Ericson, L. M., J., C. M., Liu, J., Colbert, D. T., Smith, K. A., and E., S. R. *Elastic strain of freely suspended single-wall carbon nanotube ropes.* Applied Physics Letters, **74**, 3803 (1999).

[85] Nygrd, J. and Cobden, D. H. *Quantum dots in suspended single-wall carbon nanotubes.* Applied Physics Letters, **79**, 4216 (2001).

[86] Lin, Y.-M., Tsang, J. C., Freitag, M., and Avouris, P. *Impact of oxide substrate on electrical and optical properties of carbon nanotube devices.* Nanotechnology, **18**, 295202 (2007).

[87] Sangwan, V. K., Ballarotto, V. W., Fuhrer, M. S., and D., W. E. *Facile fabrication of suspended as-grown carbon nanotube devices.* Applied Physics Letters, **93**, 113112 (2008).

[88] Tombler, T. W., Zhou, C., Alexseyev, L., Kong, J., Dai, H., Liu, L., Jayanthi, C. S., Tang, M., and Wu, S.-Y. *Reversible electromechanical characteristics of carbon nanotubes under local-probe manipulation.* Nature, **405**, 769 (2000).

[89] Cao, J., Wang, Q., and Wang, H., D.and Dai. *Suspended carbon nanotube quantum wires with two gates.* Small, **1**, 138 (2005).

[90] Franklin, N. R., Wang, Q., Tombler, T., Javey, A., Shim, M., and Dai, H. *Integration of suspended carbon nanotube arrays into electronic devices and electromechanical systems.* Applied Physics Letters, **81**, 913 (2002).

[91] Ahn, J.-H., Kim, H.-S., Lee, K. J., Jeon, S., Kang, S. J., Sun, Y., Nuzzo, R. G., and Rogers, J. A. *Heterogeneous three-dimensional electronics by use of printed semiconductor nanomaterials.* Science, **314**, 1754 (2006).

[92] Wu, Y., Lin, X., and Zhang, M. *Carbon nanotubes for thin film transistor: Fabrication, properties, and applications.* Journal of Nanomaterials, **2003**, 627215 (2013).

[93] Wu, C. C., Liu, C. H., and Z., Z. *One-step direct tranfer of pristine single-walled carbon nanotubes for functional nanoelectronis.* Nano Letters, **10**, 1032 (2010).

[94] Liu, C.-H., Wu, C.-C., and Zhong, Z. *A fully tunable single-walled carbon nanotube diode.* Nano Letters, **11**, 1782 (2011).

[95] Jiao, L., Xian, X., Wu, Z., Zhang, J., and Liu, Z. *Selective positioning and integration of individual single-walled carbon nanotubes.* Nano Letters, **9**, 205 (2009).

[96] Kasumov, A. Y., Deblock, R., Kociak, M., Reulet, B., Bouchiat, H., Khodos, I. I., Gorbatov, Y. B., Volkov, V. T., Journet, C., and Burghard, M. *Supercurrents through single-walled carbon nanotubes.* Science, **284**, 1508 (1999).

[97] Kociak, M., Suenaga, K., Hirahara, K., Saito, Y., Nakahira, T., and Iijima, S. *Linking chiral indices and transport properties of double-walled carbon nanotubes.* Phys. Rev. Lett., **89**, 155501 (2002).

[98] Meyer, J. C., Obergfell, D., Roth, S., Yang, S., and Yang, S. *Transmission electron microscopy and transistor characteristics of the same carbon nanotube.* Appl. Phys. Lett., **85**, 2911 (2004).

[99] Sfeir, M. Y., Beetz, T., Wang, L., F.and Huang, Huang, X. M. H., Huang, M., Hone, J., O'Brien, S., Misewich, J. A., Heinz, T. F., Wu, L., Zhu, Y., and Brus, L. E. *Optical spectroscopy of individual single-walled carbon nanotubes of defined chiral structure.* Science, **312**, 554 (2006).

[100] Liu, K., Wang, W., Xu, Z., Bai, X., Wang, E., Yao, Y., Zhang, J., and Liu, Z. *Chirality-dependent transport properties of double-walled nanotubes measured in situ on their field-effect transistors.* Journal of the American Chemical Society, **131**, 62 (2009).

[101] Huang, X. M. H., Caldwell, R., Huang, L., Jun, S. C., Huang, M., Sfeir, M. Y., O'Brien, S., and Hone, J. *Controlled placement of individual carbon nanotubes.* Nano Letters, **5**, 1515 (2005).

[102] B., C., Caldwell, R., Huang, M., Huang, L., Sfeir, M. Y., O'Brien, S., Heinz, T. F., and Hone, J. *Electrical transport measurements of nanotubes with known (n, m) indices.* phys. stat. sol. (b), **234**, 3359 (2006).

[103] Kim, T., Zuo, J.-M., Olson, E. A., and Petrov, I. *Imaging suspended carbon nanotubes in field-effect transistors configured with microfabricated slits for transmission electron microscopy.* Appl. Phys. Lett., **87**, 173108 (2005).

[104] Madou, M. J. *Fundamentals of Microfabrication: The Science of Miniturization.* second edition. CRC Press (2002).

[105] Franssila, S. *Introduction to Microfabrication.* first edition. Wiley (2004).

[106] Pant, B. D. and Tandon, U. S. *Etching of silicon nitride in* CCl_2F_2, CHF_3, SiF_4, *and* SF_6 *reactive plasma: A comparative study.* Plasma Chemistry and Plasma Processing, **14**, 603 (2006).

[107] Seidel, H., Csepregi, L., Heuberger, A., and Baumgrtel, H. *Anisotropic etching of crystalline silicon in alkaline solutions: I . orientation dependence and behavior of passivation layers.* J. Electrochem. Soc., **137**, 3612 (1990).

[108] Kuzyk, A., Yurke, B., Toppari, J. J., Linko, V., and Trm, P. *Dielectrophoretic trapping of dna origami.* Small, **4**, 447 (2008).

[109] Kumar, M. and Ando, Y. *Chemical vapor deposition of carbon nanotubes: A review on growth mechanism and mass production.* J. Nanosci. Nanotechnol., **10**, 3739 (2010).

[110] Kumar, M. *Carbon nanotube synthesis and growth mechanism.* In *Carbon Nanotubes - Synthesis, Characterization, Applications*, edited by S. Yellampalli, first edition, pp. 63–100. InTech, Croatia (2011).

[111] Maruyama, S., Kojima, R., Miyauchi, Y., Chiashi, S., and Kohno, M. *Low-temperature synthesis of high-purity single-walled carbon nanotubes from alcohol.* Chemical Physics Letters, **360**, 229 (2002).

[112] Murakami, Y., Miyauchi, Y., Chiashi, S., and Maruyama, S. *Characterization of single-walled carbon nanotubes catalytically synthesized from alcohol.* Chemical Physics Letters, **374**, 53 (2003).

[113] Zheng, L. X., O'Connell, M. J., Doorn, S. K., Liao, X. Z., Zhao, Y. H., Akhadov, E. A., Hoffbauer, M. A., Roop, B. J., Jia, Q. X., Dye, R. C., Peterson, D. E., Huang, S. M., Liu, J., and Zhu, Y. T. *Ultralong single-wall carbon nanotubes.* Nature materials, **3**, 673 (2004).

[114] Reina, A., Hofmann, M., Zhu, D., and Kong, J. *Growth mechanism of long and horizontally aligned carbon nanotubes by chemical vapor deposition.* Journal of Physical Chemistry C, **111**, 7292 (2007).

[115] Hofmann, M., Nezich, D., Alfonso, R., and Kong, J. *In-situ sample rotation as a tool to understand chemical vapor deposition growth of long aligned carbon nanotubes.* Nano Letters, **8**, 4122 (2008).

[116] Zhang, R., Xie, H., Zhang, Y., Zhang, Q., Jin, Y., Li, P., Qian, W., and Wei, F. *The reason for the low density of horizontally aligned ultralong carbon nanotube arrays.* Carbon, **52**, 232 (2013).

[117] Zhou, W., Rutherglen, C., and Burke, P. J. *Wafer scale synthesis of dense aligned arrays of single-walled carbon nanotubes.* Nano Research, **1**, 158 (2008).

[118] Liu, Z., Jiao, L., Yao, Y., Xian, X., and Zhang, J. *Aligned, ultralong single-walled carbon nanotube: From synthesis, sorting, to electronic devices.* Advanced Materials, **22**, 2285 (2010).

[119] Hong, B. H., Lee, J. Y., Beetz, T., Zhu, Y., Kim, P., and Kim, K. S. *Quasi-continuous growth of ultralong carbon nanotube arrays.* Journal of the American Chemical Society, **127**, 15336 (2005).

[120] Huang, L., White, B., Sfeir, M. Y., Huang, M., Huang, H. X., Wind, S., Hone, J., and O'Brien, S. *Cobalt ultrathin film catalyzed ethanol chemical vapor deposition of single-walled carbon nanotubes.* The Journal of Physical Chemistry B, **110**, 11103 (2006).

[121] Elliot, S. *The Physics and Chemistry of Solids.* First edition. Wiley (2005).

[122] Goodhew, P. J., Humphreys, F. J., and Beanland, R. *Electron Microscopy and Analysis.* Third edition. Taylor & Francis (2001).

[123] Qin, L.-C. *Electron diffraction from carbon nanotubes.* Reports on Progress in Physics, **69**, 2761 (2006).

[124] Qin, L.-C. *Measuring the true helicity of carbon nanotubes.* Chemical Physics Letters, **297**, 23 (1998).

[125] Gao, M., Zuo, J. M., Twesten, R. D., Petrov, I., Nagahara, L. A., and Zhang, R. *Structure determination of individual single-wall carbon nanotubes by nanoarea electron diffraction.* Applied Physics Letters, **82**, 2703 (2003).

[126] Jiang, H., Nasibulin, A. G., Brown, D. P., and Kauppinen, E. I. *Unambiguous atomic structural determination of single-walled carbon nanotubes by electron diffraction.* Carbon, **45**, 662 (2007).

[127] Wang, Y., Lin, C.-Y., Nikolaenko, A., Raghunathan, V., and Potma, E. O. *Four-wave mixing microscopy of nanostructures.* Adv. Opt. Photon., **3**, 1 (2011).

[128] Boyd, R. W. *Nonlinear Optics.* Second edition. Academic Press (2003).

[129] Shen, Y. R. *Surface properties probed by second-harmonic and sum-frequency generation.* Nature, **337**, 519 (1989).

[130] Petralli-Mallow, T., Wong, T. M., Byers, J. D., Yee, H. I., and Hicks, J. M. *Circular dichroism spectroscopy at interfaces: a surface second harmonic generation study.* The Journal of Physical Chemistry, **97**, 1383 (1993).

[131] Kim, H., Sheps, T., Collins, P. G., and Potma, E. O. *Nonlinear optical imaging of individual carbon nanotubes with four-wave-mixing microscopy.* Nano Letters, **9**, 2991 (2009).

[132] Sheps, J., T.and Brocious, Corso, B. L., Gül, O. T., Whitmore, D., Durkaya, G., Potma, E., and Collins, P. G. *Four-wave mixing microscopy with electronic contrast of individual carbon nanotubes.* Phys. Rev. B, **86**, 235412 (2012).

[133] Seferyan, H. Y., Nasr, M. B., Senekerimyan, V., Zadoyan, R., Collins, P., and Apkarian, V. A. *Transient grating measurements of excitonic dynamics in single-walled carbon nanotubes: The dark excitonic bottleneck.* Nano Letters, **6**, 1757 (2006).

[134] Zhu, Z., Crochet, J., Arnold, M. S., Hersam, M. C., Ulbricht, H., Resasco, D., and Hertel, T. *Pump-probe spectroscopy of exciton dynamics in (6,5) carbon nanotubes.* The Journal of Physical Chemistry C, **111**, 3831 (2007).

[135] Graham, M. W., Ma, Y.-Z., and Fleming, G. R. *Femtosecond photon echo spectroscopy of semiconducting single-walled carbon nanotubes.* Nano Letters, **8**, 3936 (2008).

[136] Kang, K., Ozel, T., Cahill, D., and Shim, M. *Optical phonon lifetimes in single-walled carbon nanotubes by time-resolved raman scattering.* Nano Letters, **8**, 4642 (2008).

[137] Ikeda, K. and Uosaki, K. *Coherent phonon dynamics in single-walled carbon nanotubes studied by time-frequency two-dimensional coherent anti-stokes raman scattering spectroscopy.* Nano Letters, **9**, 1378 (2009).

[138] Berciaud, S., Voisin, C., Yan, H., Chandra, R., B.and Caldwell, Shan, L. E., Y.and Brus, Hone, J., and Heinz, T. F. *Excitons and high-order optical transitions in individual carbon nanotubes: A rayleigh scattering spectroscopy study.* Phys. Rev. B, **81**, 041414 (2010).

[139] De Dominicis, L., Botti, S., Asilyan, L. S., Ciardi, R., Fantoni, R., Terranova, M. L., Fiori, A., Orlanducci, S., and Appolloni, R. *Second- and third- harmonic generation in single-walled carbon nanotubes at nanosecond time scale.* Applied Physics Letters, **85**, 1418 (2004).

[140] Akimov, D., Alfimov, M., Konorov, S., Ivanov, A., Botti, S., Podshivalov, A., Ciardi, R., Dominicis, L., Asilyan, L., Fantoni, R., and Zheltikov, A. *Second-and third-harmonic generation by carbon nanotubes irradiated with femtosecond laser pulses.* Journal of Experimental and Theoretical Physics, **98**, 220 (2004).

[141] De Dominicis, L., Fantoni, R., Botti, S., Ciardi, R., Asilyan, L., Fiori, A., and Orlanducci, S. *Analysis of the chiral composition of a carbon nanotube surface by means of second harmonic generation.* Journal of Raman Spectroscopy, **36**, 165 (2005).

[142] Su, H. M., Ye, J. T., Tang, Z. K., and Wong, K. S. *Resonant second-harmonic generation in monosized and aligned single-walled carbon nanotubes.* Phys. Rev. B, **77**, 125428 (2008).

[143] Guo, G. Y., Chu, K. C., Wang, D., and Duan, C. *Linear and nonlinear optical properties of carbon nanotubes from first-principles calculations.* Phys. Rev. B, **69**, 205416 (2004).

[144] Pedersen, T. G. and Pedersen, K. *Systematic tight-binding study of optical second-harmonic generation in carbon nanotubes.* Phys. Rev. B, **79**, 035422 (2009).

[145] Kogan, S. *Electronic noise and fluctuations in solids.* First edition. Cambridge University Press (1996).

[146] Caloyannides, M. A. *Microcycle spectral estimates of $1/f$ noise in semiconductors.* Journal of Applied Physics, **45**, 307 (1974).

[147] Weissman, M. B. $1/f$ *noise and other slow, nonexponential kinetics in condensed matter*. Reviews of Modern Physics, **60**, 537 (1988).

[148] Hooge, F. N. and Hoppenbrouwers, A. M. H. $1/f$ *noise in continuous thin gold films*. Physica, **45**, 386 (1969).

[149] Ralls, K. S., Skocpol, W. J., Jackel, L. D., Howard, R. E., Fetter, L. A., Epworth, R. W., and Tennant, D. M. *Discrete resistance switching in submicrometer silicon inversion layers: Individual interface traps and low-frequency ($1/f$?) noise*. Phys. Rev. Lett., **52**, 228 (1984).

[150] Malchup, S. *Noise in semiconductors: Spectrum of a two-parameter random signal*. Journal of Applied Physics, **25**, 341 (1954).

[151] Dmitriev, A. P., Levinshtein, M. E., and Rumyantsev, S. L. *On the hooge relation in semiconductors and metals*. Journal of Applied Physics, **106**, 024514 (2009).

[152] McWhorter, A. L. $1/f$ *noise and germanium surface properties*. In *Semiconductor Surface Physics*, edited by R. A. Kingston, first edition, pp. 207–228. University of Pennsylvania Press (1957).

[153] Vandamme, L. K. J., Li, X., and Rigaud, D. $1/f$ *noise in mos devices, mobility or number fluctuations*. IEEE Transactions on electron devices, **41**, 1936 (1994).

[154] Vandamme, E. P. and Vandamme, L. K. J. *Critical discussion on unified 1/f noise models for mosfets*. IEEE Transactions on electron devices, **47**, 2146 (2000).

[155] Dekker, C., Scholten, A. J., Liefrink, F., Eppenga, R., van Houten, H., and Foxon, C. T. *Spontaneous resistance switching and low-frequency noise in quantum point contacts*. Physical Review Letters, **66**, 2148 (1991).

[156] Liefrink, F., Dijkhuis, J. I., and van Houten, H. *Low-frequency noise in quantum point contacts*. Semiconductor Science and Technology, **9**, 2178 (1994).

[157] Collins, P. G., Fuhrer, M. S., and Zettl, A. $1/f$ *noise in carbon nanotubes*. Applied Physics Letters, **76**, 894 (2000).

[158] Briman, M., Bradley, K., and Gruner, G. *Source of* $1/f$ *noise in carbon nanotube devices*. Journal of Applied Physics, **100**, 013505 (2006).

[159] Lin, Y.-M., Appenzeller, J., Knoch, J., Chen, Z., and Avouris, P. *Low-frequency current fluctuations in individual semiconducting single-wall carbon nanotubes.* Nano Letters, **6**, 930 (2006).

[160] Ishigami, M., Chen, J. H., Williams, E. D., Tobias, D., Chen, Y. F., and Fuhrer, M. S. *Hooge's constant for carbon nanotube field effect transistor.* Journal of Applied Physics, **88**, 203116 (2006).

[161] Liu, F., Wang, K. L., Zhang, D., and Zhou, C. *Noise in carbon nanotube field effect transistor.* Applied Physics Letters, **89**, 063116 (2006).

[162] Tobias, D., Ishigami, M., Tselev, A., Barbara, P., Williams, E. D., Lobb, C. J., and Fuhrer, M. S. *Origins of $1/f$ noise in individual semiconducting carbon nanotube field-effect transistors.* Physical Review B, **77**, 033407 (2008).

[163] Liu, F., Bao, M., Kim, H., and Wang, K. L. *Giant random telegraph signals in the carbon nanotubes as a single defect probe.* Applied Physics Letters, **86**, 163102 (2005).

[164] Liu, F., Wang, K. L., Zhang, D., and Zhou, C. *Random telegraph signals and noise behaviors in carbon nanotube transistors.* Applied Physics Letters, **89**, 243101 (2006).

[165] Wang, N.-P., Heinze, S., and Tersoff, J. *Random-telegraph-signal noise and device variability in ballistic nanotube transistors.* Nano Letters, **7**, 910 (2007).

[166] Tarkiainen, R., Roschier, L., Ahlskog, M., Paalanen, M., and Hakonen, P. *Low-frequency current noise and resistance fluctuations in multiwalled carbon nanotubes.* Physica E, **28**, 57 (2005).

[167] Tersoff, J. *Low-frequency noise in nanoscale ballistic transistors.* Nano Letters, **7**, 194 (2007).

[168] Mannik, J., Heller, A. M., I.and Janssens, Lemay, S. G., and Dekker, C. *Charge noise in liquid-gated single-wall carbon nanotube transistors.* Nano Letters, **8**, 685 (2008).

[169] Heller, S., I.and Chatoor, Mannik, J., Zevenbergen, M. A. G., Oostinga, J. B., Morpurgo, A. F., Dekker, C., and Lemay, S. G. *Charge noise in graphene transistors.* Nano Letters, **10**, 1563 (2010).

[170] Roschier, L., Tarkiainen, R., Ahlskog, M., Paalanen, M., and Hakonen, P. *Multiwalled carbon nanotubes as ultrasensitive electrometers.* Applied Physics Letters, **78**, 3295 (2001).

[171] Ouacha, H., Willander, M., Yu, H. Y., Park, Y. W., Kabir, M. S., Persson, S. H. M., Kish, L. B., and Ouacha, A. *Noise properties of an individual and two crossing multiwalled carbon nanotubes.* Applied Physics Letters, **80**, 1055 (2002).

[172] Lassagne, B., Raquet, B., Broto, J.-M., Cleuziou, J.-P., Ondaruhu, T., Monthioux, M., and Magrez, A. *Electronic fluctuations in multi-walled carbon nanotubes.* New Journal of Physics, **8**, 31 (2006).

[173] Ahlskog, M., Herranen, O., Johansson, A., Leppaniemi, J., and Mtsuko, D. *Electronic transport in intermediate sized carbon nanotubes.* Physical Review B, **79**, 155408 (2009).

[174] Tarkiainen, R., Ahlskog, M., Zyuzin, A., Hakonen, P., and Paalanen, M. *Transport in strongly disordered multiwalled carbon nanotubes.* Phys. Rev. B, **69**, 033402 (2004).

[175] Bourlon, B., Glattli, D. C., Plaçais, B., Berroir, J. M., Miko, C., Forró, L., and Bachtold, A. *Geometrical dependence of high-bias current in multiwalled carbon nanotubes.* Phys. Rev. Lett., **92**, 026804 (2004).

[176] Sanvito, S., Kwon, Y.-K., Tománek, D., and Lambert, C. J. *Fractional quantum conductance in carbon nanotubes.* Phys. Rev. Lett., **84**, 1974 (2000).

[177] Li, H. J., Lu, W. G., Li, J. J., Bai, X. D., and Gu, C. Z. *Multichannel ballistic transport in multiwall carbon nanotubes.* Phys. Rev. Lett., **95**, 086601 (2005).

[178] Uren, M. J., Day, D. J., and Kirton, M. J. $1/f$ *and random telegraph noise in silicon metal-oxide-semiconductor field-effect transistors.* Applied Physics Letters, **47**, 1195 (1985).